

Instabilities and Turbulence in Rayleigh-Bénard Convection: Numerical and Phenomenological Studies

A Thesis Submitted

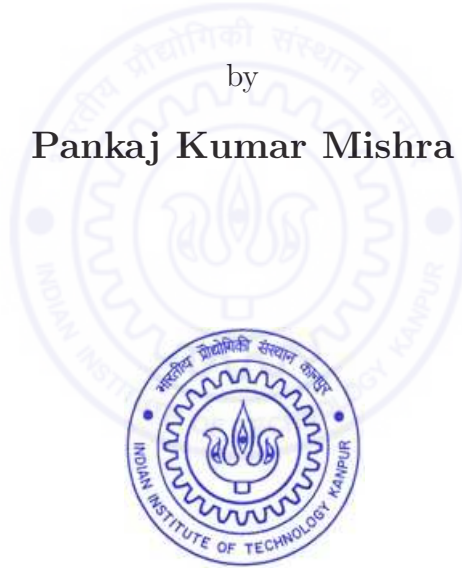
in partial fulfilment of the requirements

for the degree of

Doctor of Philosophy

by

Pankaj Kumar Mishra

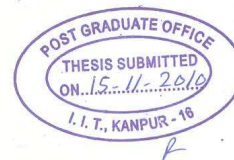


to the

DEPARTMENT OF PHYSICS

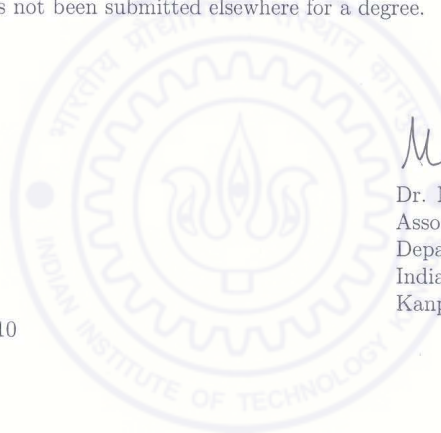
INDIAN INSTITUTE OF TECHNOLOGY KANPUR

November, 2010



Certificate

It is certified that the work contained in this thesis entitled “Instabilities and Turbulence in Rayleigh-Bénard Convection: Numerical and Phenomenological Studies” by Pankaj Kumar Mishra, has been carried out under my supervision and that this work has not been submitted elsewhere for a degree.



Dr. Mahendra K. Verma
Associate Professor
Department of Physics
Indian Institute of Technology
Kanpur

November, 2010

SYNOPSIS

Name of Student: Pankaj Kumar Mishra **Roll No.:** Y3809066
Degree for which submitted: Doctor of Philosophy **Department:** Physics
Title: Instabilities and Turbulence in Rayleigh-Bénard Convection: Numerical and Phenomenological Studies.
Thesis supervisor: Prof. Mahendra K. Verma
Month and Year of submission: November, 2010

Rayleigh-Bénard Convection (RBC), in which fluid in a box is heated from below and cooled from the top, is a classical problem in fluid dynamics with relevance in astrophysical, geophysical, atmospheric, and engineering flows. It exhibits various patterns, chaos, spatio-temporal chaos and turbulence. The dynamics of RBC is mainly governed by two non-dimensional parameters, the Rayleigh number (R), which is the ratio of the buoyancy and the dissipative terms, and the Prandtl number (P), which is the ratio of the heat diffusion time scale and the viscous diffusion time scale. This thesis addresses different aspects of Rayleigh-Bénard convection near the onset and in the fully developed turbulent regime through direct numerical simulations and phenomenological models.

The layout of the thesis is as follows:

In **Chapter 1**, we first introduce Rayleigh-Bénard convection and the corresponding governing hydrodynamical equations. This is followed by a discussion on different types of boundary conditions used in numerical and theoretical studies of RBC. Subsequently, we present various convective states that are observed in RBC as the control parameters R and P are varied. We describe the patterns and instabilities observed near the onset of low-Prandtl number and zero-Prandtl number convection. To this end, we present a

brief literature survey of the analytical, experimental, and numerical works in the area of non-linear instabilities of low- P and zero- P convection. Next, we focus on the turbulent regime of convection, wherein, we discuss two issues: (i) the nature of the velocity and temperature cascades in the inertial range, and (ii) the dynamics of large scale circulation. We first introduce the existing phenomenological theories of the scalings of the spectra of the velocity and temperature fields in the inertial range of turbulent convection. Further, we present the experimental and numerical works related to the phenomenological theories on energy spectra and fluxes. Next, we discuss the Large Scale Circulation (LSC) and its associated dynamics, such as azimuthal reorientations and reversals, in the turbulent regime of RBC as observed in the laboratory experiments. This is followed by an extensive review of the previous phenomenological and numerical works that have been carried out to explain the observed dynamics of LSC in laboratory experiments.

In **Chapter 2**, we present the details of the two codes used in our thesis work: (a) a parallel Pseudo-spectral code for a 3D box, and (b) a parallel finite-difference code for a cylindrical container. We use pseudo-spectral code for two problems: (i) to investigate the dynamics near the instabilities for low- P and zero- P convection, and (ii) to investigate the scalings of the energy cascade in the inertial range for turbulent RBC. The finite-difference code has been used to analyze the reorientations and reversals of LSC in the turbulent regime of convection. In the first part of the chapter, we discuss the details of the techniques and algorithms used in the pseudo-spectral code. This discussion is followed by an introduction to different schemes that have been used for the calculation of various statistical quantities such as fluxes, velocity and temperature spectra, etc., from the numerically calculated fields. In the second part, we provide the details of the algorithm used to solve the RBC dynamical equations in a cylindrical geometry with realistic boundary conditions: no-slip at all the walls, adiabatic on the lateral wall, and isothermal on the horizontal plates. At the end of the chapter, we provide the details on (i) the function used for the distribution of the grids, (ii) numerical schemes used to solve the dynamical convective equations in a cylindrical geometry, and (iii) higher order schemes used to discretize the fields in space.

In **Chapter 3**, we present the results from the Direct Numerical Simulation (DNS)

and related low-dimensional models regarding the dynamics of patterns near the onset for low-Prandtl number ($P = 0.02$, $P = 0.005$, and $P = 0.0002$) convection for r (reduced Rayleigh number) ranging from 1 to 1.25. We perform the DNS in a 3D box on 64^3 grid size with free-slip and conducting boundary conditions on the top and bottom plates, and periodic boundary condition on the lateral walls. In the DNS, we observe various convective patterns: rolls, asymmetric squares, squares, oscillatory asymmetric squares, and chaotic patterns for low-Prandtl number (low-P) convection. To investigate the origin of the patterns and chaos, we identify the active large scale Fourier modes present near the onset from the DNS data and develop a thirty-dimension model for low-P convection. We numerically solve these coupled nonlinear equations of the low-dimensional models and construct bifurcation diagrams for various Prandtl numbers. We find that the static patterns such as rolls, squares, and asymmetric squares are generated as a result of supercritical pitchfork bifurcations, and periodic patterns are generated via Hopf-bifurcation. We observe the presence of chaotic attractors just above the onset for $P \lesssim 0.005$. We present a comprehensive analysis of the route to chaos for these values of P ($P = 0.005$ and $P = 0.0002$) and find that the chaotic attractors are related to the “gluing bifurcations”, “attractors merging crisis” and “homoclinic chaos” phenomena. These results are compared with those for zero-P convection. Furthermore, we find that the bifurcation diagram for low-P is very similar to that for zero-P convection case, except near the onset of convection where 2D stationary rolls, stationary asymmetric squares, and oscillatory asymmetric squares are observed for non-zero Prandtl numbers. We also find that the range of Rayleigh number for which stationary 2D rolls exist decreases rapidly with decreasing Prandtl number. These results are in general agreement with earlier numerical results.

In **Chapter 4**, we compute the spectra and fluxes of the velocity and temperature fields in the inertial range of turbulent RBC using DNS in a 3D rectangular box on 512^3 grids. We consider free-slip conditions for the velocity and isothermal conditions for the temperature on the horizontal plates. We employ periodic conditions for the fields in the horizontal directions. We perform our simulations for the Prandtl numbers of 0, 0.02, 0.2, 1, and 6.8. We present a phenomenology for the nature of the energy spectra for zero-

P and low-P convection which supports Kolmogorov-Obukhov scaling. Our numerical simulations for $P = 0$ and 0.02 are in good agreement with this phenomenology. For large-Prandtl number convection, the system appears to follow Bolgiano-Obukhov scaling (with as the $-11/5$ spectral exponent for the velocity field). We also calculate the heat and viscous dissipation rates using our numerical data and find them to be in reasonably good agreement with their corresponding analytical values. We observe that the temperature spectrum exhibits dual branches for all finite-Prandtl number simulations with the upper branch following a k^{-2} scaling. Using the numerical data, we present a phenomenological model to explain this behaviour. Our study suggests that the lower branch of the spectra participate in the non-linear transfer of energy in the inertial range.

In **Chapter 5**, we analyze the dynamics of reorientations and reversals of the Large Scale Circulation (LSC) in Rayleigh-Bénard convection using direct numerical simulations for air ($P = 0.7$). This simulation was performed in a cylindrical container of aspect ratio of one. We vary R from 6×10^5 to 3×10^7 . For the velocity, we employ no-slip boundary conditions. For the temperature, we employ conducting conditions on the top and bottom plates, and adiabatic condition on the lateral surfaces. We calculate the velocity and temperature fields at eight azimuthal probes placed near the side walls in the middle of the container. We first establish the presence of LSC in our simulation by calculating the autocorrelation function of temperature at these probes. We find the presence of regular oscillations at an interval of one eddy turn-over time in the autocorrelation function. This result is consistent with earlier experimental results on LSC. We calculate the phase and amplitudes of the azimuthal Fourier modes. We show that the phase and amplitude of the first Fourier mode provide interesting information on the orientation and strength of the LSC. Next, we find that during the “complete reversals”, the phase of first Fourier mode changes by an angle of 180° , leading to the reversals of vertical velocity at all the probes. We also observe partial reorientations, in which the phase of the first Fourier mode changes by an angle other than 180° . We observe rotation-led and cessation-led partial and full reorientations of LSC in our numerical simulations. We also report the structure of the flow during rotation-led and cessation-led orientations. We find that the second Fourier mode dominates over the first Fourier mode during the cessation in cessation-

led reorientations, while the first Fourier mode continues to dominate throughout in the rotation-led reorientations. This observation is consistent with the quadrupolar dominant temperature profile observed during cessation-led reorientation. We also observe double-cessation led reorientation in our simulation which is a rare event during the azimuthal reorientations of LSC.

In **Chapter 6**, we present a summary and the conclusions of our studies on the non linear instabilities and turbulence in Rayleigh-Bénard convection. We also propose possible numerical and theoretical extensions of our present work.

In the **Appendix**, we present a phenomenological model to understand the dual branches observed in the temperature (entropy) spectra of non-zero Prandtl numbers. This appendix is based on the results of Chapter 4.



Acknowledgements

Shakespeare says that all the world is a stage and life is a play. I look upon the journey that I have travelled so far in a similar way. We get the stage set by predecessors and play out our individual roles. At each stage of this magnificent play, we come across several coactors and get exposed to their attitudes and thoughts. Our interactions with them strengthen our resolve and encourage us to keep on moving. This thesis is the end of the most exciting journey of my life as a PhD student, which I look upon as the most effective period for nurturing my thoughts and attitudes at different levels. The time has now come when I should express my humble gratitude and thanks to all the people who have played an active role in the successful completion of this journey.

First and foremost, I express my deep sense of gratitude to my thesis supervisor, Prof. Mahendra K. Verma, for giving me an opportunity to work on one of the most exciting fields of fluid dynamics, Rayleigh-Bénard Convection. I thank him for showing his faith in my abilities and giving me unlimited freedom to look at different aspects of this interesting field. It is my pleasure to thank him for his unconditional cooperation and support which I have received during the course of my PhD work. I must acknowledge all the vibrant and exciting scientific discussions I had with him, which always inspired and motivated me to look at things more positively whenever I would find myself on a rocky path. Working with him has been a wonderful experience and shall always be a part of my memories.

Thanks are due to my Peer Review Committee members Prof. Harshawardhan Wanare and Prof. A. Ramakrishnan whose constant encouragement and inputs helped me to finish my PhD in the stipulated time period.

I acknowledge all the teachers of the Physics Department from whom I received a rigorous training during my course work studies. Specifically, I would like to thank Prof. D. Chowdhury, Prof. S. D Jogleker, Prof. R. Prasad, Prof. K. P. Rajeev, Prof. V. Subrahmanyam, and Prof. Mahendra K. Verma for introducing me the different realms of Physics. I would also like to acknowledge Prof. S. Mukherjee, Prof. S. Bhattacharjee,

Prof. Zakir Hossain, Prof. V. Ravishankar, Prof. Manoj K. Harbola, Prof. G. Sengupta, and Prof. T. Sarkar under whom I did not have the opportunity taking any course, but with whom discussions at different moments have played a very crucial role in keeping up my enthusiasm and energy.

It is my pleasure to express my deep sense of gratitude to all of our group collaborators. I greatly benefitted from their expertise and experience during the course of my work. I would like to acknowledge Prof. Krishna Kumar (IIT Kharagpur) for introducing me to the vast field of Rayleigh-Bénard Convection when I visited IITKgp in the summer of 2007. I acknowledge him for sharing his rich experience in different fields of fluid dynamics. I thank Prof. Pankaj Wahi for his kind help in analyzing the bifurcation diagrams for low-Prandtl number convection. The discussions with him on several other problems are gratefully acknowledged. I acknowledge my fruitful collaboration with Dr. Supriyo Paul and Dr. Pinaki Pal on zero-Prandtl number convection. I also acknowledge Dr. Supriyo Paul for introducing me to several software packages which are being used for the visualization of fluid dynamics. Above all, I express my high regard for him for all the computation-related help that I received from him at the various stages of my work. I would like to acknowledge Prof. Vinayak Eswaran and Dr. Arnab De for their fruitful collaboration on the dynamics of Large Scale Circulation. I thank Arnab for sharing his finite-difference code which I used for the study. The kind suggestions and advice of Prof. Eswaran are also acknowledged.

I thank all my lab mates – Ambarish, Dinesh, Haider, Mani, Rakesh, Rohit, and Sandeep – for their cooperation and for maintaining a healthy academic environment in the lab.

I would like to acknowledge my association with Prof. Debashish Chowdhury at the early stage of my research career. My interaction with him provided opportunity for me to look at things from a physicist's point of view. I cherish all the moments spent with him. I also acknowledge the comments and advice of Prof. Amit Dutta and Prof. Anjan Gupta, they being a part of my Three Men Committee at the early stage of PhD program.

I would like to thank all the leading experts working in this field with whom I have interacted at various scientific meets. My sincere thanks to Prof. Stephen Fauve, Prof. K. R. Sreenivasan, and Prof. J. J. Niemela for sharing their experiences related with experiments in Rayleigh-Bénard Convection. I would like to acknowledge Prof. Itamar Procaccia for his stimulating discussions and for enlightening me on the various theoretical challenges in the field of turbulence.

I would like to acknowledge all the staff members of the Physics Department for their kind cooperations, support, and ever willingness to help no matter how difficult problems were. My special thanks are due to Mr. G. R. Hoshing, Mr. Arvind Verma, Mr. Khan, Mr. Murlidhar, and Mr. G. Narayan for their kind cooperations on different official matters. I would like to thank Mr. Arvind Mishra for all the computation related help which I have received from him at different points of time.

During my brief stay in IIT Kanpur, I came across several friends who made the journey very pleasant and colourful. I acknowledge all the love and cooperation that I have received from them at different stages of my PhD. I thank Abhishek, Anurag, Andrew, Awanish, Bhaskar, Debjit, Debashish, Shyam, Saurabh, Vivek Anand, Tripti, Saumyadip, Soumen, Subhayan, Subhadip, Aswath, D. D. B. Rao, Subrat Das, Lipsa, Sunil, Sudhakar, Goutam Roy (Boga Da), Kavijee, Vijay Bisht, Deven, Ashok Garai, Bhaskarjit Neog, Neeraj, and many other friends whose company I really cherished during my PhD and whose memories will always be an integral part of my life. My special thanks are due to Anurag for always showing his great interests to discuss several aspects of Physics whenever I approached him.

This work would not have been possible without the computational facilities at EKA, Pune, and the CHAOS Cluster at IIT Kanpur. I would specially like to thank the staffs of EKA for their kind cooperation and support in successfully running the code.

Above everything, this PhD would not have been possible without the constant support, encouragement, blessings and good wishes of my family members. I will never be able to repay their unconditional support and the personal sacrifices that they have made, those that made it possible for me to accomplish this task. My special thanks are due to my elder brother, Mr. Amrendra Mishra, and my younger brother, Mr. Sanjeev Mishra, for their kind support and encouragement throughout my PhD.

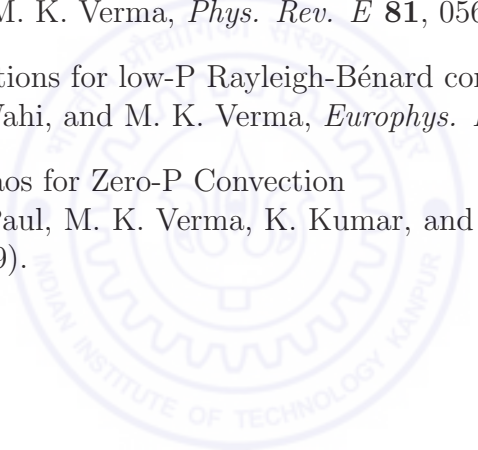
As an honest truth-seeker, I am grateful to Nature for stimulating us to discover her manifold secrets.

Pankaj Kumar Mishra

To my parents...



Publications

1. Dynamics of reorientations and reversals of large scale flow in Rayleigh-Bénard Convection
P. K. Mishra, A. K. De, M. K. Verma, and V. Eswaran, *J. Fluid Mechanics* (2010) (In press), *arXiv:1003.2102v4* (2010).
 2. Energy Spectra and Fluxes for Rayleigh-Bénard Convection
P. K. Mishra and M. K. Verma, *Phys. Rev. E* **81**, 056316 (2010).
 3. Patterns and bifurcations for low-P Rayleigh-Bénard convection
P. K. Mishra, P. Wahi, and M. K. Verma, *Europhys. Lett.* **89**, 44003 (2010).
 4. Bifurcations and Chaos for Zero-P Convection
P. Pal, P. Wahi, S. Paul, M. K. Verma, K. Kumar, and **P. K. Mishra**, *Europhys. Lett.* **87**, 54003 (2009).
- 

Contents

Synopsis	iv
Acknowledgement	x
Publications	xvi
List of figures	xix
1 Introduction	1
1.1 Rayleigh-Bénard Convection	1
1.1.1 Governing equations and parameters of RBC	2
1.2 RB Convection near the onset	7
1.2.1 Patterns and chaos for low-Prandtl number convection	9
1.2.2 Patterns and chaos for zero-Prandtl number convection	13
1.3 Turbulent RBC	14
1.3.1 Scalings of energy spectra in the inertial range of turbulent RBC . .	14
1.3.2 Large scale circulation and its associated dynamics in turbulent RBC	20
1.4 Outline of the subsequent chapters	24
2 Direct numerical simulation of Rayleigh-Bénard convection: numerical details	28
2.1 Pseudo-spectral code for a 3D box	29
2.1.1 Numerical methods	29
2.1.2 Initial conditions	31
2.1.3 Calculation of the spectrum and flux	33
2.2 Finite-difference code for simulating convection in a cylindrical geometry .	34
2.2.1 Governing equations	34
2.2.2 Numerical techniques	37
2.2.3 Predictor-corrector method	38
2.2.4 Solution algorithm	41
2.2.5 Discretization of the fields and other numerical details	42
3 Patterns and chaos in low-P and zero-P convection	44
3.1 Introduction	44
3.2 Bifurcation analysis of low-P RBC	46
3.2.1 Direct numerical simulations for low-P convection	46

3.2.2	Low-dimensional model	50
3.2.3	Bifurcations for low- P convection	51
3.3	Zero- P Convection	62
3.3.1	Low-dimensional model	63
3.4	Conclusion	68
4	Energy spectra and fluxes for Rayleigh-Bénard convection	69
4.1	Introduction	69
4.2	Governing equations	71
4.3	Numerical simulations and results	73
4.3.1	Prandtl number $P = 0$	76
4.3.2	Prandtl number $P = 0.02$	77
4.3.3	Prandtl number $P = 0.2$	81
4.3.4	Prandtl number $P = 1$	84
4.3.5	Prandtl number $P = 6.8$	86
4.4	Conclusions	88
5	Dynamics of large scale flow in Rayleigh-Bénard convection	93
5.1	Introduction	93
5.2	Simulation details	95
5.3	Numerical results	99
5.3.1	Large scale circulation	99
5.3.2	Measure of reorientations of LSC	102
5.3.3	Dynamics of reorientations	108
5.4	Discussion and conclusions	116
6	Conclusion and future work	119
6.1	Main conclusions of the thesis	119
6.2	Scope for future work	121
A	Appendix	123
A.1	Entropy spectrum	123
	Bibliography	126

List of Figures

1.1	Plot showing transitions in convection as a function of the Rayleigh and Prandtl numbers [adapted from Krishnamurti and Howard, PNAS (1981) [6]]. The curve indicates the onset of steady rolls (I), three-dimension steady convection patterns (II), time dependent convection (III), and turbulent flow (IV). Symbols denote the dynamical structure of the flows in different regime: \circ , steady roll; \bullet , time-dependent cellular flow; and \sim , large-scale flow.	7
2.1	Schematic diagram of the cylindrical cell used for our study. Isothermal conditions on the horizontal walls and adiabatic condition on lateral walls are applied for the temperature. No-slip conditions for velocity fields are applied on all the walls. Circular lines show the locations of the ideal probes inserted at different locations of the container to characterize the temporal behaviour of RBC flow.	35
2.2	Schematic diagram of the physical (r, ϕ, z) and computational (ξ, η, ζ) domain of the simulation in a cylindrical geometry. The grids are non-uniform in the physical domain and uniform in the computational domain.	36
2.3	Distribution of $100 \times 120 \times 201$ grids in (a) a horizontal ($z = 0.5$), and (b) a vertical ($\theta = 3\pi/4$) plane of a cylindrical container of aspect ratio one.	42
3.1	Static patterns in the mid-plane of the 3D convection box observed in DNS near the onset for $P = 0.02$ on a 64^3 grid. Temperature snapshots at: (a) $r = 1.0005$ exhibits a roll pattern, (b) $r = 1.007$ exhibits a “weak” asymmetric square (ASQ) pattern, (c) $r = 1.186$ exhibits a “strong” asymmetric square (ASQ) pattern, and (d) $r = 1.217$ exhibits a square (SQ) pattern. Blue and red regions represent, respectively, the downflow and upflow of the convection.	47
3.2	Relaxation oscillation with an intermediate square regime (SQOR) pattern observed in the DNS at $r = 1.031$ for $P = 0.02$. Snapshots of temperature at: (a) $t = 0$, (b) $t = T/4$, and (c) $t = T/2$, where T is the time period of the oscillation.	48
3.3	Oscillating asymmetric square (OASQ) pattern observed in the DNS for $P = 0.02$ at $r = 1.110$. Snapshots of temperature at: (a) $t = 0$, (b) $t = T/2$, where T is the time period of the oscillation.	49

3.4	For $P = 0.02$, the three-dimensional view of the bifurcation diagram computed from the low-dimensional model exhibiting stable fixed points (solid curves), and unstable fixed points (dashed curves). The purple solid and dashed lines represent the stable and unstable 2D roll solutions respectively. The black, blue, and cyan curves depict stationary squares (SQ), asymmetric stationary squares (ASQ), and the conduction state, respectively. This Figure is taken from [38].	54
3.5	Bifurcation diagram of the low-dimensional model for $P = 0.02$ in the range $0.95 \leq r \leq 1.25$. The stable branches corresponding to the conduction state, 2D rolls, SQ, and ASQ are represented by solid cyan, solid purple, solid black, and solid blue curves respectively. The red and green curves depict the extrema of OASQ and SQOR, respectively. The dashed curves represent unstable solutions. This Figure is taken from [38].	55
3.6	Phase space projection on the $W_{101} - W_{011}$ plane is shown to make a comparison between the DNS results and the model results in the OASQ and the SQOR regimes of convection for $P = 0.02$. Red and blue curves show the results obtained from the DNS and the model, respectively. (a) The limit cycle obtained in DNS at $r = 1.016$. (b) The limit cycle obtained in model for $r = 1.0129$. (c) The homoclinic orbit obtained in DNS at $r = 1.027$. (d) The homoclinic orbit at $r = 1.0184$ for model. The black dots shown in (b) and (d) indicate the symmetric square saddle points. Note that the two limit cycles corresponding to OASQ in the homoclinic orbit are very close but they don't touch each other.	56
3.7	(a) The time series of W_{101} and W_{011} . (b) The phase space projection on the $W_{101}-W_{011}$ plane in the SQOR regime for $P = 0.02$ at $r = 1.034$	57
3.8	Bifurcation diagram of the low-dimensional model for $P = 0.005$ in the range $0.95 \leq r \leq 1.25$. The colour convention is the same as that for $P = 0.02$ (Fig. 3.5). The chaotic attractors are shown in brown. A zoomed view of the bifurcation diagram for the chaotic regime is shown in the inset where the x -axis is chosen as $\log(r - 1)$ to highlight the behaviour near $r = 1$. The three attractors <i>Ch1</i> , <i>Ch2</i> and <i>Ch3</i> are shown as (i), (ii), and (iii), respectively. This Figure is taken from [38].	58
3.9	Phase space projections of the attractors on the $W_{101}-W_{011}$ plane obtained from the low-dimensional model for $P = 0.005$ near $r = 1$: (a) two of the limit cycles at $r = 1.0006844$; (b) the chaotic attractor <i>Ch3</i> at $r = 1.0023$; (c) the chaotic attractor <i>Ch2</i> at $r = 1.0053$; (d) the chaotic attractor <i>Ch1</i> at $r = 1.0064$, with the inset depicting the chaotic nature of the attractor. This Figure is taken from [38].	61
3.10	Phase space projections of the chaotic attractors on the $W_{101}-W_{011}$ plane obtained from DNS with $P = 0.005$: (a) <i>Ch3</i> for $r = 1.0023$; (b) <i>Ch1</i> for $r = 1.0068$. The insets show an enlarged view of the boxed region. This Figure is taken from [38].	62
3.11	Bifurcation digram of the low-dimensional model for $P = 0.0002$ in the range $0.95 \leq r \leq 1.25$. The colour convention is same as that for $P = 0.005$ (Fig. 3.8). This Figure is taken from [38].	63

3.12	Three-dimensional view of the bifurcation diagram showing the fixed points with solid and dashed curves representing the stable and unstable fixed points, respectively. Black, blue, and cyan curves represent stationary squares (SQ), asymmetric stationary squares (ASQ), and the conduction state, respectively. All the points on the axis (purple lines) are 2D roll solutions. Below the 3D diagram, we plot the values of W_{101} and W_{011} vs. r . These plots indicate xy symmetry in the system. This Figure is taken from [43].	65
3.13	Bifurcation diagram of the model for $0.95 \leq r \leq 1.4$. The stable branches corresponding to stationary squares (SQ) and stationary asymmetric squares (ASQ) are represented by solid black and solid blue lines, respectively. Red, green, and brown curves represent the extrema of oscillatory asymmetric squares (OASQ), relaxation oscillation of squares (SQOR), and chaotic solutions respectively. A zoomed view of the bifurcation diagram for the chaotic regime is shown in the inset. In the inset, the x -axis is chosen as $\log(r - 1)$ to highlight the behaviour near $r = 1$. Branches corresponding to the unstable fixed points are represented by dashed lines. The cyan line represents the conduction state. This Figure is taken from [43].	66
3.14	The three different chaotic solutions observed near $r = 1$: Ch1 at $r = 1.0041$ for the model (a) and at $r = 1.0045$ in DNS (b); Ch2 at $r = 1.0038$ for the model (c) and at $r = 1.0030$ in DNS (d); Ch3 at $r = 1.0030$ for the model (e) and at $r = 1.0023$ in DNS (f). These solutions belong to (i), (ii), and (iii) regimes in the bifurcation diagram (Fig. 3.13). This Figure is taken from [43].	67
4.1	For $R = 6.6 \times 10^6$ and $P = 6.8$: (a) the vertical variation of the velocity fluctuations averaged over the horizontal planes. The solid, dashed, and dotted lines represent the rms values of u_x^{rms} , u_y^{rms} , and u_z^{rms} , respectively; and (b) the vertical variation of the horizontally averaged mean temperature. This Figure is taken from [122].	74
4.2	Plot of the compensated kinetic energy spectra $E^u(k)k^{5/3}$ (KO) and $E^u(k)k^{11/5}$ (BO) vs. k for $R = 1.97 \times 10^4$ and $P = 0$ on a 256^3 grid. The DNS spectrum matches with the KO spectrum quite well. This Figure is taken from [122].	77
4.3	Plot of the kinetic energy flux vs. k for $R = 1.97 \times 10^4$ and $P = 0$ on a 256^3 grid. The constancy of the flux in the inertial range indicates that zero-P convection follows Kolmogorov's scaling. This Figure is taken from [122]. .	78
4.4	Plot of the compensated kinetic energy spectra $E^u(k)k^{5/3}$ (KO) and $E^u(k)k^{11/5}$ (BO) vs. k for $R = 2.6 \times 10^6$ and $P = 0.02$ on a 512^3 grid. The KO scaling is in better agreement than the BO scaling. This Figure is taken from [122].	79
4.5	Plot of the entropy spectrum for $R = 2.6 \times 10^6$ and $P = 0.02$ on a 512^3 grid. The exponential fit in the inset indicates the diffusive nature of the entropy spectrum. The upper part of the entropy spectrum corresponds to the $\theta(0, 0, 2n)$ modes. This Figure is taken from [122].	81

4.6	Plot of the kinetic energy flux (solid line) and the entropy flux (dashed line) vs. k for $R = 2.6 \times 10^6$ and $P = 0.02$ on a 512^3 grid. The kinetic energy flux is constant in a narrow inertial range, indicating agreement with Kolmogorov's scaling for the velocity field. The entropy flux appears to decay rather sharply suggesting diffusive entropy spectrum. This Figure is taken from [122].	82
4.7	Plot of the compensated kinetic energy spectra $E^u(k)k^{5/3}$ (KO) and $E^u(k)k^{11/5}$ (BO) vs. k for $R = 6.6 \times 10^6$ and $P = 0.2$ on a 512^3 grid. The numerical results match better with the KO scaling than the BO scaling. This Figure is taken from [122].	83
4.8	Plot of the entropy spectrum vs. k for $R = 6.6 \times 10^6$ and $P = 0.2$ on a 512^3 grid. The lower part of the entropy spectrum matches better with KO scaling than BO scaling. The upper part of the entropy spectrum corresponds to the $\theta(0, 0, 2n)$ modes, and is in general agreement with the k^{-2} fit. This Figure is taken from [122].	84
4.9	Plot of the kinetic energy flux (solid line) and the entropy flux (dashed line) vs. k for $R = 6.6 \times 10^6$ and $P = 0.2$ on a 512^3 grid. The kinetic energy and entropy fluxes are constant in the narrow inertial range indicating a general agreement with the KO scaling. This Figure is taken from [122].	85
4.10	Plot of the compensated kinetic energy spectra $E^u(k)k^{5/3}$ (KO) and $E^u(k)k^{11/5}$ (BO) vs. k for $R = 6.6 \times 10^6$ and $P = 1$ on a 512^3 grid. We cannot infer which phenomenology fits better with the plots. This Figure is taken from [122].	86
4.11	Plot of the entropy spectrum vs. k for $R = 6.6 \times 10^6$ and $P = 1$ on a 512^3 grid. Both the KO and BO lines do not fit with the lower branch of the entropy spectrum. The upper part of the entropy spectrum matches with k^{-2} quite well. This Figure is taken from [122].	87
4.12	Plot of the kinetic energy flux (solid line) and the entropy flux (dashed line) vs. k for $R = 6.6 \times 10^6$ and $P = 1$ on a 512^3 grid. The dotted line represents the $\Pi^u(k)k^{4/5}$ curve. The flux results are inconclusive about the nature of the scaling. This Figure is taken from [122].	88
4.13	Plot of the compensated kinetic energy spectra $E^u(k)k^{5/3}$ (KO) and $E^u(k)k^{11/5}$ (BO) vs. k for $P = 6.8$ and $R = 6.6 \times 10^6$ on a 512^3 grid. The fit is somewhat inconclusive, yet the BO scaling appears to fit better with the numerical data than the KO scaling. This Figure is taken from [122].	89
4.14	Plot of the entropy spectrum $E^\theta(k)$ vs. k for $P = 6.8$ and $R = 6.6 \times 10^6$ on a 512^3 grid. Even though both the KO and BO lines do not fit well with the data, the BO line is closer to the lower part of the spectrum. The upper branch matches with k^{-2} quite well. This Figure is taken from [122].	90
4.15	Plot of the kinetic energy flux (solid line) and the entropy flux (dashed line) vs. k for $R = 6.6 \times 10^6$ and $P = 6.8$ on a 512^3 grid. The normalized kinetic energy flux (multiplied by $k^{4/5}$) is also shown in the figure as a dotted line. $\Pi^u(k)k^{4/5}$ and $\Pi^\theta(k)$ are constant for a range of wavenumbers. This Figure is taken from [122].	91

-
- 5.1 (a) Some of the velocity and temperature probes placed inside the cylinder. For most of our discussions in this chapter, we use the probes at $z = 0.5$, $r = 0.48$, and $\theta = j\pi/4$ with $j = 0 : 7$ as shown in the figure. (b) Temperature profile in the vertical plane $\theta = 3\pi/4$ for $R = 2 \times 10^7$ on a $100 \times 120 \times 201$ grid. A hot plume ascends from the right wall and a cold plume descends from the left wall confirming the presence of a large scale structure. (c) Temperature profile in the horizontal section $z = 0.5$ for $R = 2 \times 10^7$ on a $100 \times 120 \times 201$ grid. This Figure is taken from [131]. 98
- 5.2 Plot of the autocorrelation function $g_c(\tau) = \langle \delta T(t)\delta T(t + \tau) \rangle / \sigma_T^2$ vs. delay time τ (in units of large eddy turnover time) for a probe at $r = 0.48$, $\theta = 0$, and $z = 0.5$: (a) $R = 6 \times 10^5$ on a $(33 \times 49 \times 97)$ grid, (b) $R = 8 \times 10^6$ on a $75 \times 96 \times 145$ grid, (c) $R = 2 \times 10^7$ on a $100 \times 120 \times 201$ grid, and (d) $R = 3 \times 10^7$ on a $100 \times 120 \times 201$ grid. The insets show oscillations on the eddy turn-over time scale. This Figure is taken from [131]. 100
- 5.3 For $R = 2 \times 10^7$ on a $100 \times 120 \times 201$ grid, the cross-correlation function between the temperature measured at two azimuthally opposite probes at $\theta = 0$ and $\theta = \pi$ in the mid-plane at $r = 0.48$. The inset shows oscillations on the eddy turn-over time scale. This Figure is taken from [131]. 101
- 5.4 For $R = 6 \times 10^5$ on a $33 \times 49 \times 97$ grid, the time series of the vertical velocity measured by the probes at $z = 0.5$ (mid- plane) and $r = 0.48$ for: (a) $\theta = 0$ and $\theta = \pi$, (b) $\theta = \pi/4$ and $\theta = 5\pi/4$, (c) $\theta = \pi/2$ and $\theta = 3\pi/2$, and (d) $\theta = 3\pi/4$ and $\theta = 7\pi/4$. The time series of the phase of the first Fourier mode of the vertical velocity (δ_1) is shown in subfigure (e). Time is measured in units of the free-fall time $d/\sqrt{\alpha g(\Delta T)d}$. The arrows (inside the boxed regions) in (e) indicate a partial reorientation ($\delta_1 \simeq 135^\circ$) near $t \simeq 2700$, and a complete reversal ($\delta_1 = 180^\circ$) near $t \simeq 3900$. This Figure is taken from [131]. 103
- 5.5 For $R = 8 \times 10^6$ on a $75 \times 96 \times 145$ grid, the time series of the vertical velocity measured by the probes at $z = 0.5$ (mid- plane) and $r = 0.48$, and the phase of the first Fourier mode of the vertical velocity. Details of the figures are the same as in Fig. 5.4. A complete reversal of the flow occurs in the boxed region. This Figure is taken from [131]. 104
- 5.6 For $R = 2 \times 10^7$ on a $100 \times 120 \times 201$ grid, the time series of the vertical velocity measured by the probes at $z = 0.5$ (mid- plane) and $r = 0.48$, and the phase of the first Fourier mode of the vertical velocity. Details of the figures are the same as in Fig. 5.4. A complete reversal of the flow occurs in the boxed region. This Figure is taken from [131]. 106
-

-
- 5.7 Azimuthal profile of the vertical velocity at $z = 0.5$ and $r = 0.48$ before (solid line) and after reorientation (dashed line): (a) $R = 2 \times 10^7$ at $t = 695$ & 750, (c) $R = 6 \times 10^5$ at $t = 2548$ & 2850, and (e) $R = 6 \times 10^5$ at $t = 3400$ & 4050. During the reorientations the phase of the first Fourier mode changes by $\Delta\delta_1 = 180^\circ$, 135° , and 180° , respectively. For the reoriented time series, we subtract $\Delta\delta_1$ from the positive k modes, add $\Delta\delta_1$ to the negative k modes, and construct a modified velocity profile (dotted line). As seen in the sub-figures (b), (d), and (f), the reconstructed velocity profiles match quite well with the profiles before the reorientation. This Figure is taken from [131]. 107
- 5.8 Time series of the phase of the first Fourier mode δ_1 (in units of 2π), amplitude of the first Fourier mode $|\hat{u}_1|$, and amplitude of the second Fourier mode $|\hat{u}_2|$ during the rotation-led reversals. Panels (a), (b), (c), and (d) show the time series of δ_1 , $|\hat{u}_1|$, $|\hat{u}_2|$, and $|\hat{u}_2|/|\hat{u}_1|$, respectively, for $R = 6 \times 10^5$ on a $33 \times 49 \times 97$ grid in which the reversal takes place near $t = 3950$. (e), (f), (g), and (h) show the time series of δ_1 , $|\hat{u}_1|$, $|\hat{u}_2|$, and $|\hat{u}_2|/|\hat{u}_1|$, respectively, for $R = 2 \times 10^7$ on a $100 \times 120 \times 201$ grid with a reorientation event near $t = 700$. This Figure is taken from [131]. 108
- 5.9 Time series of δ_1 , $|\hat{u}_1|$, $|\hat{u}_2|$, and $|\hat{u}_2|/|\hat{u}_1|$ indicating cessation-led reorientation near $t \sim 1175$ for $R = 8 \times 10^6$ on a $75 \times 96 \times 145$ grids. The strength of $|\hat{u}_1|$ decreases significantly, while $|\hat{u}_2|/|\hat{u}_1|$ increases during this event. This Figure is taken from [131]. 109
- 5.10 Time series of δ_1 , $|\hat{u}_1|$, $|\hat{u}_2|$, and $|\hat{u}_2|/|\hat{u}_1|$ indicating cessation-led partial reorientations near $t \sim 6625$ and 6710 for $R = 6 \times 10^5$ ($33 \times 49 \times 97$ grid). For both the events $\Delta\delta_1 \approx 72^\circ$. This Figure is taken from [131]. 110
- 5.11 Time series of δ_1 , $|\hat{u}_1|$, $|\hat{u}_2|$, and $|\hat{u}_2|/|\hat{u}_1|$ indicating double-cessation for $R = 6 \times 10^5$ on a $33 \times 49 \times 97$ grid. The first cessation occurs at $t \sim 2083$ and second one occurs at $t \sim 2088$. During both the events, $|\hat{u}_1|$ becomes weak and $|\hat{u}_2|$ dominates. Panel (d) shows the two spikes in $|\hat{u}_2|/|\hat{u}_1|$ during these events. This Figure is taken from [131]. 111
- 5.12 Time series of δ_1 , $|\hat{u}_1|$, $|\hat{u}_2|$, and $|\hat{u}_2|/|\hat{u}_1|$ indicating double-cessation for $R = 6 \times 10^5$ on a $33 \times 49 \times 97$ grid. The first cessation at $t \sim 2464$ is followed by the second at $t \sim 2466$. During both the events, $|\hat{u}_1|$ becomes weak and $|\hat{u}_2|$ dominates. Panel (d) shows the two spikes in $|\hat{u}_2|/|\hat{u}_1|$ during these events. This Figure is taken from [131]. 112
- 5.13 Time series of δ_1 , $|\hat{u}_1|$, $|\hat{u}_2|$, and $|\hat{u}_2|/|\hat{u}_1|$ for $R = 6 \times 10^5$ depicting events similar to double cessations on a $33 \times 49 \times 97$ grid. $\Delta\delta_1 \sim 72^\circ$ near $t \sim 4270$, while $\Delta\delta_1 \approx 0$ near $t \sim 4540$. During both the events, $|\hat{u}_1| \rightarrow 0$ while the ratio $|\hat{u}_2|/|\hat{u}_1|$ increases significantly. This Figure is taken from [131]. 113
- 5.14 The distribution of the change in the phase of the first Fourier mode ($|\Delta\delta_1|$) of LSC during reorientations. The criteria of Brown *et al.* [84] and Brown and Ahlers [85] have been used for identifying reorientations of the LSC. This Figure is taken from [131]. 114
-

- 5.15 Temperature snapshots at the mid-plane ($z = 0.5$) during cessation-led reorientations near $t \sim 2087$ and 4539 for $R = 6 \times 10^5$. Dipolar structures are dominant before and after the reorientations, but quadrupolar structures are prominent during the reorientations (at $t = 2087$ & 4539). The horizontal black lines are drawn as a reference line which provide a guide to the azimuthal reorientations of the convective structure. This Figure is taken from [131]. 115



Chapter 1

Introduction

1.1 Rayleigh-Bénard Convection

Thermal convection has been of major interest to the scientific community owing to its ubiquitous presence in many natural flows and its potential applications in science and engineering [1, 2, 3, 4]. For instance, many solar and stellar structures depend critically on the nature of heat transport from the core to the surface. Convection in Earth's mantle is responsible for the movement of the tectonic plates, which is of major interest to geophysicists. Convection plays an active role in the generation of magnetic fields within the earth's core, and it is possibly responsible for the reversal of the geomagnetic field. In the atmosphere, convection is an important factor in weather prediction at small length and time scales, and for climate prediction at large time scales. In the oceans, convection is responsible for the mixing of water masses. Convection is not only confined to natural flows, it is also manifest in various forms in industrial applications, for example in nuclear reactors, crystallization processes, solar heating devices, etc.

From the basic science point of view, thermal convection is one of the few systems in which various instabilities, spatio-temporal chaos, and soft and hard turbulence are observed. Among convective systems, Rayleigh-Bénard convection (RBC) is an ideal system in which fluid in a closed box is heated from below and cooled from above. In the present thesis, we focus on some of the instabilities, chaos, and the turbulent aspects of RBC.

1.1.1 Governing equations and parameters of RBC

The governing hydrodynamical equations of RBC flow are

$$\frac{\partial \mathbf{u}}{\partial t} + (\mathbf{u} \cdot \nabla) \mathbf{u} = -\frac{1}{\rho_0} \nabla \sigma + \frac{1}{\rho_0} \rho(T) g \hat{z} + \nu \nabla^2 \mathbf{u}, \quad (1.1)$$

$$\frac{\partial T}{\partial t} + (\mathbf{u} \cdot \nabla) T = \kappa \nabla^2 T, \quad (1.2)$$

$$\nabla \cdot \mathbf{u} = 0, \quad (1.3)$$

where $\mathbf{u} = (u_1, u_2, u_3)$ is the velocity field, T is the temperature field, σ is the pressure field, and \hat{z} is the buoyancy direction. ν is the kinematic viscous coefficient, κ is the thermal diffusivity coefficient, ρ_0 is the fluid density at a reference temperature, and $\rho(T)$ is the density of the fluid at temperature T . We assume Boussinesq approximation under which all the properties (e.g., ν, κ) of the fluid are considered to be independent of the temperature, and the fluid is considered to be incompressible except for the buoyancy term. Note that the buoyancy force depends on the linear variation of density as a function of temperature ($\rho \propto -\rho_0(1 - \alpha T)$, where α is the heat expansion coefficient). The Boussinesq approximation is valid for small temperature differences between the top and bottom plates.

Generally two types of containers are used for the study of an RBC system: (i) a Rectangular box, and (ii) a Cylindrical container. In the following, for the sake of simplicity, we define the problem for the rectangular box geometry which can be easily generalized to the cylindrical geometry. We consider that the fluid is confined in a box with dimension $L_x \times L_y \times d$, where L_x and L_y are the lengths in x and y directions respectively, and d is the vertical height of the container. In the experiment, the top and bottom plates are kept at constant temperatures, i.e.,

$$T|_{z=0} = T_H, \quad T|_{z=d} = T_C, \quad (1.4)$$

where T_H and T_C are the temperatures of the lower (hot) and upper (cold) horizontal plates of the container, respectively. Quite often, the temperature of the dynamical system is expressed as a sum of the linear profile of the conduction state and the temperature

fluctuation $\theta(\mathbf{x}, t)$, i.e,

$$T(\mathbf{x}, t) = T_H - \frac{\Delta T}{d}z + \theta(\mathbf{x}, t), \quad (1.5)$$

where $\Delta T = T_H - T_C$. Then the Boussinesq equations, Eqs. (1.1) - (1.3), become

$$\frac{\partial \mathbf{u}}{\partial t} + (\mathbf{u} \cdot \nabla) \mathbf{u} = -\frac{1}{\rho} \nabla \sigma + \nu \nabla^2 \mathbf{u} + \frac{1}{\rho} \alpha g \theta \hat{z}, \quad (1.6)$$

$$\frac{\partial \theta}{\partial t} + (\mathbf{u} \cdot \nabla) \theta = \frac{\Delta T}{d} u_3 + \kappa \nabla^2 \theta, \quad (1.7)$$

$$\nabla \cdot \mathbf{u} = 0. \quad (1.8)$$

Note that an additional term from the body force has been absorbed into the pressure term:

$$\sigma \rightarrow \sigma + \alpha g \left(\frac{\Delta T}{2d} z^2 - T_H z \right). \quad (1.9)$$

The boundary condition for θ at the top and bottom plates would imply that

$$\theta|_{z=0} = 0 = \theta|_{z=d}. \quad (1.10)$$

For the velocity field, the typical boundary conditions used are no-slip and free-slip at the thermal plates. Under no-slip conditions,

$$\mathbf{u}|_{z=0} = 0 = \mathbf{u}|_{z=d}, \quad (1.11)$$

while for the free-slip or stress-free conditions,

$$\begin{aligned} u_3|_{z=0} = 0 = u_3|_{z=d}, \\ \partial_z u_1|_{z=0} = 0 = \partial_z u_1|_{z=d}, \quad \partial_z u_2|_{z=0} = 0 = \partial_z u_2|_{z=d}. \end{aligned} \quad (1.12)$$

For the lateral walls, different choices of boundary conditions are possible: (a) adiabatic for temperature and no-slip for velocity, (b) free-slip for velocity and adiabatic/periodic

for temperature, and (c) periodic for both the fields. Quite often periodic conditions for the fields are considered to ignore the effects of the side walls. Note that typical experiments have no-slip boundary conditions at all the walls. However free-slip boundary conditions are appropriate in situations when the convective fluid of high viscosity is confined between the fluid having low viscosity. Eqs. (1.6)-(1.8) with the boundary conditions in Eq. (1.10) and those either Eq. (1.11) or Eq. (1.12) is called the *Rayleigh-Bénard* problem.

The dimensional equations of RBC contain various dynamical parameters such as thermal expansion coefficient (α), acceleration due to gravity (g), thermal diffusion coefficient (κ), viscous diffusion coefficient (ν), etc. However, owing to the self-similar nature of the dynamics, this large number of parameters can be reduced to the compact form by choosing a relevant length scale, time scale, velocity scale, and temperatures scale present in the RBC system. In RBC, the characteristic length scale is the distance ‘ d ’ between the top and bottom plates. There are three time scales: (a) heat diffusion time scale given by d^2/κ , (b) viscous diffusive time scale given by d^2/ν , and (c) free-fall time scale given by $d/\sqrt{\alpha g \Delta T d}$. The characteristic temperature scale is ΔT . If one choose d as a length scale, d^2/ν as a time scale (and thus ν/d for the velocity scale), and $\nu \Delta T/\kappa$ as a scale for the temperature, the corresponding non-dimensional equations of the RBC system will be

$$\frac{\partial \mathbf{u}}{\partial t} + (\mathbf{u} \cdot \nabla) \mathbf{u} = -\nabla \sigma + R \theta \hat{z} + \nabla^2 \mathbf{u}, \quad (1.13)$$

$$P \left(\frac{\partial \theta}{\partial t} + \mathbf{u} \cdot \nabla \theta \right) = u_3 + \nabla^2 \theta, \quad (1.14)$$

$$\nabla \cdot \mathbf{u} = 0, \quad (1.15)$$

where $R = \frac{\alpha g \Delta T d^3}{\nu \kappa}$ is the Rayleigh number, and $P = \frac{\nu}{\kappa}$ is the Prandtl number. These two dimensionless quantities, together with the boundary conditions, characterize the convection problem in the Boussinesq approximation.

The Prandtl number (P) is the ratio of the heat diffusion time scale and the viscous diffusion time scale of the system. It measures the relative importance of the advection of momentum with heat advection, thus affecting the non-linear properties of the convection

accordingly. The values of Prandtl number vary from 10^{-8} for the sun's convective zone to 10^{23} for Earth's mantle. The values of P for some fluids are listed in Table 1.1. In the literature, the fluids with $P < 1$ are considered as low-Prandtl number fluid, while those with $P > 1$ are considered as high-Prandtl number fluid. Another parameter, the Rayleigh number (R) is proportional to the temperature difference (ΔT) applied between the bottom and top plates, and relates the strength of the destabilizing mechanism (buoyancy force) to the stabilizing processes (viscous diffusion and thermal diffusion). These two non-dimensional parameters are the main control parameters for RBC. The other control parameter that critically affects the dynamics of RBC is the aspect ratio (τ) of the container. It is the ratio of the horizontal and the vertical dimension of the container, and it plays a crucial role in determining the convective patterns of the flow.

Table 1.1: Typical value of Prandtl number for different fluids.

	Sun	Sodium (liquid)	Mercury	Air	Water	Silicon oils	Glycerine	Earth's Mantle
P	10^{-8}	0.01	0.02	0.7	7	100	10^4	10^{23}

Apart from the above-mentioned control parameters, there are three response parameters, that characterize the dynamical behaviour of the system: (i) the Nusselt number (Nu), which is the ratio of the convective heat flux to the conductive heat flux, (ii) the Reynolds number (Re), which is the ratio of the momentum advection term to the momentum diffusion term, and (iii) Peclet number (Pe), which is the ratio of the temperature advection term to the heat diffusion term. In the following, we discuss various forms of dynamical equations used to study RBC.

When we take the limit $P \rightarrow 0$ in Eq. (1.14), we obtain the equation for zero-Prandtl (zero-P) number convection [5]:

$$\frac{\partial \mathbf{u}}{\partial t} + (\mathbf{u} \cdot \nabla) \mathbf{u} = -\nabla \sigma + R\theta + \nabla^2 \mathbf{u}, \quad (1.16)$$

$$u_3 + \nabla^2 \theta = 0, \quad (1.17)$$

$$\nabla \cdot \mathbf{u} = 0. \quad (1.18)$$

We use these equations for simulating zero-P convection.

For large-Prandtl (large-P) number convection, the time scale d^2/ν is too small. Hence, d^2/κ is used as the time scale for large-P convection. Consequently, the non-dimensional equations become

$$\frac{\partial \mathbf{u}}{\partial t} + (\mathbf{u} \cdot \nabla) \mathbf{u} = -\nabla \sigma + RP\theta \hat{z} + P\nabla^2 \mathbf{u}, \quad (1.19)$$

$$\frac{\partial \theta}{\partial t} + \mathbf{u} \cdot \nabla \theta = u_3 + \nabla^2 \theta, \quad (1.20)$$

$$\nabla \cdot \mathbf{u} = 0. \quad (1.21)$$

The dynamical equations (Eqs. (1.13)-(1.15)) have been written using the three components of the velocity field and the temperature field. These equations can also be written using the vertical velocity (u_3) and the vertical vorticity (ω_3), where $\omega_3 = \hat{z} \cdot (\nabla \times \mathbf{u})$. Now, the governing dynamical equations under the same scalings as used for Eqs. (1.13)-(1.15) would be

$$\begin{aligned} \partial_t(\nabla^2 u_3) &= \nabla^4 u_3 + R\nabla_H^2 \theta \\ &\quad - \hat{z} \cdot \nabla \times [(\boldsymbol{\omega} \cdot \nabla) \mathbf{u} - (\mathbf{u} \cdot \nabla) \boldsymbol{\omega}], \end{aligned} \quad (1.22)$$

$$\partial_t \omega_3 = \nabla^2 \omega_3 + [(\boldsymbol{\omega} \cdot \nabla) u_3 - (\mathbf{u} \cdot \nabla) \omega_3], \quad (1.23)$$

$$P(\partial_t \theta + (\mathbf{u} \cdot \nabla) \theta) = u_3 + \nabla^2 \theta, \quad (1.24)$$

$$\nabla \cdot \mathbf{u} = 0, \quad (1.25)$$

where $\boldsymbol{\omega} = \nabla \times \mathbf{u}$, \hat{z} is the vertically-directed unit vector, and $\nabla_H^2 = \partial_{xx} + \partial_{yy}$ is the horizontal Laplacian operator. For zero-Prandtl number convection, the above equations reduce to

$$\begin{aligned} \partial_t(\nabla^2 u_3) &= \nabla^4 u_3 + R\nabla_H^2 \theta \\ &\quad - \hat{z} \cdot \nabla \times [(\boldsymbol{\omega} \cdot \nabla) \mathbf{u} - (\mathbf{u} \cdot \nabla) \boldsymbol{\omega}], \end{aligned} \quad (1.26)$$

$$\partial_t \omega_3 = \nabla^2 \omega_3 + [(\boldsymbol{\omega} \cdot \nabla) u_3 - (\mathbf{u} \cdot \nabla) \omega_3], \quad (1.27)$$

$$\nabla^2 \theta = -u_3, \quad (1.28)$$

$$\nabla \cdot \mathbf{u} = 0. \quad (1.29)$$

In the next section we discuss various instabilities and patterns exhibited in RBC.

1.2 RB Convection near the onset

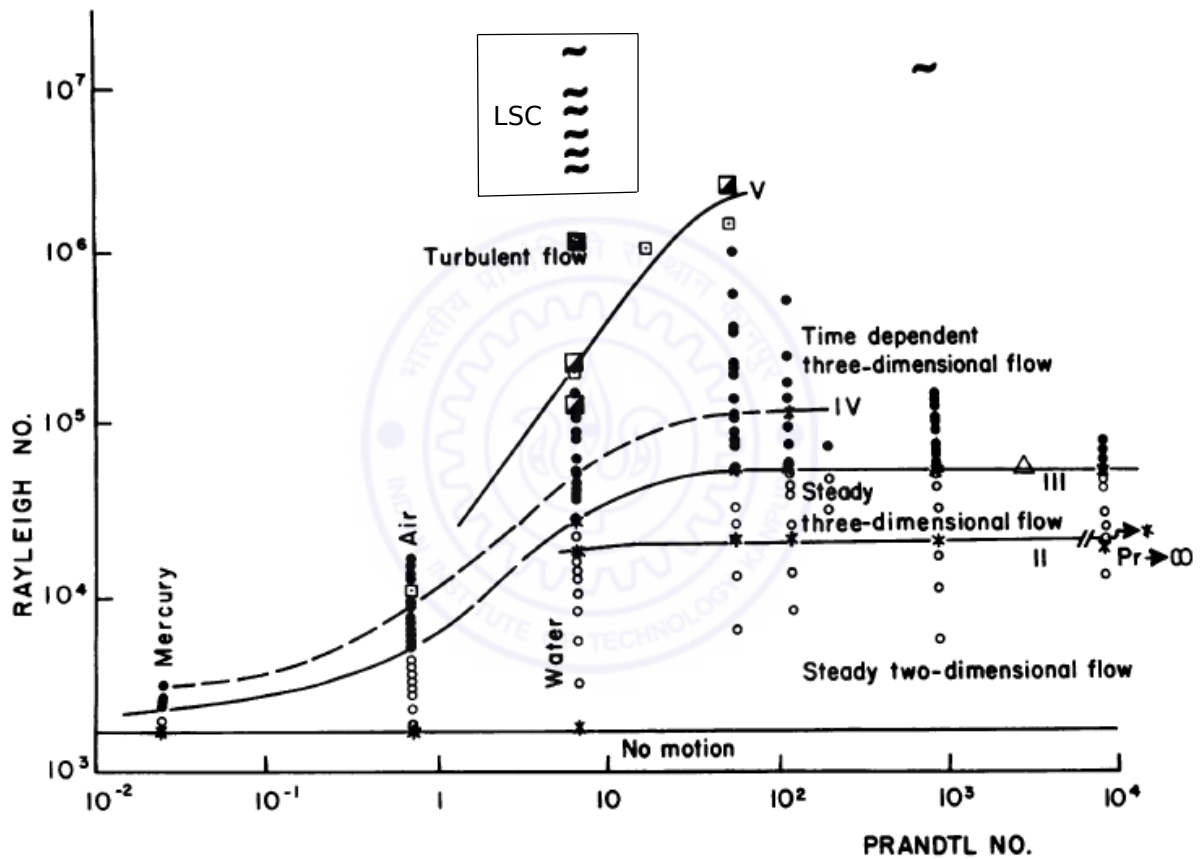


Figure 1.1: Plot showing transitions in convection as a function of the Rayleigh and Prandtl numbers [adapted from Krishnamurti and Howard, PNAS (1981) [6]]. The curve indicates the onset of steady rolls (I), three-dimension steady convection patterns (II), time dependent convection (III), and turbulent flow (IV). Symbols denote the dynamical structure of the flows in different regime: \circ , steady roll; \bullet , time-dependent cellular flow; and \sim , large-scale flow.

Convection starts as the Rayleigh number is increased beyond a critical value. This is called the critical Rayleigh number (R_c). The critical Rayleigh number is independent of the Prandtl number, but still it depends on the boundary conditions. For the box

geometry, the numerical value of R_c is 657.5 for the free-slip boundary condition and 1707 for the no-slip boundary condition. Flow appears as a two-dimensional roll at the onset of convection. Note that the orientation of the roll depends on the initial perturbation. As the Rayleigh number is increased beyond the transition state, the RBC system exhibits transitions from the static states to the turbulent states via periodic and chaotic states as intermediate states. Systematic transitions between the convective states are shown in Fig. 1.1 [6] for different fluids.

As shown in Fig. 1.1, the transition from conduction to convection states occurs at $R_I \simeq 1707$. Note that the transition occurs at the same R_I for all Prandtl numbers. The flow is two-dimensional near the onset. For moderate Prandtl number ($P \sim 1$) and high Prandtl number ($P > 1$) fluids, steady two-dimensional rolls are realized upto $R \sim 2 \times 10^4$. Beyond $R = R_{II} = 2 \times 10^4$ (shown as curve II in Fig. 1.1) the steady two-dimensional rolls make a transition to steady three-dimensional convection patterns. Note that the structure of the three-dimensional patterns depends on the symmetry and aspect ratio of the container. For example, square pattern, asymmetric square pattern, etc., are observed for a rectangular box, while hexagonal pattern and spiral pattern are observed for a cylindrical container. The steady three dimensional flow continues till $R = R_{III}$, marked as curve III in Fig. 1.1, beyond which the flow becomes periodic in time due to various kinds of time-dependent instabilities. The nature of the time-dependent instabilities depends on the initial perturbations and control parameters (R, P, τ). Some of these time-dependent instabilities are zigzag, skewed-varicose, wavy roll, Eckhause etc. [7, 8, 9, 10, 11].

At $R = R_{IV}$ (curve IV in Fig. 1.1), the flow loses its temporal coherence and the flow becomes chaotic. Further increase of the Rayleigh number results in a loss of the spatial and the temporal coherence of the flow. In this state, flow exhibits the spatio-temporal chaos. Flow becomes turbulent at $R = R_V$ (curve V in Fig. 1.1). In turbulent state, flow exhibits random characteristics in both space and time. It is interesting to note that the statistical coherence of the flow is restored above a certain threshold value of the Rayleigh number with an appearance of “large scale circulation” (shown as \sim in Fig. 1.1). In this state on average flow rises from one side of the lateral wall and comes

down on the opposite side wall. The length and time scales of this large scale circulation are the container size and the eddy turn-over time of the flow, respectively. Later in this chapter, we will discuss random reorientations and reversals exhibited by the “large scale circulation” (LSC).

The transition to convective state for low- P convection is different from that for high- P convection. For low- P ($P \ll 1$), secondary instabilities appear as time-dependent, contrary to the high- P convection case for which secondary instabilities appear as a steady three-dimensional convection. Questions arise as to how the secondary instabilities are generated for low- P convection. Furthermore, the regime for the stable two-dimensional roll pattern shrinks rapidly as P is decreased. An important topic of investigation has been the nature of flow structures just near the onset for low-Prandtl number and zero-Prandtl number convection [12]. In the following subsection, we review the analytical, experimental, and numerical works that investigate the nature of patterns and their dynamics near the onset of convection for both low- P and zero- P convection.

1.2.1 Patterns and chaos for low-Prandtl number convection

For small Prandtl number convection, secondary instabilities occur near the onset of convection. The secondary instabilities and the resulting patterns depend critically on the Prandtl number. For low- P , the inertial term $\mathbf{u} \cdot \nabla \mathbf{u}$ becomes quite important and it generates vertical vorticity. Consequently, the flow patterns are three-dimensional, and oscillatory waves along the horizontal axes are generated near the onset of convection. On the contrary, for large-Prandtl number (large- P) convection, vertical vorticity is absent near the onset and the two-dimensional (2D) rolls survive till large Rayleigh numbers [7].

Instabilities and chaos in low- P convection have been widely studied using analytical tools (e.g., approximation techniques), experiments, and numerical simulations. Busse [13] established a close connection between vertical vorticity and time-dependent behaviour of RBC. He demonstrated that in the limit of small Prandtl numbers, the ‘oscillatory’ instability for stress-free boundaries sets in due to the generation of the vertical component of the vertical vorticity. Using perturbative analysis, he showed that for small Prandtl numbers, the 2D rolls become unstable when the amplitude of the convective motion

exceeds a critical value. According to him, the condition for the instability takes the form

$$\frac{R_t}{R_c} - 1 \approx 0.310P^2 \quad (1.30)$$

where R_c is the critical Rayleigh number for the onset of convection, and R_t is the Rayleigh number when time-dependent instability first sets in in the system.

In a review article, Libchaber and Maurer [14] point out that the vorticity is horizontal before the onset of the oscillatory instability, and the vertical component of the vorticity is generated with the introduction of time-dependent instabilities. Busse and Bolton [15] argued that under free-slip boundary conditions, the stability of the 2D rolls exists only for Prandtl numbers above a critical value P_c , which is around 0.543. Ozoe and Hara [16] performed numerical simulations for the Prandtl numbers $P = 0.001-0.1$ fluid in a two-dimensional rectangular enclosure of aspect ratio 4 and observed that the time-dependent behaviour sets in at the onset of convection for $P = 0.01$, thus decreasing the value of P_c to a much lower limit than that predicted by Busse and Bolton [15]. Clever and Busse [17] extended the oscillatory instability analysis to no-slip boundary conditions and showed that the convective rolls are unstable for Prandtl numbers less than about 5.

The role of the non-linear terms in the generation of various kinds of instabilities and patterns for low- P convection have been extensively studied using different analytical techniques. One way for the analytical investigation is to write the equations of the amplitudes of slowly varying large scale modes [18]. Newell and Whitehead [19] and Segel [20] derived the amplitude equations for wave packets of 2D rolls. Using these equations, they investigated the nature of secondary instabilities for containers with small and large aspect ratios. Subsequently, Siggia and Zippelius [21, 22, 23] included the marginal modes associated with a slowly varying vertical vorticity in the amplitude equations and predicted that for low-Prandtl numbers, 2D rolls are always unstable in an infinite layer. Later on, Busse and Bolton [15] included the modes pertaining to the free-slip boundary conditions in their analytical studies which were validated by their subsequent numerical works [24]. Fauve *et al.* [25] investigated the origin of instabilities in low- P convection using the phase dynamical equations and argued that the instability always saturates

into travelling waves as observed in experiments and numerical simulations. Jenkins and Proctor [26] studied the transition from 2D rolls to square patterns in RBC for different Prandtl numbers using analytical tools.

Interesting experiments have been performed to explore the instabilities and chaos in convective flows near the onset. Willis and Deardorff [27] carried out experiments on air ($P = 0.7$) and observed time-dependence as a result of wavy instability. Rossby [28] demonstrated the existence of wavy instability in mercury ($P = 0.02$). Krishnamurti [29] performed extensive convection experiments on a variety of fluids ($P = 0.1-50$) and observed stationary and time-dependent three-dimensional patterns in her experiments; time-dependent rolls appear at much lower Rayleigh numbers for low- P convection compared to that for large- P convection.

One of the convection experiments performed for low- P in the laboratory is on liquid sodium ($P \sim 0.01$). The visualization of flow patterns inside these types of low- P fluids (also mercury) is quite difficult. Due to these limitations of experiments, numerical simulations have played a very significant role in the study of low- P convection. Furthermore, numerical simulations complement experiments in the investigation of instabilities and chaos in convection. Lipps [30] simulated convective flows in air ($P \approx 0.7$) and investigated various states including 2D rolls, time-periodic and aperiodic convection as functions of the Rayleigh number and the aspect ratio. He showed that the roll solution becomes unstable due to the oscillatory instabilities consequently leading to chaotic states. Bolton and Busse [24] studied the stability of the steady convection rolls with respect to arbitrary three-dimensional infinitesimal disturbances and observed stability of steady solutions for a small regime of Rayleigh numbers and wavenumbers. Clever and Busse [31] simulated convective flows for $P = 0.02$ with rigid boundary conditions using Galerkin technique and observed the instabilities of the roll to be due to the travelling waves along the axis of the roll. They found that these travelling waves encounter a secondary bifurcation which saturate in a quasi-periodic regime. Meneguzzi *et al.* [32] performed three-dimensional convective simulations for $P = 0.2$ under stress-free boundary conditions, and for $P = 0.025$ under no-slip boundary conditions. For $P = 0.2$, they observed stationary, periodic, bi-periodic, and chaotic regimes as the Rayleigh number is increased.

For the latter, they found stationary and time-periodic solutions only. Thual [12] studied low- P convection using numerical simulations for both no-slip and free-slip boundary conditions. In his simulations, he observed supercritical oscillatory instabilities, competition between the two-dimensional rolls, square and hexagonal patterns, travelling and standing waves, and chaos for low- P convection.

The study of the origins of the large number of patterns and instabilities observed in numerical simulations and experiments can be quite intricate. Each run of the simulation takes a long time, so it is not possible to scan the entire parameter space minutely for the purpose of deciphering a detailed bifurcation scenario. Moreover, experiments have their own limitations. The large number of modes present in simulations and experiments tend to obscure the underlying dynamics. These difficulties can be circumvented by a powerful and complimentary approach in which the system is analyzed using an appropriately constructed low-dimensional model employing Galerkin-projection techniques. Lorenz [33] was one of the first scientists to propose a three-mode low-dimensional model to investigate the chaos and patterns observed in Rayleigh-Bénard convection using the Galerkin projection techniques. Subsequently, McLaughlin and Martin [34], and Curry *et al.* [35] proposed a generalized Lorenz model in higher dimensional state space. They observed various convective states including chaos through the period-doubling route and quasi-periodic routes. Yahata [36, 37] constructed the 48-mode model to explain the experimental results of RBC near the onset and reported a chaos through quasi-periodic (Rouelle-Takens type) and period-doubling routes.

Mishra *et al.* [38] proposed a 30-mode low-dimensional model for low- P convection using the energetic modes of a direct numerical simulation performed on 64^3 grids in a 3D box with free-slip boundary conditions, and perform a bifurcation analysis using this model and simulation results. Our model and the simulation results exhibit chaotic behaviour near the onset for low- P ($P \sim 0.005$). Furthermore, the bifurcation analysis for the low-dimensional model provides an explanation for the origin of squares, asymmetric squares, oscillating asymmetric squares, relaxation oscillations with an intermediate square regime, and three kinds of the chaotic attractors. These results will be described in Chapter 3 of this thesis.

1.2.2 Patterns and chaos for zero-Prandtl number convection

The numerical works of Thual [12] indicate that the properties of low- P convection as $P \rightarrow 0$ are quite close to those of zero- P convection. Hence, low- P convection as $P \rightarrow 0$ appears to approach zero- P convection as a limiting case. Therefore, zero- P convection is very useful for understanding the properties of low- P convection. Even though numerical analysis of zero- P convection is quite tricky due to its inherent instabilities near the onset, it provides certain advantages. For $P = 0$, the thermal modes are enslaved to the velocity modes [see Eq. (1.17)], hence the number of independent variables is less than those required for low- P analysis. Also, the time steps for numerical simulations of low- P could be very small due to the stiffness of the equations, which is not a limitation for zero- P convection [12]. Further, the growing two-dimensional roll solution becomes the exact solution of the nonlinear equations near the onset for zero- P convection. This feature makes the study of zero- P convection theoretically very interesting [39]. In the following we present a brief review of the numerical and theoretical studies performed for $P = 0$ convection.

Herring [40] was the first to simulate zero- P convection under the free-slip boundary conditions. However, he observed a divergence of the solutions possibly due to an inadequate selection of the initial modes. Clever and Busse [31] performed simulations with no-slip boundary condition for low-Prandtl and zero-Prandtl number convection. They compared the first instabilities of zero-Prandtl number convection to those of low-Prandtl number convection and found that the limit of vanishing Prandtl number approaches zero- P smoothly in the range of Rayleigh numbers that includes at least two subsequent bifurcations beyond the onset of convection. Subsequently, Thual [12] performed the simulation of zero- P convection with free-slip and no-slip boundary conditions. The patterns observed by Thual are two-dimensional rolls, periodic and quasi-periodic rolls, squares, travelling waves, etc. Many of the patterns and instabilities observed for zero- P resemble those observed for the low- P simulation [32].

Many low-dimensional models have been proposed to study the patterns and instabilities near the onset for low-Prandtl number and zero-Prandtl number convection. Using

a 6-mode model of zero-P convection, Kumar, Fauve and Thual [39] showed that the growth of the 2D rolls saturate through the generation of the vertical vorticity (wavy nature). Kumar, Pal and Fauve [41] observed critical bursting in the above model during the saturation. Pal and Kumar [42] explained the mechanism of the selection of the square patterns using a 15-mode model of zero-P convection.

Pal *et al.* [43] constructed a bifurcation diagram for zero-P convection using a low-dimensional model and direct numerical simulation. The bifurcation analysis for the low-P convection has significant similarities with that for zero-P convection, except near the onset of convection. These issues will be discussed in Chapter 3.

As the Rayleigh number is increased, various non-linear instabilities generate chaos, spatio-temporal chaos, soft-turbulence, and hard turbulence. In the turbulent state, RBC exhibits many interesting dynamics at both small and large scales. In the next section, we will discuss two aspects of turbulent RBC: (i) the energy spectra and fluxes at small scales, and (ii) dynamics of large scale flow.

1.3 Turbulent RBC

In our thesis, we focus on two features of turbulent RBC: (a) nature of the energy cascade in convective turbulence in the presence of buoyancy force, and (b) properties of large scale structures appearing in hard turbulence. Scientists have observed in experiments that these structures tend to reverse over time. We will, thus, study the dynamics of reversal.

1.3.1 Scalings of energy spectra in the inertial range of turbulent RBC

One interesting problem in turbulent convection is the scaling of the energy spectra and fluxes in the inertial range of turbulent RBC. In 1941, Kolmogorov [44] proposed a phenomenological theory for the energy transfer from large scales to small scales in the inertial range of fluid turbulence. According to this theory, the energy cascade is independent of

the fluid properties and nature of the energy input at the large scales, and the energy spectrum of the velocity field can be expressed in terms of this energy cascade and the local wave number. The energy spectrum of the velocity field falls with an exponent of $-5/3$, and corresponding flux remains constant in the inertial range.

The energy spectra and fluxes for the convective turbulence are more complex than those for fluid turbulence due to the presence of the buoyancy force [45, 46]. For stable-stratified fluid convection, Bolgiano [47] and Obukhov [48] proposed a dual cascade picture in the inertial range. For small wavenumbers (large length scale), they predicted a dominance of the buoyancy force over the inertial term leading to the velocity and temperature spectra scaling as $k^{-11/5}$ and $k^{-7/5}$, respectively, where k is the wavenumber. In this regime, the energy flux of the temperature field is constant, while the flux of the velocity field varies as $k^{-4/5}$. For the intermediate wavenumbers, Bolgiano [47] and Obukhov [48] conjectured the dominance of the inertial force over the buoyancy force. Consequently, the temperature field evolves as a passive scalar, and both the velocity and temperature fields have Kolmogorov's energy spectrum ($k^{-5/3}$) and constant energy fluxes [44, 47, 48]. The length scale that separates these two different regimes of the energy cascades is called the Bolgiano length (l_B).

Later, Procaccia and Zeitak [49], L'vov [50], and Falkovich and L'vov [51] proposed the same scaling for Rayleigh-Bénard convection. In convective turbulence, for scales above the Bolgiano length ($l > l_B$), the kinetic energy spectrum ($E^u(k)$) and the entropy spectrum ($E^\theta(k)$) follow the Bolgiano-Obukhov (BO) scaling

$$E^u(k) = C_k(\epsilon^\theta)^{\frac{2}{5}}(\alpha g)^{\frac{4}{5}}k^{-\frac{11}{5}}, \quad (1.31)$$

$$E^\theta(k) = C_\theta(\epsilon^\theta)^{\frac{4}{5}}(\alpha g)^{-\frac{2}{5}}k^{-\frac{7}{5}}, \quad (1.32)$$

$$\Pi^u(k) = C_f(\epsilon^\theta)^{\frac{3}{5}}(\alpha g)^{\frac{6}{5}}k^{-\frac{4}{5}}, \quad (1.33)$$

while for $l < l_B$, the spectra follow the Kolmogorov-Obukhov (KO) scaling

$$E^u(k) = K_{Ko}(\epsilon^u)^{\frac{2}{3}}k^{-\frac{5}{3}}, \quad (1.34)$$

$$E^\theta(k) = K_\theta\epsilon^\theta(\epsilon^u)^{-\frac{1}{3}}k^{-\frac{5}{3}}, \quad (1.35)$$

where Π^u is the kinetic energy flux, ϵ^u and ϵ^θ are the kinetic and entropy dissipation rates, respectively, α is the thermal expansion coefficient of the fluid, and g is the acceleration due to gravity. K_{Ko} is Kolmogorov's constant. C_k, C_θ, C_f , and K_θ are other universal constants. Note that in literature, the spectrum and the flux of the temperature field are also referred to as the “entropy spectrum” and the “entropy flux”, respectively. The entropy flux is defined in the similar spirit as the energy flux, and it is $\theta^2/2$ (entropy) leaving per unit time from a wavenumber sphere of radius k_0 . Note that the entropy flux is not same as heat flux, which is defined as $\langle u_3\theta - \kappa\partial_z\theta \rangle_A$, where $\langle \rangle_A$ denotes the average over the horizontal plane.

The Bolgiano length l_B has the following dependence on the convective parameters:

$$l_B = \frac{Nu^{\frac{1}{2}}d}{(RP)^{\frac{1}{4}}}, \quad (1.36)$$

where Nu is the Nusselt number (dimensionless heat flux), R is the Rayleigh number, P is the Prandtl number, and d is the vertical height of the container. Grossmann and L'vov [52] and Chillá *et al.* [53] argued that for $P < 1$, the Bolgiano length is of the order of container's size. Hence, only KO scaling is expected in the inertial regime for low Prandtl number convection. For large-Prandtl number convection, l_B lies in the inertial regime and hence mixed scaling is expected. Several exact relationships connecting ϵ^u , ϵ^θ , Nu , R , and P have been derived for homogeneous convective turbulence. Shraiman and Siggia [54] have derived that

$$\epsilon^u = \frac{\nu^3}{d^4}(Nu - 1)RP^{-2}, \quad (1.37)$$

$$\epsilon^\theta = \kappa \frac{(\Delta T)^2}{d^2} Nu. \quad (1.38)$$

Researchers have attempted to test the above scaling predictions [Eqs. (1.31)-(1.35)] by using experiments and numerical simulations (to be described later in this section). In a recent review, Lohse and Xia [46] have described these results critically and exhaustively. The inconsistencies of the scaling predictions with the numerical and experimental results are attributed to the drastic assumptions, such as isotropic and homogeneous nature of

the flow, made in the scaling arguments. In the theory described above, both thermal and viscous boundary layers are not considered appropriately. Shraiman and Siggia [54] and Grossmann and Lohse [55] showed that the properties of the fluctuations in the boundary layer and in the bulk are rather different. Experiments and numerical simulations reveal that the fields in the boundary layer are highly inhomogeneous and anisotropic, while the bulk flow is somewhat homogeneous and isotropic. Hence, the above scaling arguments are expected to hold only in the bulk, if at all. The computation of the Bolgiano length l_B [Eq. (1.36)] assumes uniform dissipation, which is not valid in the boundary layer. Calzavarini *et al.* [56] have computed l_B for different layers in the convective fluid; they report that l_B/d is small near the walls (in the boundary layer), but $l_B/d \approx 1$ in the bulk. In brief, the presence of boundary layers, taking a single l_B for the whole fluid, the inhomogeneity and anisotropy of the flow are some of the features that possibly make the above scaling arguments inconsistent with realistic experiments and simulations [46].

To disentangle various complexities mentioned above, researchers have idealized the geometry of RBC even further. For example Borue and Orszag [57], Škandera *et al.* [58] considered convection in a periodic box (with thermal gradients along the vertical) and obtained KO scaling. This feature removes the effects of the viscous and thermal boundary layers on the bulk, and hints that BO scaling is possibly due to the thermal forcing in the boundary layer [46]. For the free-slip and conducting boundary conditions, the viscous boundary layer is insignificant, while the thermal boundary layer is present. These conditions suppress the effect of the boundary layers and provide the energy spectrum for the bulk. These boundary conditions are widely used in the investigation of instabilities and behaviour of spectra in the turbulent regime for the RBC problem.

In the following discussion, we briefly review the experimental studies that attempt to test the above phenomenology of RBC. Many convection experiments measured the velocity and temperature fields only at fixed locations of the apparatus. For such experiments, the “local Taylor hypothesis” is invoked to relate the frequency spectrum to the wavenumber spectrum [46, 59]. However, in some experiments, high resolution spatial velocity and temperature fields have been measured for computing the above-mentioned spectra; experiments by Mashiko *et al.* [60] and Sun *et al.* [61] belong to this category of

experiments. Chillá *et al.* [53], Zhou and Xia [62], and Shang and Xia [63] carried out convection experiments on water ($P \approx 7$) at large Rayleigh number and found the energy spectrum to be consistent with BO scaling. Heslot *et al.* [64] and Castaing [65] measured frequency power spectrum of the temperature field in gaseous Helium ($0.65 < P < 1.5$) and found the spectrum to be consistent with KO scaling. Wu *et al.* [66] however reported BO scaling for Helium gas through frequency spectrum measurements of temperature. Ashkenazi and Steinberg [67] performed an experiment with sulfur hexafluoride (SF_6) gas contained in a rectangular box of aspect ratio 0.7. They carried out their experiment near the critical point of SF_6 , where they were able to vary the Rayleigh and Prandtl number over a wide range, R from 10^9 to 10^{14} and P from 1 to 300. Using the light scattering produced by the critical density fluctuation, Ashkenazi and Steinberg [67] measured the local velocity by using laser Doppler velocimetry technique and measured the frequency power spectra for over a wide range of R and P . Their measured frequency power spectra of the vertical velocity showed an exponent of -2.4 , which is close to the BO exponent of $-11/5$ predicted for the wave number spectra. They also measured the temperature spectra using the thermistors by placing the probes near the boundary layers and observed the scaling exponent of -1.45 which is close to BO scaling. Mashiko *et al.* [60] performed convection experiments for mercury and reported BO scaling for the velocity spectra. Niemela *et al.* [68] measured temperature time series for He gas ($P \approx 0.7$) and reported the presence of both the KO and BO scaling. Cioni *et al.* [69] carried out experiments on mercury ($P \simeq 0.02$, a low- P fluid), and reported KO frequency spectrum for it. Thus the outcome of these experiments are somewhat inconclusive on the validity of the phenomenologies for RBC, yet the majority appear to support BO scaling for large- P ($P \geq 0.7$) convection, and the KO scaling for low- P ($P < 0.7$) convection.

Numerical experiments provide important clues in the study of turbulence. The tremendous advantage that numerical simulations have over turbulent experiments is that in numerical simulations data can be measured at multiple points. However, due to the high computational cost, only a limited range of R can be covered in simulations. A series of numerical simulations of RBC have been performed to test the KO and BO scaling. Grossmann and Lohse [70, 71] simulated an RB fluid with $P = 1$ under

Fourier-Weierstrass approximation and reported KO scaling. Borue and Orszag [57] and Škandera *et al.* [58] performed pseudo-spectral simulations on $P = 1$ fluid with periodic boundary conditions in all directions and found consistency with KO scaling. Vincent and Yuen [72] performed spectral simulations for $P = 1$ and $R = 10^8$ using free-slip boundary conditions and reported spectral indices of $-5/3$ and -3 for the temperature and velocity fields, respectively. They, however, found dual branches in the entropy spectrum. Paul *et al.* [73] also observed dual entropy spectrum in their 2D spectral simulations with free-slip boundary conditions, albeit at lower Rayleigh numbers. Rincon [74] performed a numerical simulation using a higher order finite-difference scheme to study the effects of inhomogeneity and anisotropy on the scaling of the energy spectra; for $R = 10^6$ and $P = 1$ on $256 \times 256 \times 128$ grids with free-slip boundary conditions, he reported that the numerical results are inconclusive in identifying a definite spectral slope. Kerr [75] used pseudo-spectral method for his simulations of $P = 0.7$ fluid (air) under no-slip boundary conditions on top and bottom plates and periodic condition on the side walls; he observed $E^u(k) \approx k^{-5/3}$ for the velocity spectrum and a less steep scaling for the temperature spectrum, consistent with $E^\theta(k) \approx k^{-1}$. Camussi and Verzicco [76] performed numerical simulations for a fluid with $P = 0.7$ contained in a cylindrical geometry using the finite-difference method; they found both velocity and temperature spectral exponents to be $-7/5$, which is inconsistent with both the KO and BO scaling. They attribute this anomaly to inhomogeneities and the anisotropy of the flow near the boundaries. On the whole, numerical results indicate uncertainty in the tests of the convective phenomenology.

Another way to investigate turbulent scaling is through the structure function calculations. Following Kolmogorov, Yakhot [77] derived an exact analytical form for the third-order structure function for BO scaling. Skrbek *et al.* [78] calculated the temperature structure functions using the experimental data of helium ($P \approx 0.7$) for $R = 1.5 \times 10^{11}$ and reported BO scaling. Note that they used extended self similarity in their analysis. Sun *et al.* [61] computed the structure functions of the velocity and temperature fields using the data of their convection experiments on water and reported KO scaling. Kunnen *et al.* [79] performed similar calculations for Helium gas (both experiments and numerical simulation) and observed BO scaling. Calzavarini *et al.* [56] computed third-order struc-

ture function using the Lattice Boltzmann method for $P = 1$ and reported BO scaling. Hence, structure function studies, too, are inconclusive in testing of the validity of BO and KO scaling.

The above results indicate ambiguity in the phenomenologies of convective turbulence. To complement the earlier phenomenological and experimental observations on the scalings of spectra in the inertial range, we computed the energy spectra and cascade rates for the velocity and temperature fields using the pseudo-spectral method on 512^3 grids over a wide range of Prandtl numbers. We considered the free-slip boundary condition on the top and bottom plates to reduce the effects of viscous boundary layers on the cascade of energy. Our computations include zero-Prandtl number, low-P, and large-P convection regimes ($P = 0, 0.02, 0.2, 1, 6.8$). We hence have a reasonable number of numerical runs to confirm the existing phenomenology in turbulent convection. The detailed results pertaining to these investigations are presented in Chapter 4 of this thesis.

1.3.2 Large scale circulation and its associated dynamics in turbulent RBC

In the previous subsection, we discussed the energy spectra and fluxes of convective turbulence. Another interesting feature of convective turbulence observed in RBC experiments is the presence of coherent roll structures at large length scales in spite of strong random fluctuations at small scales. This is called the “large scale circulation” (LSC) of “mean wind” [6, 80, 81, 82, 83, 84, 85, 86, 87]. The regime for LSC is shown as \sim in Fig. 1.1 [6]. It is a coherent structure of the flow in which the fluid particle ascends from one side of the wall and descends from the opposite side. It has been observed in laboratory experiments that the vertical plane containing LSC undergoes a diffusive motion in the azimuthal direction of the cylindrical container. Sometimes, in the course of its motion, the plane of the LSC changes by a significant angle. This phenomenon, called the “reorientation of the LSC”, has been found to occur in two ways: (i) rotation-led in which reorientation takes place without changing the amplitude of the LSC, and (ii) cessation-led in which the amplitude of the LSC vanishes during the reorientation [84, 85]. The reorientation

of the LSC typically leads to flow reversals. These issues are of major interest to the community at present. For a recent review, see [87]. In the following, we will review the experimental, theoretical, and numerical works related to the LSC in the Rayleigh-Bénard convection.

Krishnamurti and Howard [6] performed experiments on water ($P \simeq 7.0$) and silicon oil ($P \sim 860$) and observed coherent roll structures or LSC in the turbulent regime. Subsequently, Castaing *et al.* [80] ascertained the existence of LSC in helium ($P \simeq 0.65 - 1.5$) contained in a cylindrical container. They proposed that coherent large-scale structures exist statistically only above a certain Rayleigh number ($R \simeq 10^8$). They also observed a low frequency peak in the power spectrum of the temperature field. Xi *et al.* [88] studied the onset of large-scale coherent mean flow in RBC using shadowgraph and particle image velocimetry techniques and showed that LSC is a result of the organization of plume motion.

Cioni *et al.* [81] performed RBC experiments on mercury ($0.021 < P < 0.026$) and placed several thermistors along the azimuthal direction of the cylinder. They deduced the presence of global circulation from the dipolar temperature distribution measured by the probes. The temperature fluctuations (after subtracting the mean) switched signs randomly in their experiment. Since the warmer fluid ascends from one side, and the cooler fluid descends from the other side of the apparatus, Cioni *et al.* [81] deduced that the vertical velocity would also exhibit random “reversals” in phase with the temperature fluctuations. This feature of convection has been studied extensively using theoretical, experimental, and computational tools [87, 89].

To capture the dynamics of LSC in the azimuthal direction, Cioni *et al.* [81] put eight probes in the azimuthal direction of the cylindrical container and computed the first Fourier mode of the measured temperature field using the following relations:

$$\hat{T}_1(t) = \sum_{j=1}^8 T_j(t) \exp(-i\delta_1), \quad (1.39)$$

$$|\hat{T}_1(t)| = \sqrt{\Re(\hat{T}_1)^2 + \Im(\hat{T}_1)^2}, \quad (1.40)$$

$$\delta_1 = \arctan \frac{\Im(\hat{T}_1)}{\Re(\hat{T}_1)}, \quad (1.41)$$

where $T_j(t)$ is the temperature field measured at the j^{th} probe at a particular instant of time, \hat{T}_1 is the first azimuthal Fourier mode, $|T_1(\hat{t})|$ and δ_1 are the amplitude and phase of the first azimuthal Fourier mode, respectively, and $\Re(\hat{T}_1)$ and $\Im(\hat{T}_1)$ represent the real and imaginary parts of the first Fourier mode, respectively. They observed that the amplitude of the first Fourier mode never vanishes, while the phase of first Fourier mode changes by an angle of π during the reversal of the flow. They related this reversal of LSC due to the travelling wave instability in the azimuthal direction of the cylindrical container. Note that they did not report the dynamics of the higher Fourier modes during the reversals of LSC. Cioni *et al.* [81] also observed a low-frequency peak in the energy spectrum that corresponds to the circulation frequency of the large-scale flow inside the cylinder.

Tsuji *et al.* [90] performed an experiment with mercury contained in a cylindrical container with aspect ratios 1/2, 1, and 2 and found that the low-frequency peak is absent for the aspect ratio 1/2 case. Niemela *et al.* [82], and Sreenivasan *et al.* [83] performed convection experiments on helium contained in cylindrical container and reported reversals of LSC using two probes near the lateral walls in the bulk of the container.

Brown *et al.* [84] and Brown and Ahlers [85] performed similar experiments on water ($P = 4.38$) and measured the temperature field in the bulk using probes placed at 1/4th, 1/2 and 3/4th of height of the cylinder. They observed that the plane containing the LSC exhibits diffusive and sometimes a quick but significant drift in the azimuthal direction with the angular change ($|\Delta\theta|$) ranging from small values to π , i.e., $\pi/4 < |\Delta\theta| < \pi$. They called this phenomenon as the “reorientation of LSC”, and showed that the reorientation of the flow can occur in two ways: (a) through rotation of the circulation plane without any major reduction of the circulation strength, and (b) through “cessation” of the circulation, followed by a restart in a randomly chosen new direction. Brown and Ahlers [85] observed the probability distribution $P(\Delta\theta)$ to be a power law ($P(\Delta\theta) \propto (\Delta\theta)^\gamma$ with $\gamma = 3.77 \pm 0.04$) for the former, and a uniform distribution for the latter. Brown and Ahlers [85] also computed the amplitude of the first Fourier mode, and found it to be non-zero for the rotation-led reorientations and close to zero during the cessation-led reorientations. Xi *et al.* [86] measured the azimuthal motion of the LSC using particle image velocimetry and studied the reversals of LSC. They also observed cessation-led

and rotation-led reorientation of the LSC for water contained in a cylindrical container of aspect ratio one. They observed that sometimes LSC undergoes two quick cessations within an interval of eddy turn over time, which they termed as a “double cessation”. In a similar set of experiments, Xi and Xia [91, 92, 93] observed strong dependence of the azimuthal reorientations on the aspect ratio of the cylinder.

Qiu and Tong [94] performed RBC experiments on water and computed the temperature correlation functions. They reported a transition from random chaotic states to a correlated turbulent state at around $R_c \simeq 5 \times 10^7$. Sano *et al.* [95] report a strongly correlated large-scale flow beyond $R_c \simeq 4 \times 10^7$ for He gas ($P = 0.7$).

Various theoretical models have been proposed to understand the dynamical behaviour of the LSC. Sreenivasan *et al.* [83] and Benzi [96] proposed a stochastic model in which the reversal of LSC was explained as noise-induced switching between two meta-stable states. They treated diffusion of the LSC strength in a potential well. However, they could not address the azimuthal dynamics of the LSC. Araujo *et al.* [97] attempted to explain the irregular cessation and subsequent reversal of the LSC using the force and thermal balance on a single plume modelled by coupled non-linear equations related to the Lorenz equations. The model was based on assumptions about the lifetimes of the plumes. Brown and Ahlers [98] and Brown and Ahlers [99] proposed a stochastic model with the strength and the azimuthal orientation of the LSC being determined by two stochastic ordinary differential equations; this model appears to explain the experimental observations of cessation and reorientation. They extended the model by considering various perturbations. Villiermaux [100] proposed a model to explain the low-frequency oscillations in the temperature signal measured in the bulk. His model assumes that the modes of the boundary layers interact through the slow-moving large-scale circulation.

There are only a small number of computational studies on the reorientation or reversal of LSC. Stringano and Verzicco [101] simulated convection in air ($P = 0.7$) in a cylinder with an aspect ratio of 1/2 and observed a single roll breaking into two counter-rotating roll stacks vertically. Benzi and Verzicco [102] performed a simulation of a fluid at $R = 6 \times 10^5$ with white noise added to the heat equation and studied the statistical behaviour of the observed reversals. Breuer and Hansen [103] studied RBC for infinite Prandtl

number in a 2D box and observed reversals of the LSC for very high R ($R = 10^9$). There are other 2D numerical experiments in a box that report that the reversals of the LSC are due to cessations [104, 105] or due to the chaotic movement of rolls perpendicular to the roll axis [106].

In Chapter 5, we present a numerical study of the reversals and reorientations of the large scale circulation (LSC) of a convective fluid in a cylindrical container of aspect ratio one. We take the Prandtl number to be 0.7 and Rayleigh numbers in the range of 6×10^5 to 3×10^7 . It is observed that the reversals of the LSC are induced by its reorientation along the azimuthal direction, which are quantified using the phase of the first Fourier mode of the vertical velocity measured near the lateral surface in the mid-plane. During a “complete reversal”, the above phase changes by around 180° leading to reversals of the vertical velocity at all the probes. We also observe “partial reversals” in which the phase of the first Fourier mode changes by an angle of less than 180° . Numerically, we observe rotation-led and cessation-led reorientations, in agreement with earlier experimental results. During the cessation-led orientations, the amplitude of the first Fourier mode becomes relatively weak as compared to the amplitude of the second Fourier mode. This observation is consistent with the quadrupolar dominant temperature profile observed during cessation. We also observe reorientations involving double cessation.

1.4 Outline of the subsequent chapters

The layout of the subsequent chapters is as follows.

In **Chapter 2**, we present the details of the two codes used in our thesis work: (a) a parallel pseudo-spectral code TARANG [107] for a 3D box, and (b) a parallel finite-difference code for a cylindrical container. We use the pseudo-spectral code for two problems: (i) to investigate the dynamics near the instabilities for low- P and zero- P convection, and (ii) to investigate the scalings of the energy cascade in the inertial range for turbulent RBC. The finite-difference code has been used to analyze the reorientations and reversals of large scale circulation in the turbulent regime of convection. In the first part of the chapter, we discuss the details of the techniques and algorithms used in pseudo-

spectral code. This discussion is followed by an introduction of different schemes that have been used for the calculation of various statistical quantities such as fluxes, velocity and temperature spectra, etc., from the numerically calculated fields. In the second part, we provide details of the algorithm used to solve the RBC dynamical equations in a cylindrical geometry with realistic boundary conditions: no-slip at all the walls, adiabatic on the lateral wall, and isothermal on the horizontal plates. At the end of the chapter, we provide some details on (i) the function used for the distribution of the grids, (ii) numerical schemes used to solve the dynamical convective equations in a cylindrical geometry, and (iii) higher-order schemes used to discretize the fields in space.

In **Chapter 3**, we present direct numerical simulations and a related low-dimensional models to investigate the dynamics of patterns near the onset for low-Prandtl number ($P = 0.02$, $P = 0.005$, $P = 0.0002$) for r (reduced Rayleigh number) ranging from 1 - 1.25 in a 3D box on a 64^3 grid with free-slip and conducting conditions on top and bottom plates, and periodic condition on the lateral walls. We observe various convective patterns: rolls, asymmetric squares, squares, oscillatory asymmetric squares, and chaotic patterns for low- P convection. To investigate the origin of these patterns and chaos, we identify the active large scale Fourier modes present near the onset from the DNS data and construct a thirty-dimension model using Galerkin projection methods. We numerically solve the 30 coupled nonlinear equations and construct bifurcation diagrams for various Prandtl numbers. We find that the static patterns such as rolls, squares, and asymmetric squares are generated as a result of supercritical pitchfork bifurcations, and periodic patterns are generated via Hopf bifurcations. Furthermore, we observe presence of chaotic attractors just above the onset for $P \lesssim 0.005$. We present a comprehensive analysis of the route to chaos for these values of P ($P = 0.005$ and $P = 0.0002$) and find that the chaos is related to the “gluing bifurcations”, “attractors merging crisis” and “homoclinic chaos”. We also find that the range of Rayleigh numbers for which stationary 2D rolls exist decreases rapidly with decreasing Prandtl number. Our low- P results are consistent with zero- P convection results [43].

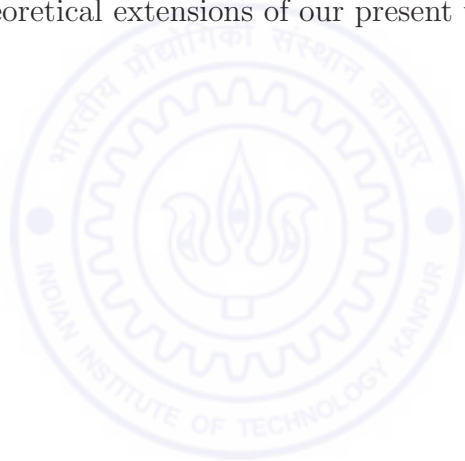
In **Chapter 4**, we compute the spectra and fluxes of the velocity and temperature fields in the inertial range of turbulent RBC using simulations in a 3D rectangular box on

512^3 grids. To reduce the effects of viscous boundary layers on the scalings, we consider free-slip boundary conditions for the velocity and isothermal conditions for the temperature on the horizontal plates. We employ periodic boundary condition for the fields in the horizontal directions. We perform our simulations for the Prandtl numbers 0, 0.02, 0.2, 1, and 6.8. We present a phenomenology for the nature of the energy spectra for zero- P and low- P convection which supports Kolmogorov-Obukhov scaling. Our numerical simulations for $P = 0$ and 0.02 are in good agreement with this phenomenology. For large-Prandtl number convection, the system appears to follow Bolgiano-Obukhov scaling (spectral exponent of $-11/5$ for the velocity field). We also calculate the heat and viscous dissipation rates using our numerical data and find them to be in reasonably good agreement with their corresponding analytical values. We observe that the temperature spectra exhibit dual branches for all finite-Prandtl number simulations. Using the numerical data, we present a phenomenological model to explain this behaviour. Our study suggests that the lower branch of the spectra participate in the non-linear transfer of energy in the inertial range.

In **Chapter 5**, we analyze the dynamics of reorientations and reversals of the large scale circulation in Rayleigh-Bénard convection using direct numerical simulations for air ($P = 0.7$) confined in a cylindrical container of aspect ratio one. We vary R from 6×10^5 to 2×10^7 and employ no-slip boundary conditions. For the temperature, we employ conducting conditions for the top and bottom plates, and adiabatic condition on the lateral surfaces. We calculate velocity and temperature fields at the eight azimuthal probes placed near the side walls in the middle of the container. We first establish the presence of LSC in our simulation. To this end, we calculate autocorrelation function for the temperature fields at these probes and show the presence of regular oscillations in the LSC. This result is consistent with earlier experimental results on LSC. We calculate the phase and amplitudes of the azimuthal Fourier modes. We show that the phase and amplitude of the first Fourier mode provide interesting information on the orientation and strength of the LSC. Next we find that during the “complete reversals”, the phase of the first Fourier mode changes by an angle of 180° leading to the reversals of the vertical velocities at all the probes. We also observe partial reorientations in which the phase of

the first Fourier mode changes by an angle other than 180° . We observe rotation-led and cessation-led partial and full reorientations of the LSC in our numerical simulation. We also report the structure of the flow during rotation-led and cessation-led orientations. We find that the second Fourier mode dominates over the first Fourier mode during the cessation in cessation-led reorientations, while the first Fourier mode continues to dominate throughout in rotation-led reorientations. This observation is consistent with the quadrupolar dominant temperature profile observed during cessation-led reorientation. We also observe double-cessation led reorientation in our simulation, which is a rare event during the azimuthal reorientations of LSC.

In **Chapter 6**, we present a summary and the conclusion of our studies on non-linear instabilities and turbulent aspects of Rayleigh-Bénard convection. We also propose possible numerical and theoretical extensions of our present work.



Chapter 2

Direct numerical simulation of Rayleigh-Bénard convection: numerical details

In this chapter, we present the details of the numerical simulations used for the investigation of the instabilities and the turbulent aspects of Rayleigh-Bénard convection. We have performed studies for two different geometries: (i) a three-dimensional (3D) box with free-slip boundary condition for the velocity field and isothermal boundary conditions for the temperature field on the top and bottom plates, and periodic condition for both the fields in the horizontal directions, and (ii) a cylindrical container with isothermal top and bottom plates and adiabatic lateral walls, and no-slip boundary conditions for the velocity field on all the walls. For the 3D box, we use the pseudo-spectral technique, while for the cylindrical container, we use finite-difference scheme.

We first discuss the algorithm and techniques used to solve the RBC flow in a 3D rectangular box. To this end, time-advancement and the discretization of different terms are discussed. Further, we present the method to compute the fluxes and spectra of the fields from numerically calculated data. In the second part of the chapter, we present the numerical procedure to solve the RBC equations in a cylindrical geometry. To this end, we provide the details of the semi-explicit scheme used for the calculation of the fields. Further, the details of the schemes used for the spatial discretization of the fields are

discussed. At the end, we validate the cylindrical geometry code with earlier numerical and experimental results by calculating the Nu for a range of Rayleigh number varying from $R = 6 \times 10^5$ to 3×10^7 and find the good agreement between our results and earlier ones.

2.1 Pseudo-spectral code for a 3D box

We use a pseudo-spectral code TARANG [107] for simulating RBC in a 3D box. We solve the RBC equations (Eqs. (1.13) - (1.15)) in a 3D rectangular geometry. We employ free-slip boundary conditions for the horizontal velocity fields, isothermal boundary condition for temperature at the top and bottom plates, and periodic boundary conditions for both temperature and velocity fields on the lateral walls. Consequently, the velocity and temperature fields are expanded in terms of the basis functions as

$$u_{1,2}(x, y, z) = \sum_{i_x, i_y} [u_{1,2}(i_x, i_y, 0) + \sum_{i_z} u_{1,2}(i_x, i_y, i_z) 2 \cos(k_z z)] \exp i(k_x x + k_y y), \quad (2.1)$$

$$u_3(x, y, z) = \sum_{i_x, i_y, i_z} u_3(i_x, i_y, i_z) 2 \sin(k_z z) \exp i(k_x x + k_y y), \quad (2.2)$$

$$\theta(x, y, z) = \sum_{i_x, i_y, i_z} \theta(i_x, i_y, i_z) 2 \sin(k_z z) \exp i(k_x x + k_y y), \quad (2.3)$$

where u_1, u_2, u_3 are the x -, y -, and z -components of the velocity field, respectively, and θ is the deviation of the temperature field from the mean profile, and i_x, i_y, i_z are the grid indices with $k_x = i_x \pi / \sqrt{2}$, $k_y = i_y \pi / \sqrt{2}$, and $k_z = n \pi$, n being a positive integer.

2.1.1 Numerical methods

In this subsection, we will briefly sketch the spectral method used for the convective flow in a 3D rectangular container. For details of this numerical scheme we refer to Canuto *et al.* [108]. In Fourier space, Eqs. (1.13)-(1.15) will take the following form

$$\frac{\partial u_i(\mathbf{k}, t)}{\partial t} = -ik_i \sigma(\mathbf{k}, t) - ik_i \sum_{\mathbf{p}+\mathbf{q}=\mathbf{k}} u_j(\mathbf{q}, t) u_i(\mathbf{p}, t) + R\theta(\mathbf{k}, t) \delta_{i3} - k^2 u_i(\mathbf{k}, t), \quad (2.4)$$

$$P \frac{\partial \theta(\mathbf{k}, t)}{\partial t} = u_3(\mathbf{k}, t) - P i k_j \sum_{\mathbf{p}+\mathbf{q}=\mathbf{k}} u_j(\mathbf{q}, t) \theta(\mathbf{p}, t) - k^2 \theta(\mathbf{k}, t), \quad (2.5)$$

$$\mathbf{k} \cdot \mathbf{u}(\mathbf{k}, t) = 0, \quad (2.6)$$

where $u_1(\mathbf{k}), u_2(\mathbf{k}), u_3(\mathbf{k})$ are respectively the x -, y - and z -components of the velocity field (\mathbf{u}) in the Fourier space, and $\theta(\mathbf{k})$ is the deviation of the temperature field from the mean profile in the Fourier space. The box size in the real space is $2\sqrt{2} \times 2\sqrt{2} \times 1$. In the following we describe the steps involved in the calculation of the fields.

1. Computation of the non-linear terms ($\mathbf{u} \cdot \nabla \mathbf{u}$ and $\mathbf{u} \cdot \nabla \theta$) is performed using the Fast Fourier Transforms (FFT). We use the FFTW library in our simulations. The details of this method are as follows:

- (a) Compute $\mathbf{u}(\mathbf{x}), \theta(\mathbf{x})$ from $\mathbf{u}(\mathbf{k}), \theta(\mathbf{k})$ using the Inverse FFTW.
- (b) Compute $u_i(\mathbf{x})u_j(\mathbf{x})$ and $u_i(\mathbf{x})\theta(\mathbf{x})$ in the real space by multiplying the fields at each space point.
- (c) Compute $\text{FFT}[u_i(\mathbf{x})u_j(\mathbf{x})]$ and $\text{FFT}[u_i(\mathbf{x})\theta(\mathbf{x})]$ using FFTW.
- (d) Compute $i k_j \text{FFT}[u_i(\mathbf{x})u_j(\mathbf{x})]$ and $i k_j \text{FFT}[u_j(\mathbf{x})\theta(\mathbf{x})]$ for $j = 1, 2$, and $k_j \text{FFT}[u_i(\mathbf{x})u_j(\mathbf{x})]$ and $k_j \text{FFT}[u_j(\mathbf{x})\theta(\mathbf{x})]$ for $j = 3$. Note that in z -direction *cosine – sine* transformation has been used. The resulting vectors are $\text{FFT}[\mathbf{u} \cdot \nabla \mathbf{u}]$ and $\text{FFT}[\mathbf{u} \cdot \nabla \theta]$.

2. Products $u_i(\mathbf{x})u_j(\mathbf{x})$ produce modes with wavenumbers larger than k_{max} . On FFT, these modes get aliased with $k < k_{max}$ and will provide incorrect value for the convolution. To overcome this difficulty, the last 1/3 modes of the fields $u_i(\mathbf{k})$ are set to zero, and then the FFTs are performed. This scheme is called the 2/3 rule. For details, refer to Canuto *et al.* [108].

3. Pressure is computed by taking the dot products of Eq. (2.4) with \mathbf{k} . Using incompressibility condition (Eq. (2.6)), one obtains

$$\sigma(\mathbf{k}, t) = \frac{i\mathbf{k}}{k^2} \cdot \text{FT}[\mathbf{u}(\mathbf{x}, t) \cdot \nabla \mathbf{u}(\mathbf{x}, t)] - \frac{i\mathbf{k} \cdot \hat{z}}{k^2} R\theta(\mathbf{k}, t).$$

The non-linear terms calculated in the previous step are used for the calculation of $\sigma(\mathbf{k})$.

4. Once the right-hand sides of the RBC equations (Eqs. (2.4) - (2.6)) are computed, the fourth-order Runge Kutta (RK4) scheme is used for the time advancement of the non-linear terms. An exponential trick is used for computing the diffusive term.
5. The time-step dt is computed using the CFL condition.
6. The steps are repeated until the final state is reached.

We validate our numerical code with the earlier results of Thual [12] by calculating the Nusselt numbers for 2D and 3D simulations in the box. The plot of temperature averaged over a horizontal planes show a sharp change near the horizontal walls and remains constant in the bulk of the container. This feature of the temperature inside the container confirms that our simulation is well-resolved. We use this code for two purposes: (i) to investigate the patterns and chaos for low-Prandtl number and zero-Prandtl number convection, and (ii) to investigate the dynamics of the energy cascade in the inertial range of the turbulence. In the following we discuss the different types of initial conditions that have been included in the code to investigate the dynamics of RBC flow.

2.1.2 Initial conditions

In numerical simulations, a good initial guess of the field helps in optimizing the simulation time for both the instability and the turbulence calculations. The patterns and instabilities near the onset depend critically on the initial conditions. In the turbulent regime, random initial conditions are preferred over the biased initial conditions. Furthermore, to save computational time, the turbulent state is reached by performing the numerical experiment in several steps. For example, simulation is performed for low Rayleigh numbers on a small grid and further the output of this run is fed to the run for a higher Rayleigh number convection on higher grid size. As we have performed our simulation to investigate the dynamics near the onset and in the fully turbulent regime,

different kinds of initial conditions are required to perform the simulation. The details of the initial conditions available in the code are as follows:

1. In the first type of condition, data are fed to run the simulation on the same grid size.
2. Data on smaller grid size are fed to run the simulation on higher grid size. This is useful to reach the simulation at the turbulent state starting from low Rayleigh number regime.
3. **Large scale velocity mode:** Some of the large scale modes are given as initial conditions. Due to a critical slowing down, simulations take a long time to reach the steady state for any arbitrary initial condition. Thus, this initial condition is useful to the investigations of the dynamics of static and time-dependent patterns near the onset.
4. **Large scale Vorticity modes:** Large scale vertical velocity, vertical vorticity and temperature modes are given as initial conditions to perform the numerical experiment in the regime where vertical vorticity modes play an important role in exciting instabilities. These initial conditions are useful for the numerical experiments near the onset for low-Prandtl number and zero-Prandtl number convection where vorticity plays an important role.
5. **Random initial conditions:** Initial random fields are generated by choosing the following form of the unidirectional energy and temperature spectra:

$$E(k) = \frac{ak^4}{(k^4 + q^4)^{1+\alpha}} \exp(-bk^{1.1}), \quad (2.7)$$

where $b = 0.02$, $q = 1.5$, $\alpha = 2.8/12$, and a is a free parameter [127]. The initial phases of the modes are randomly generated.

After discussing the numerical methods and different features of the 3D box code, we discuss a procedure to numerically calculate the energy spectra and fluxes of the velocity and temperature fields. In the following, we discuss these schemes in detail.

2.1.3 Calculation of the spectrum and flux

The numerical computation of the energy spectra and fluxes is quite tricky for turbulent fields. The energy spectra of the velocity field $E^u(k)$ and the temperature field $E^\theta(k)$ are calculated using the following formulae:

$$E^u(k) = \sum_{k \leq k' < k+1} \frac{1}{2} |u(\mathbf{k}')|^2, \quad (2.8)$$

$$E^\theta(k) = \sum_{k \leq k' < k+1} \frac{1}{2} |\theta(\mathbf{k}')|^2, \quad (2.9)$$

where the sum is being performed over the Fourier modes in the shell $(k, k + 1)$.

We compute the fluxes using the *mode to mode* energy transfer procedure. The energy flux from a sphere of radius k_0 is defined as the energy leaving per unit time from a wavenumber sphere to the outside of the sphere. This energy transfer takes place from the modes inside (giver) the wavenumber sphere to the modes outside (receiver) the sphere. This is computed as

$$\Pi^u(k_0) = \Im \left[\sum_{\mathbf{k}} k_j u_i^>(\mathbf{k}) \sum_{\mathbf{p}} u_j(\mathbf{k} - \mathbf{p}) u_i^<(\mathbf{p}) \right], \quad (2.10)$$

where the truncated variables $\mathbf{u}^>$ and $\mathbf{u}^<$ are defined as follows:

$$\mathbf{u}^>(\mathbf{k}) = \begin{cases} 0 & \text{if } |\mathbf{k}| < k_0 \\ \mathbf{u}(\mathbf{k}) & \text{if } |\mathbf{k}| > k_0, \end{cases} \quad (2.11)$$

$$\mathbf{u}^<(\mathbf{p}) = \begin{cases} \mathbf{u}(\mathbf{p}) & \text{if } |\mathbf{p}| < k_0 \\ 0 & \text{if } |\mathbf{p}| > k_0. \end{cases}$$

The \mathbf{p} summation in Eq. (2.10) is the convolution sum. The pseudo-spectral method can be used to compute the flux efficiently using the truncated variables $\mathbf{u}^>$ and $\mathbf{u}^<$. We repeat this process for the various values of k_0 for which we need the flux. In a similar fashion, we can compute the flux Π^θ of a scalar field θ . Convective turbulence is anisotropic, yet we compute the energy flux which is an average quantity over all angles.

For the energy flux calculation, we divide the wavenumber space into 20 shells. The

first three shells are $k = (0, 2)$, $[2, 4)$, and $[4, 8)$, and the last shell contains all modes beyond $k = 568$. Between $k = 8$ and $k = 568$, the wavenumber space is split into shells bounded by $[k_n, k_{n+1})$ with $k_n = 8 \times 2^{s(n-4)}$ where $s = (1/15) \ln_2(568/8)$. The numerical results regarding the energy spectra and fluxes will be presented in Chapter 4.

In the following section, we provide the details of the numerical schemes and procedures used to simulate RBC flow in a cylindrical container.

2.2 Finite-difference code for simulating convection in a cylindrical geometry

In this section, we provide details of the finite-difference code that has been used to investigate the dynamics of large scale circulation in a cylindrical container. The results pertaining to LSC are discussed in Chapter 5. The schematic diagram of the cylindrical container used for the study is shown in Fig. 2.1. The bottom plate is heated at $T = T_h$ and the top plate is cooled at $T = T_c$. For the temperature, the adiabatic condition ($\frac{\partial T}{\partial n} = 0$) has been implemented on the lateral walls. No-slip condition for the velocity field has been implemented on all the walls. In the following, we discuss the dynamical equations of the convective flow in cylindrical geometry.

2.2.1 Governing equations

The forms of the dynamical equations with different scalings have been discussed in detail in Chapter 1. In this sub-section, we discuss the details of the governing equations of Rayleigh-Bénard convection in the physical and computation domain. We choose the vertical height h of the container as the length scale, $(T_h - T_c)$ as the temperature scale, and the free-fall velocity $\left(\sqrt{\alpha g (T_h - T_c) h}\right)$ as the velocity scale, where α and g are the thermal expansion coefficient and acceleration due to gravity, respectively. The governing Boussinesq RBC equation in the cylindrical geometry (r, ϕ, z) will have the form [109]

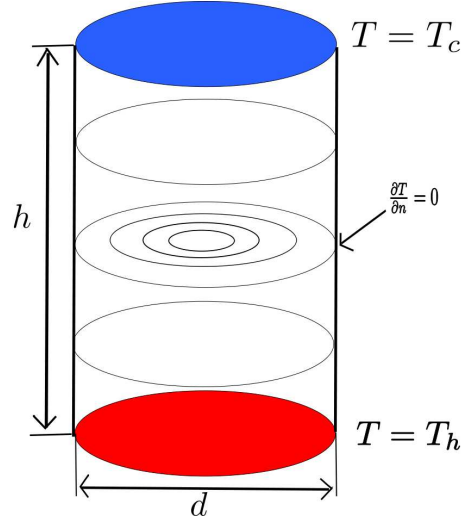


Figure 2.1: Schematic diagram of the cylindrical cell used for our study. Isothermal conditions on the horizontal walls and adiabatic condition on lateral walls are applied for the temperature. No-slip conditions for velocity fields are applied on all the walls. Circular lines show the locations of the ideal probes inserted at different locations of the container to characterize the temporal behaviour of RBC flow.

$$\frac{\partial u}{\partial t} + (\mathbf{u} \cdot \nabla)u - \frac{v^2}{r} = -\frac{\partial p}{\partial r} + \sqrt{\frac{P}{R}} \left(\Delta u - \frac{2}{r^2} \frac{\partial v}{\partial \phi} - \frac{u}{r^2} \right), \quad (2.12)$$

$$\frac{\partial v}{\partial t} + (\mathbf{u} \cdot \nabla)v + \frac{uv}{r} = -\frac{1}{r} \frac{\partial p}{\partial \phi} + \sqrt{\frac{P}{R}} \left(\Delta v + \frac{2}{r^2} \frac{\partial u}{\partial \phi} - \frac{v}{r^2} \right), \quad (2.13)$$

$$\frac{\partial w}{\partial t} + (\mathbf{u} \cdot \nabla)w = -\frac{\partial p}{\partial z} + \sqrt{\frac{P}{R}} \Delta w + T, \quad (2.14)$$

$$\frac{\partial T}{\partial t} + (\mathbf{u} \cdot \nabla)T = \frac{1}{\sqrt{RP}} \Delta T, \quad (2.15)$$

$$\frac{\partial u}{\partial r} + \frac{1}{r} \frac{\partial v}{\partial \phi} + \frac{\partial w}{\partial z} + \frac{u}{r} = 0, \quad (2.16)$$

where u , v , and w are, respectively, the radial, azimuthal, and vertical components of the velocity field (\mathbf{u}) in the cylindrical coordinates (r, ϕ, z) , and T is the temperature field. The operators are $\nabla \equiv \frac{\partial}{\partial r} + \frac{1}{r} \frac{\partial}{\partial \phi} + \frac{\partial}{\partial z}$, and $\Delta \equiv \frac{\partial^2}{\partial r^2} + \frac{1}{r^2} \frac{\partial^2}{\partial \phi^2} + \frac{\partial^2}{\partial z^2} + \frac{1}{r} \frac{\partial}{\partial r}$. Due to the presence of boundary layers near the container walls, non-uniform grids are chosen in the vertical and radial directions, and uniform grids are chosen in the azimuthal direction. But higher-order numerical schemes are compatible with the uniform grids. Therefore, the physical domain $\bar{x}(r, \phi, z)$ with non-uniform grids is transformed to another domain

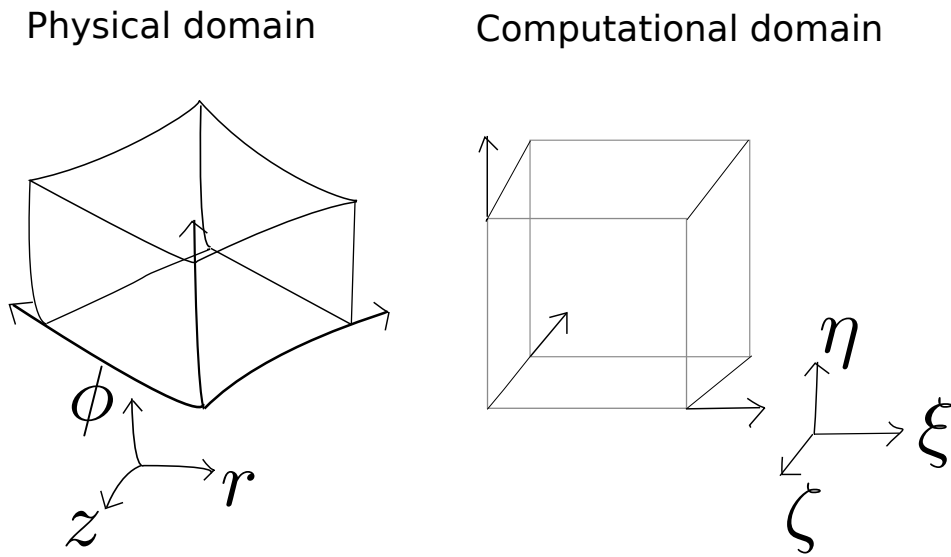


Figure 2.2: Schematic diagram of the physical (r, ϕ, z) and computational (ξ, η, ζ) domain of the simulation in a cylindrical geometry. The grids are non-uniform in the physical domain and uniform in the computational domain.

$\bar{\xi}(\xi, \eta, \zeta)$ with uniform grids. Fig. 2.2 shows a schematic view of the physical domain with non-uniform grids, and the transformed (computation) domain with uniform grids. In order to solve the equations in uniformly spaced grids, the governing equations are transformed according to the definition $\bar{x} = \bar{x}(\bar{\xi})$, i.e., for $r = r(\xi)$, $\phi = \phi(\eta)$, $z = z(\zeta)$. The corresponding metric tensor will be [110]

$$\xi_{ix_j} = \begin{pmatrix} \xi_r & 0 & 0 \\ 0 & \eta_\phi & 0 \\ 0 & 0 & \zeta_z \end{pmatrix} = \begin{pmatrix} r_\xi & 0 & 0 \\ 0 & \phi_\eta & 0 \\ 0 & 0 & z_\zeta \end{pmatrix}^{-1},$$

where $\xi_{ix_j} \equiv \frac{\partial \xi_i}{\partial x_j}$ and $x_{j\xi_i} \equiv \frac{\partial x_j}{\partial \xi_i}$. The above relation leads to a simplified relation between the direct and the inverse matrices:

$$\xi_r = \frac{1}{r_\xi} = \frac{\phi_\eta z_\zeta}{J}, \eta_\phi = \frac{1}{\phi_\eta} = \frac{r_\xi z_\zeta}{J}, \zeta_z = \frac{1}{z_\zeta} = \frac{r_\xi \phi_\eta}{J},$$

where the Jacobian of the metric tensor is given by $J = r_\xi \phi_\eta z_\zeta$.

The governing equations, Eqs. (2.12) - (2.16), in the transformed domain are

$$\frac{\partial u}{\partial t} + \frac{1}{J} (\mathbf{U} \cdot \nabla_{\bar{\xi}}) u + \frac{v^2}{r} = -\frac{1}{r_{\xi}} \frac{\partial p}{\partial \xi} + \sqrt{\frac{P}{R}} \left(\nabla_{\bar{\xi}}^2 u - \frac{2}{r^2 \phi_{\eta}} \frac{\partial v}{\partial \eta} - \frac{u}{r^2} \right), \quad (2.17)$$

$$\frac{\partial v}{\partial t} + \frac{1}{J} (\mathbf{U} \cdot \nabla_{\bar{\xi}}) v + \frac{uv}{r} = -\frac{1}{r \phi_{\eta}} \frac{\partial p}{\partial \eta} + \sqrt{\frac{P}{R}} \left(\nabla_{\bar{\xi}}^2 v + \frac{2}{r^2 \phi_{\eta}} \frac{\partial u}{\partial \eta} - \frac{v}{r^2} \right), \quad (2.18)$$

$$\frac{\partial w}{\partial t} + \frac{1}{J} (\mathbf{U} \cdot \nabla_{\bar{\xi}}) w = -\frac{1}{z_{\zeta}} \frac{\partial p}{\partial \zeta} + \sqrt{\frac{P}{R}} \nabla_{\bar{\xi}}^2 w + T, \quad (2.19)$$

$$\frac{\partial T}{\partial t} + \frac{1}{J} (\mathbf{U} \cdot \nabla_{\bar{\xi}}) T = \frac{1}{\sqrt{RP}} \nabla_{\bar{\xi}}^2 T, \quad (2.20)$$

$$\frac{1}{J} (\nabla_{\bar{\xi}} \cdot \mathbf{U}) + \frac{u}{r} = 0, \quad (2.21)$$

where the contravariant velocity (\mathbf{U}) is given by

$$U = \phi_{\eta} z_{\zeta} u, V = r_{\xi} z_{\zeta} v, W = r_{\xi} \phi_{\eta} w,$$

and the nabla operators in the transformed domain are given by

$$\nabla_{\bar{\xi}} = \frac{\partial}{\partial \xi} \hat{\xi} + \frac{\partial}{r \partial \eta} \hat{\eta} + \frac{\partial}{\partial \zeta} \hat{\zeta} \quad (2.22)$$

$$\nabla_{\bar{\xi}}^2 = \left(\frac{1}{r_{\xi}^2} \frac{\partial^2}{\partial \xi^2} + \frac{1}{r^2 \phi_{\eta}^2} \frac{\partial^2}{\partial \eta^2} + \frac{1}{z_{\zeta}^2} \frac{\partial^2}{\partial \zeta^2} \right) - \left(\frac{r_{\xi \xi}}{r_{\xi}^3} \frac{\partial}{\partial \xi} + \frac{z_{\zeta \zeta}}{z_{\zeta}^3} \frac{\partial}{\partial \zeta} \right) + \frac{1}{r r_{\xi}} \frac{\partial}{\partial \xi}. \quad (2.23)$$

Note that in deriving the dynamical equations, Eqs. (2.17) - (2.21), in the transformed domain, only the gradient operators are changed to the corresponding transformed domain, whereas the other variables are left in the physical domain.

2.2.2 Numerical techniques

The governing equations (Eqs. (2.17) - (2.21)) are solved using a semi-explicit scheme. To avoid velocity-pressure decoupling, a staggered grid arrangement for the variables is used with the temperature defined at the centre of the cell. The Predictor-corrector algorithm has been used to solve the equations [110]. Under this scheme, a provisional velocity

field that does not satisfy the continuity equation is initially guessed using a pressure at previous time, and then it is corrected by solving a Poisson equation for pressure correction in the previous step. This corrected velocity field satisfies the continuity equation, and the new pressure values are obtained simultaneously. Once the velocity field is calculated, the temperature field is calculated using the divergence-free velocity field. However, in the z-momentum equation, the temperature is taken explicitly to avoid further coupling between the equations. In the following, we describe the details of the algorithm for the Predictor-corrector method used to solve the equations.

2.2.3 Predictor-corrector method

For time-advancement, a second-order Adams-Bashforth scheme is used for the non-linear terms, and the Crank-Nicholson scheme is used for the diffusive terms [110]. Further, pressure is considered as an implicit variable. Under this procedure, the governing equations will have the form

$$\frac{u_P^{n+1} - u_P^n}{\Delta t} + \frac{1}{2}(3C_{u_P}^n - C_{u_P}^{n-1}) = -\frac{1}{r_\xi} \frac{\partial p^{n+1}}{\partial \xi} + \frac{\alpha_v}{2}(Du_P^{n+1} + Du_P^n), \quad (2.24)$$

$$\frac{v_P^{n+1} - v_P^n}{\Delta t} + \frac{1}{2}(3C_{v_P}^n - C_{v_P}^{n-1}) = -\frac{1}{r\phi_\eta} \frac{\partial p^{n+1}}{\partial \eta} + \frac{\alpha_v}{2}(Dv_P^{n+1} + Dv_P^n), \quad (2.25)$$

$$\frac{w_P^{n+1} - w_P^n}{\Delta t} + \frac{1}{2}(3C_{w_P}^n - C_{w_P}^{n-1}) = -\frac{1}{z_\zeta} \frac{\partial p^{n+1}}{\partial \zeta} + \frac{\alpha_v}{2}(Dw_P^{n+1} + Dw_P^n) + T^n, \quad (2.26)$$

where the subscript P represents the particular grid point on which the velocities (u , v , w) are defined in the computational domain, $\alpha_v = \sqrt{\frac{P}{R}}$ and C , D correspond to the discretized *effective* convective and diffusive operators, respectively. Note that here the convective (C) and diffusive (D) operators contain some extra terms apart from the usual operators (see Eqs. (2.17)- (2.20)). From the above equations we see that the calculation of the velocity fields at the n^{th} time level depends on the pressure at $(n+1)^{th}$ level. Thus, the Predictor-corrector scheme is used to solve the equations. In this method, the provisional velocity field (\tilde{u}), which need not satisfy the continuity equations, is calculated using the the known pressure at the n^{th} time level. The corresponding equations with the

provisional velocity will be

$$\frac{\tilde{u}_P - u_P^n}{\Delta t} + \frac{1}{2}(3C_{u_P}^m - C_{u_P}^{m-1}) = -\frac{1}{r_\xi} \frac{\partial p^n}{\partial \xi} + \frac{\alpha_v}{2}(D\tilde{u}_P + Du_P^n), \quad (2.27)$$

$$\frac{\tilde{v}_P - v_P^n}{\Delta t} + \frac{1}{2}(3C_{v_P}^m - C_{v_P}^{m-1}) = -\frac{1}{r\phi_\eta} \frac{\partial p^n}{\partial \eta} + \frac{\alpha_v}{2}(D\tilde{v}_P + Dv_P^n), \quad (2.28)$$

$$\frac{\tilde{w}_P - w_P^n}{\Delta t} + \frac{1}{2}(3C_{w_P}^m - C_{w_P}^{m-1}) = -\frac{1}{z_\zeta} \frac{\partial p^n}{\partial \zeta} + \frac{\alpha_v}{2}(D\tilde{w}_P + Dw_P^n) + T^n. \quad (2.29)$$

Eqs. (2.27)-(2.29) constitute the predictor steps that give the provisional velocity \tilde{u} . The corresponding contravariant velocities can be calculated using their respective definitions

$$\tilde{U} = \phi_\eta z_\zeta \tilde{u}, \tilde{V} = r_\xi z_\zeta \tilde{v}, \tilde{W} = r_\xi \phi_\eta \tilde{w}. \quad (2.30)$$

When Eqs. (2.27)-(2.29) are correspondingly subtracted from Eqs. (2.24)-(2.26), the relations between the velocity and pressure correction can be obtained. Thus, the velocity corrections will have the form

$$u'_P = u_P^{n+1} - \tilde{u}_P = -\frac{\Delta t}{r_\xi} \frac{\partial p'}{\partial \xi} + \frac{\alpha_v \Delta t}{2} Du'_P, \quad (2.31)$$

$$v'_P = v_P^{n+1} - \tilde{v}_P = -\frac{\Delta t}{r\phi_\eta} \frac{\partial p'}{\partial \eta} + \frac{\alpha_v \Delta t}{2} Dv'_P, \quad (2.32)$$

$$w'_P = w_P^{n+1} - \tilde{w}_P = -\frac{\Delta t}{z_\zeta} \frac{\partial p'}{\partial \zeta} + \frac{\alpha_v \Delta t}{2} Dw'_P, \quad (2.33)$$

where the pressure correction (p') is defined as $p' = p^{n+1} - p^n$.

In order to obtain a compact formula for the velocity correction, the contribution of the diffusions operator in Eqs. (2.31) - (2.33) are discarded, which leads to

$$u' = -\frac{1}{a_{Pu}} \frac{\Delta t}{r_\xi} \frac{\partial p'}{\partial \xi}, v' = -\frac{1}{a_{Pv}} \frac{\Delta t}{r\phi_\eta} \frac{\partial p'}{\partial \eta}, w' = -\frac{1}{a_{Pw}} \frac{\Delta t}{z_\zeta} \frac{\partial p'}{\partial \zeta}, \quad (2.34)$$

where the coefficients a_{pu} , a_{pv} , and a_{pw} contain the contribution to the velocity correction at the point P given by

$$a_{Pu} = a_{Pv} = a_{Pw} = 1 + \alpha \Delta t \left(\frac{1}{r_\xi^2} \frac{1}{\Delta \xi^2} + \frac{1}{r^2 \phi_\eta^2} \frac{1}{\Delta \eta^2} + \frac{1}{z_\zeta^2} \frac{1}{\Delta \zeta^2} \right). \quad (2.35)$$

Note that a_{Pu}, a_{Pv} , and a_{Pw} have the same formula but they are computed at the different u , v , and w node points, respectively. By using the definition of the contravariant velocities,

$$U_P^{n+1} = \tilde{U}_P + \phi_\eta z_\zeta u'_P, \quad (2.36)$$

$$V_P^{n+1} = \tilde{V}_P + r_\xi z_\zeta v'_P, \quad (2.37)$$

$$W_P^{n+1} = \tilde{W}_P + r_\xi \phi_\eta w'_P, \quad (2.38)$$

and substituting Eqs. (2.34) and (2.36)- (2.38) in the transformed continuity Eq. (2.21), a Poisson equation for the pressure correction is obtained :

$$\frac{u^{n+1}}{r} + \frac{1}{J} \left[\left(\frac{\partial U}{\partial \xi} \right)^{n+1} + \left(\frac{\partial V}{r \partial \eta} \right)^{n+1} + \left(\frac{\partial W}{\partial \zeta} \right)^{n+1} \right] = 0 \quad (2.39)$$

$$\implies \frac{u'}{r} + \frac{1}{J} \left(\frac{\partial U'}{\partial \xi} + \frac{\partial V'}{r \partial \eta} + \frac{\partial W'}{\partial \zeta} \right) = -\frac{1}{J} \left(\frac{\partial \tilde{U}}{\partial \xi} + \frac{\partial \tilde{V}}{r \partial \eta} + \frac{\partial \tilde{W}}{\partial \zeta} \right) - \frac{\tilde{u}}{r} \quad (2.40)$$

$$\begin{aligned} \implies \frac{1}{J} \left[\frac{\partial}{\partial \xi} \left(\frac{\phi_\eta z_\zeta}{a_{Pu} r_\xi} \frac{\partial p'}{\partial \xi} \right) + \frac{\partial}{r \partial \eta} \left(\frac{r_\xi z_\zeta}{a_{Pv} \phi_\eta} \frac{\partial p'}{\partial \eta} \right) + \frac{\partial}{\partial \zeta} \left(\frac{r_\xi \phi_\eta}{a_{Pw} z_\zeta} \frac{\partial p'}{\partial \zeta} \right) + \frac{\phi_\eta z_\zeta}{a_{pu}} \frac{\partial p'}{r \partial \xi} \right] \\ = \frac{1}{J \Delta t} \left(\frac{\partial \tilde{U}}{\partial \xi} + \frac{\partial \tilde{V}}{r \partial \eta} + \frac{\partial \tilde{W}}{\partial \zeta} + \frac{r_\xi \tilde{U}}{r} \right) \end{aligned} \quad (2.41)$$

$$\implies \nabla_{\xi}^2 p' = \frac{1}{a_{Pu} J \Delta t} \left(\frac{\partial \tilde{U}}{\partial \xi} + \frac{\partial \tilde{V}}{r \partial \eta} + \frac{\partial \tilde{W}}{\partial \zeta} + \frac{r_\xi \tilde{U}}{r} \right). \quad (2.42)$$

Coefficients a_{Pu} , a_{Pv} , and a_{Pw} are held constant in Eq. (2.41) to derive the Poisson equation for the pressure correction. The nabla operator in Eq. (2.42) is the same as given by Eq. (2.23). The solution of Eq. (2.42) provides the pressure correction field which using Eq. (2.34) corrects the provisional velocity field to yield the $(n+1)^{th}$ time-level values that satisfy the continuity equation. Using the divergence-free velocity field, the temperature equation can be time-advanced by using the Adams-Bashforth method for the non-linear term and the Crank-Nicholson method for the diffusive term. Thus the form of the temperature equations will be

$$\frac{T^{n+1} - T^n}{\Delta t} + \frac{1}{2} (3C_T^m - C_T^{m-1}) = \frac{1}{2\sqrt{RP}} (DT^{n+1} + DT^n), \quad (2.43)$$

where C and D are the convective and diffusive operators mentioned above.

2.2.4 Solution algorithm

In the following, we present a flow chart of the algorithm used for the calculation of the fields for RBC flow in a cylindrical container using the finite-difference scheme.

Step 1: At first, the velocity, pressure, and temperature fields are initialized with random values.

Step 2: A provisional velocity field $(\tilde{u}, \tilde{v}, \tilde{w})$ are calculated using Eqs. (2.27) - (2.29) with known pressure fields.

Step 3: Contravariant velocities $\tilde{U}, \tilde{V}, \tilde{W}$ are predicted using the relations given in Eqs. (2.36) - (2.38).

Step 4: The divergence of the predicted contravariant velocity $\nabla \cdot \tilde{\mathbf{U}}$, which is used as the source term in the Poisson equation (Eq. (2.42)) for the pressure correction, is calculated.

Step 5: Eq. (2.42) is solved for the pressure correction field using the Gauss-Siedel Successive Overrelaxation (GSSOR) method.

Step 6: The corrected velocity is calculated using Eq. (2.34) and, subsequently, the provisional velocity fields are updated using the relations, $\tilde{u} = \tilde{u} + u'$, $\tilde{v} = \tilde{v} + v'$ and $\tilde{w} = \tilde{w} + w'$, while the pressure field is updated using $p = p + p'$, and the corresponding contravariant velocity fields using Eq. (2.41).

Step 7: Next, the divergence conditions for the free velocity field are checked. If $\frac{1}{J} \left| \left(\frac{\partial \tilde{U}}{\partial \xi} + \frac{\partial \tilde{V}}{\partial \eta} + \frac{\partial \tilde{W}}{\partial \zeta} + \frac{r_\xi \tilde{U}}{r} \right) \right| < \epsilon$ (the convergence limit), the divergence-free velocity field is obtained, i.e., $\tilde{u} \rightarrow u^{n+1}$, $\tilde{v} \rightarrow v^{n+1}$, $\tilde{w} \rightarrow w^{n+1}$, otherwise the process again starts from **Step 4**.

Step 8: Using the divergence-free velocity field, the temperature field T^{n+1} is calculated using Eq. (2.43).

Step 9: For the calculation of the fields at the next time step, the above mentioned processes are repeated from **Step 2** onwards.

2.2.5 Discretization of the fields and other numerical details

The fields in the convective parts of Eqs. (2.17) - (2.21) are discretized using Tamm and Webb's [111] fourth order central explicit scheme with enhanced spectral resolution. This scheme uses a seven point stencil for the calculation of the derivative, as is shown below:

$$\psi'_j = \frac{1}{h} [0.02651995(\psi_{j+3} - \psi_{j-3}) - 0.18941314(\psi_{j+2} - \psi_{j-2}) + 0.79926643(\psi_{j+1} - \psi_{j-1})]. \quad (2.44)$$

However, the second order central difference scheme has been used to discretize the diffusive parts of the equations. The convergence limit for all the equations including the three provisional velocities is set at 10^{-5} .

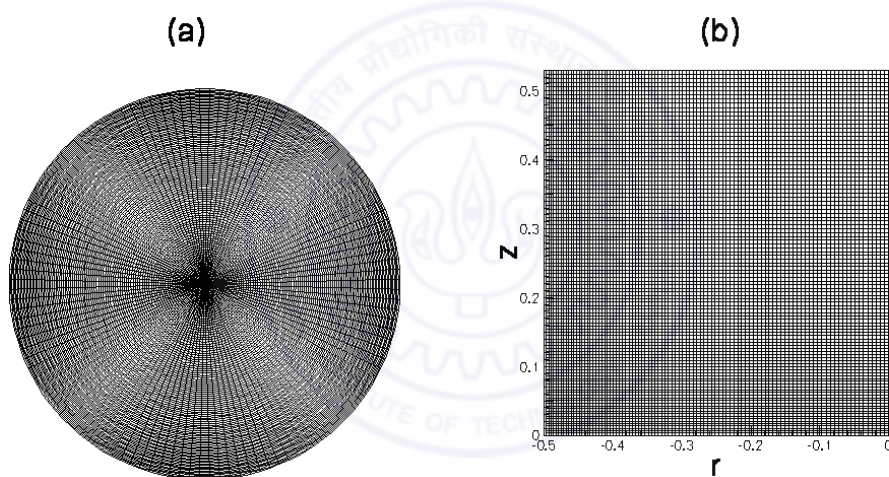


Figure 2.3: Distribution of $100 \times 120 \times 201$ grids in (a) a horizontal ($z = 0.5$), and (b) a vertical ($\theta = 3\pi/4$) plane of a cylindrical container of aspect ratio one.

Due to presence of thermal and velocity boundary layers near the top and bottom plates, and the lateral wall, we use non-uniform grids along the radial and vertical directions. A uniform grid is used along the azimuthal direction. The following function has been used for the distribution of the grids along the radial and vertical directions [112]:

$$z = h \frac{(\beta + 2\alpha)[(\beta + 1)/(\beta - 1)]^{(z_u - \alpha)/1 - \alpha} - \beta + 2\alpha}{(1 + 2\alpha)\{1 + (\beta + 1)/(\beta - 1)\}^{(z_u - \alpha)/1 - \alpha}}, \quad (2.45)$$

where $\beta > 1$ is the stretching parameter that refines the grid near the boundary layers.

In our simulation, we take $\alpha = 0.5$, and $\beta = 1.5$. h is the vertical height of the container, and z_u is the uniformly distributed grid in a domain of length 1. We have used a similar distribution of grids along the radial directions of the container. Fig. 2.3(a) and Fig. 2.3(b) show the distribution of $100 \times 120 \times 201$ grids in a horizontal plane ($z = 0.5$) and a vertical plane ($\phi = 3\pi/4$) respectively. The grids are more closely spaced near the top plates ($z \sim 0.02$), bottom plates ($z \sim 0.98$) and near the lateral walls ($r \sim -0.5$).

R	$N_r \times N_\theta \times N_z$	dt	Nu (comp)	Nu (I)	Nu (II)
6×10^5	$33 \times 49 \times 97$	0.001	7.6	7.5	7.5
8×10^6	$75 \times 96 \times 145$	0.001	15.1	16.8	16.8
2×10^7	$100 \times 120 \times 201$	0.0005	22.1	22.3	22.3
3×10^7	$100 \times 180 \times 201$	0.0005	24.03	25.3	25.3

Table 2.1: Comparison of Nu as calculated from our simulation with earlier numerical and experimental results. N_r , N_θ , and N_z are the number of grids along the radial, azimuthal, and vertical directions of the cylindrical container; $Nu(\text{comp})$ is the Nusselt number obtained from our simulations; $Nu(I)$ is the Nusselt number reported in the numerical simulation by Stringano and Verzicco [101]; and $Nu(II)$ is the Nusselt number observed in the laboratory experiment by Niemela *et al.* [68].

We validate our code by calculating the Nusselt number (Nu) for a range of Rayleigh numbers varying from $R = 6 \times 10^5$ to 3×10^7 and compare these with earlier numerical and experimental results. The Prandtl number taken for our simulations is $P = 0.7$. Table 2.1 shows the comparison of Nu calculated from our numerical results with those of Stringano and Verzicco [101] and of Niemela *et al.* [68]. We find a good agreement between our results and the earlier results. Our numerical results on the Nusselt number (Nu) for different Rayleigh numbers approximately obey a relationship of the form $Nu \simeq 0.143R^{0.297}$.

In the next chapter, we will discuss the patterns and chaos near the onset for low-Prandtl number and zero-Prandtl number convection.

Chapter 3

Patterns and bifurcations in low- P and zero- P convection

3.1 Introduction

In this chapter, we construct bifurcation diagrams for low-Prandtl number convection using DNS and low-dimensional models. Low-Prandtl number fluids, such as, for example, mercury ($P \approx 0.02$), liquid sodium ($P \approx 0.01$), solar plasma in the convective zone ($P \sim 10^{-3}$), exhibit interesting convective patterns and chaos [8, 9, 10, 11, 113, 114]. For low-Prandtl number (low- P), the inertial term $\mathbf{u} \cdot \nabla \mathbf{u}$ becomes quite important and generates the vertical vorticity. As a result, the flow pattern becomes three-dimensional, and oscillatory waves along the horizontal axes are generated just near the onset of convection [13]. The instabilities and patterns near the onset for low- P have been studied analytically [7, 15, 18, 19, 20, 21, 22, 23], experimentally [6, 8, 9, 27, 28, 29], and numerically [12, 24, 30, 31, 32]. These works have been reviewed in more detail in Chapter 1. Busse [13] showed, using perturbative analysis, that for small Prandtl numbers, the 2D rolls become unstable when the amplitude of the convective motion exceeds a critical value. Busse and Bolton [15] argued that under free-slip boundary conditions, the stability of the 2D rolls exists only for Prandtl numbers above a critical value P_c , which is around 0.543. Clever and Busse [17] extended the oscillatory instability analysis to no-slip boundary conditions and showed that the convective rolls are unstable for Prandtl

numbers less than about 5.

Straight two-dimensional (2D) rolls that have zero vertical vorticity are neutrally stable solution of zero-P convection at $r = 1$. However, they become unstable for $r > 1$. Thual [12] and Kumar *et. al.* [39] showed that these 2D rolls saturate through the generation of vertical vorticity (wavy rolls) for $r > 1$ of zero-P fluids. Thual [12] performed a DNS to study the different types of instabilities that occur for low-P and zero-P convection and established that zero-P convection may be treated as a limiting approximation of low-P convection.

Several low-dimensional models have been proposed to study the patterns and instabilities near the onset for low-Prandtl number and zero-Prandtl convection. Kumar, Fauve and Thual [39] showed using a 6-mode model of zero-P convection that the growth of the 2D rolls saturate through the generation of the vertical vorticity (wavy nature). Kumar, Pal and Fauve [41] observed critical bursting in the above model during saturation. Pal and Kumar [42] explained the mechanism of the selection of the square patterns using a 15-mode model of zero-P RBC. Recently, Pal *et al.* [43] constructed a 13-mode low-dimensional model for zero-P convection and performed bifurcation analysis for the same. They observed various convective patterns including squares, asymmetric squares, oscillating asymmetric squares, relaxation oscillations with an intermediate square pattern, and chaos in their model. Pal *et al.* [115] have generalized the 13-mode model to a 27-mode model by incorporating some of the vorticity modes that induce the wavy nature.

The main motivation of our study is to understand the dynamics of different non-linear instabilities that appear near the onset of convection for low-P convection through DNS and low-dimensional models. In this chapter, we present a detailed analysis of the instabilities and bifurcations observed near the onset for low-P convection. This work is published in *Europhys. Lett.* [38]. We perform the DNS on a 64^3 grid size in a 3D box with free-slip and conducting boundary conditions on the top and bottom plates, and periodic condition in the horizontal directions. Using DNS results as a guiding tool, we construct low-dimensional models with the active large scale modes present in the regime near the onset for low-P convection and perform a detailed bifurcations analysis. The low-P convection exhibits static patterns, such as rolls, squares, asymmetric squares, and time-

dependent patterns, such as oscillating asymmetric squares, and relaxation oscillations. We observe the presence of chaotic attractors both in the DNS and the low-dimensional model for low-Prandtl number ($P \lesssim 0.005$). However, low-P convective flows always exhibit stationary 2D rolls and associated stationary and oscillatory asymmetric squares in contrast to zero-P convection, where chaos appears at the onset itself [43].

First, we present the DNS results and bifurcation analysis of the related low-dimensional models for low-P convection. Subsequently, we present the DNS results and the low-dimensional model of zero-P convection, and compare the results with the bifurcations results of the low-P convection.

3.2 Bifurcation analysis of low-P RBC

3.2.1 Direct numerical simulations for low-P convection

We consider a layer of Boussinesq fluid with infinite horizontal extension confined within a 3D box with perfectly conducting and free-slip boundary conditions at the top and bottom plates and periodic boundary conditions along the horizontal directions. The relevant equations (under Boussinesq approximation) in non-dimensionalized form for low-Prandtl number convection are discussed in Chapter 1 [Eqs. (1.22) - (1.25)]. The main control parameters for these equations are the Rayleigh number (R) and the Prandtl number (P). For our analysis we will typically use the reduced Rayleigh number $r = R/R_c$, where R_c is the critical Rayleigh number, as the control parameter.

We perform direct numerical simulations of the convective flows for $P = 0.02, 0.005, 0.002$ and 0.0002 and for r ranging from 1 to 1.25 on a 64^3 rectangular grid. The detailed numerical schemes used to solve the dynamical equations of low-P convection in a 3D box have been discussed in Chapter 2. We use the fourth order Runge-Kutta scheme for the time-stepping. The aspect ratio of our simulations is given by $\Gamma_x = L_x/d = 2\sqrt{2}$, and $\Gamma_y = L_y/d = 2\sqrt{2}$. Eqs. (1.22) and (1.24) provide us an estimate of dt for the DNS ($dt \sim P\theta/v_3 \sim P/R$). For $P = 0.0002$, $dt \sim 10^{-7}$, which makes numerical simulations very demanding.

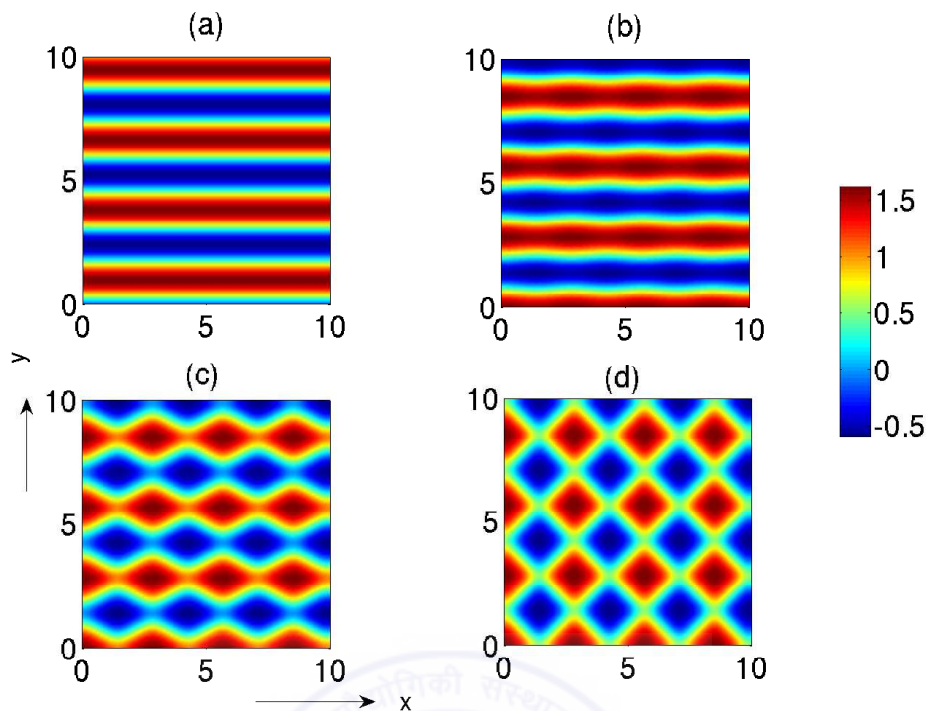


Figure 3.1: Static patterns in the mid-plane of the 3D convection box observed in DNS near the onset for $P = 0.02$ on a 64^3 grid. Temperature snapshots at: (a) $r = 1.0005$ exhibits a roll pattern, (b) $r = 1.007$ exhibits a “weak” asymmetric square (ASQ) pattern, (c) $r = 1.186$ exhibits a “strong” asymmetric square (ASQ) pattern, and (d) $r = 1.217$ exhibits a square (SQ) pattern. Blue and red regions represent, respectively, the downflow and upflow of the convection.

In DNS of low-Prandtl number convection, we observe various static patterns such as 2D rolls, asymmetric squares (ASQ), squares (SQ), and time-dependent patterns such as oscillatory asymmetric squares (OASQ), oscillatory rolls with squares in the intermediate regime, and chaotic attractors near the onset of convection. Some of these patterns were first observed in the numerical observations of Thual [12] and Meneguzzi *et al.* [32] for low- P and/or zero- P convection. For $P = 0.02$, Fig 3.1 shows the static convective flow patterns in the mid-plane of 3D box at different values of the Rayleigh number near the onset of convection. The red and blue regions represent the upcoming and downgoing convective flows, respectively. Fig. 3.1(a) exhibits straight rolls along the x -axis observed at $r = 1.0005$. Note that the orientation of the roll solutions depends on the nature of the initial perturbations in the numerical simulations. As the Rayleigh number is increased, rolls start appearing in the perpendicular direction and the superposition of the two perpendicular rolls gives rise to static asymmetric square (ASQ) and square

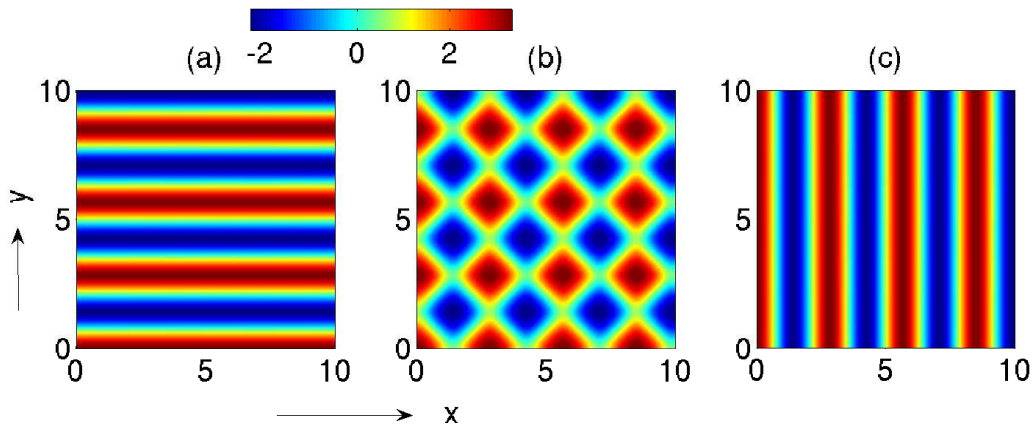


Figure 3.2: Relaxation oscillation with an intermediate square regime (SQOR) pattern observed in the DNS at $r = 1.031$ for $P = 0.02$. Snapshots of temperature at: (a) $t = 0$, (b) $t = T/4$, and (c) $t = T/2$, where T is the time period of the oscillation.

(SQ) patterns. The two perpendicular rolls have unequal intensity for ASQ patterns while they have equal intensity for SQ patterns. Figs. 3.1((b),(c)) show the “weak” and “strong” asymmetric square patterns respectively. In Fig. 3.1(b), the roll along the x -axis dominates strongly on roll along the y -axis. However, in Fig. 3.1(c), both the rolls, i.e., along the x - and y -axes, have unequal but comparable intensity. Fig. 3.1(d) shows the square patterns that are the result of the superposition of the two perpendicular rolls with equal magnitudes.

Apart from the above-described static patterns, we also observe a variety of time dependent patterns in the DNS for low-Prandtl number convection. For $P = 0.02$ at $r = 1.031$, Fig. 3.2 shows a periodic transition from the roll pattern in one direction to the roll pattern in the perpendicular direction with a square pattern as an intermediate pattern. Thual [12] observed this dynamical pattern for the first time in his numerical simulation and he termed this as the “relaxation oscillations with intermediate squares (SQOR) pattern”. Fig. 3.2(a) shows the roll along the x -axis at $t = 0$; Fig. 3.2(b) shows the intermediate square at $t = T/4$ (T is the time period of the oscillation); and Fig. 3.2(c) shows the roll along the y -axis at $t = T/2$. In another type of time-dependent pattern, we observe a periodic distortion of the roll in the transverse direction. This is called as the “oscillatory asymmetric square (OASQ) pattern”. Fig. 3.3(a) and Fig. 3.3(b) show the

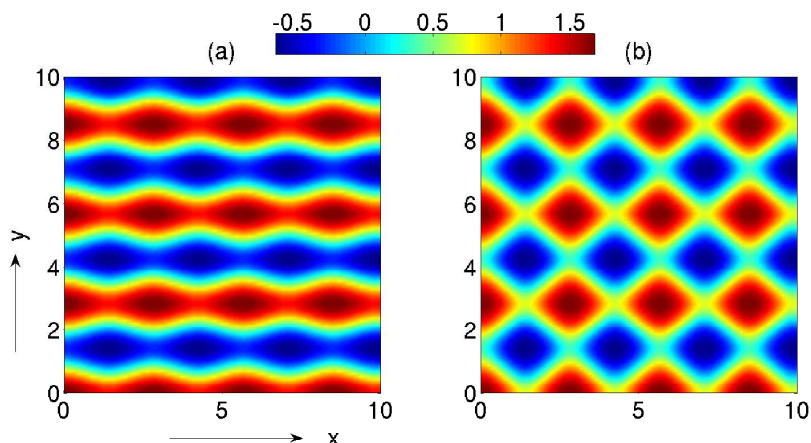


Figure 3.3: Oscillating asymmetric square (OASQ) pattern observed in the DNS for $P = 0.02$ at $r = 1.110$. Snapshots of temperature at: (a) $t = 0$, (b) $t = T/2$, where T is the time period of the oscillation.

OASQ patterns at $t = 0$ and $t = T/2$, respectively, for $P = 0.02$ at $r = 1.110$. Thual [12] reported this as a propagation of oscillatory standing wave along the roll axis. Note that this pattern is different from the wavy roll in which a travelling wave moves along the axis of the roll.

We observe similar types of static and time-dependent patterns for other low Prandtl numbers ($P = 0.002, 0.005, 0.0002$) considered for our study. However, the range of the stable roll solution that appears near the onset decreases with the decrease of the Prandtl number. For low Prandtl numbers ($P = 0.005$ and $P = 0.0002$), we also observe chaotic behaviour of the flow near the onset.

The origin of different static and time-dependent patterns observed in the DNS for low-Prandtl number convection appears to be very complicated. Each run of the simulation takes a significantly long period of time, so it is not possible to explore the whole parameter regime. Moreover, the requirement of high temporal resolution for low-Prandtl number convection near the onset makes the DNS very demanding. So, for a systematic study of these instabilities we construct a low-dimensional model of low-Prandtl number convection. In the next subsection, we present a brief discussion on the construction of the low-dimensional model.

3.2.2 Low-dimensional model

In the DNS, we observe regular and chaotic patterns near the onset of convection. As we carefully analyze the DNS data, we find that a few large scale modes are instrumental in the dynamics of convection near the onset. Using these important modes, we construct a 30-mode low-dimensional model for low-Prandtl number convection. We run the model and the DNS in the range of $r = 1 - 1.25$. Commulative energy contained in these modes ranges from 85% to 98% of the total energy of the DNS, and each of these modes has 1% or more of the total energy. We pick 11 large-scale vertical velocity modes: $W_{101}, W_{011}, W_{112}, W_{211}, W_{121}, W_{301}, W_{103}, W_{013}, W_{031}, W_{202}$, and W_{022} ; 12 large-scale θ modes: $\theta_{101}, \theta_{011}, \theta_{112}, \theta_{211}, \theta_{121}, \theta_{301}, \theta_{103}, \theta_{013}, \theta_{031}, \theta_{202}, \theta_{022}$, and θ_{002} ; and 7 large-scale vertical vorticity modes: $Z_{110}, Z_{112}, Z_{211}, Z_{121}, Z_{220}, Z_{310}$, and Z_{130} . The three subscripts here are the indices of the wavenumbers along the x -, y -, and z -directions. All the Fourier modes, 30 in total, are taken to be real. Expansion of these vertical velocity modes (v_3), temperature (θ), and vertical vorticity modes (ω_3) yields

$$\begin{aligned}
v_3(x, y, z, t) = & W_{101}(t) \cos(kx) \sin(\pi z) + W_{011}(t) \cos(ky) \sin(\pi z) \\
& + W_{112}(t) \cos(kx) \cos(ky) \sin(2\pi z) + W_{211}(t) \cos(2kx) \cos(ky) \sin(\pi z) \\
& + W_{121}(t) \cos(kx) \cos(2ky) \sin(\pi z) + W_{202}(t) \cos(2kx) \sin(2\pi z) \\
& + W_{022}(t) \cos(2ky) \sin(2\pi z) + W_{103}(t) \cos(kx) \sin(3\pi z) \\
& + W_{013}(t) \cos(ky) \sin(3\pi z) + W_{301}(t) \cos(3kx) \sin(\pi z) \\
& + W_{031}(t) \cos(3ky) \sin(\pi z), \tag{3.1}
\end{aligned}$$

$$\begin{aligned}
\theta(x, y, z, t) = & \theta_{101}(t) \cos(kx) \sin(\pi z) + \theta_{011}(t) \cos(ky) \sin(\pi z) \\
& + \theta_{112}(t) \cos(kx) \cos(ky) \sin(2\pi z) + \theta_{211}(t) \cos(2kx) \cos(ky) \sin(\pi z) \\
& + \theta_{121}(t) \cos(kx) \cos(2ky) \sin(\pi z) + \theta_{202}(t) \cos(2kx) \sin(2\pi z) \\
& + \theta_{022}(t) \cos(2ky) \sin(2\pi z) + \theta_{103}(t) \cos(kx) \sin(3\pi z) \\
& + \theta_{013}(t) \cos(ky) \sin(3\pi z) + \theta_{301}(t) \cos(3kx) \sin(\pi z) \\
& + \theta_{031}(t) \cos(3ky) \sin(\pi z) + \theta_{002}(t) \sin(2\pi z), \tag{3.2}
\end{aligned}$$

$$\begin{aligned}
\omega_3(x, y, z, t) = & Z_{110}(t) \sin(kx) \sin(ky) + Z_{112}(t) \sin(kx) \sin(ky) \cos(2\pi z) \\
& + Z_{211}(t) \sin(2kx) \sin(ky) \cos(\pi z) + Z_{121}(t) \sin(kx) \sin(2ky) \cos(\pi z) \\
& + Z_{220}(t) \sin(2kx) \sin(2ky) + Z_{310}(t) \sin(3kx) \sin(ky) \\
& + Z_{130}(t) \sin(kx) \sin(3ky).
\end{aligned} \tag{3.3}$$

The modes (1,0,1) and (0,1,1) are the most important modes of our model; they represent the rolls along the y - and x -directions, respectively. For the square pattern, the most important participating triad is [(1, 0, 1), (0, 1, 1), (1, 1, 2)]. Note that the wavenumbers of the interacting triad satisfy $\mathbf{k} = \mathbf{p} + \mathbf{q}$.

We compute the horizontal components of the velocity using the incompressibility condition for the velocity field [Eq. (1.25)]. Next, we perform a Galerkin projection of the RBC equations [Eqs. (1.22) - (1.24)] on the above modes, and obtain a set of thirty dimensional coupled ordinary differential equations for the amplitudes of the above Fourier modes. In the next subsection, we present the detailed bifurcation analysis of the low-P convection using this 30-mode low-dimensional model.

3.2.3 Bifurcations for low-P convection

We numerically solve the 30-mode model by employing accurate implicit ODE solvers from MATLAB. As the selection of large-scale modes for this model are motivated by the DNS results, we observe a variety of convective patterns: square (SQ), asymmetric square (ASQ), oscillating asymmetric squares (OASQ), relaxation oscillation with an intermediate square regime (SQOR), etc. Furthermore, the values of modes selected for the construction of the low-dimensional model match quite well with the values in the DNS. Table 3.1 shows the Fourier amplitude of the vertical velocity modes as calculated in the DNS and low-dimensional model at $r = 1.156$ (ASQ regime) and $r = 1.217$ (SQ regime) for $P = 0.02$. Stable steady values of the modes for the SQ and ASQ patterns match with the corresponding DNS values within 10%. This shows the accuracy of our low-dimensional analysis for the selected range of our study. Note that earlier Thual [12] and Meneguzzi *et al.* [32] showed the existence of SQ, SQOR, oscillatory quasi-hexagons

(SQOS), chaotic squares (SQCH) and chaotic quasi-hexagons (HXCH) in their DNS for low-Prandtl numbers. We observe OASQ and several chaotic patterns in addition to the above patterns observed by Thual [12] and Meneguzzi *et al.* [32].

-	Model Values	DNS values	Model Values	DNS values
Modes	$r = 1.156$	$r = 1.156$	$r = 1.217$	$r = 1.217$
W_{101}	9.6	9.4	14.9	14.1
W_{011}	17.8	20.2	14.9	14.1
W_{112}	-3.0	-1.7	-3.4	-1.7
W_{211}	-2.4	-1.2	-5.8	-2.5
W_{121}	-5.4	-2.9	-5.8	-2.5
W_{301}	1.3	0.9	2.5	1.8
W_{103}	0.3	0.3	0.4	0.4
W_{013}	0.3	0.3	0.4	0.4
W_{031}	1.2	1.2	1.8	2.5
W_{202}	1.0	0.9	1.4	1.6
W_{022}	1.0	1.0	1.4	1.0

Table 3.1: A comparison between the values of the amplitudes of the vertical velocity Fourier modes in the DNS and the low-dimensional model for $P = 0.02$.

We investigate the origin of various convective flow patterns for low Prandtl numbers ($P = 0.02, 0.005, 0.0002$) from the bifurcation diagrams generated using the low-dimensional model. To generate the bifurcation diagram, we start first with the fixed points of the system. For a given Prandtl number, we compute the fixed points using the Newton-Raphson method for a given r , and these fixed points are subsequently continued using a fixed arc-length based continuation scheme for the neighbouring r values [116]. The stability of the fixed points is ascertained through an eigenvalue analysis of the Jacobian. New branches of the fixed points and limit cycles are born when the eigenvalue(s) become zero (pitchfork) and purely imaginary (Hopf), respectively. This process is continued on the new branch. For aperiodic and chaotic solutions, we resort to numerical integration and report the extremum values of the important modes. We use our own MATLAB code [116] as well as MATCONT package [117] for the analysis.

The phase space of our low-dimensional model is 30-dimensional. Among all the modes, $W_{101}, W_{011}, \theta_{101}$, and θ_{011} are the most important ones. Fixed points of a system and their bifurcations provide important clues about the dynamics of the system. There-

fore, we start our analysis by locating all the fixed points of the 30-mode model with $P = 0.02$. In Fig. 3.4 we plot the numerical values of the fixed points W_{101} and W_{011} for $P = 0.02$ as a function of r . The stable fixed points are shown as solid lines, while the unstable ones are shown as dashed lines. The stable 2D rolls along the x -axis have $W_{101} = 0$, while the rolls along the y -axis have $W_{011} = 0$. The unstable symmetric square (SQ) solutions satisfy $|W_{101}| = |W_{011}|$, while asymmetric square (ASQ) solutions satisfy $|W_{101}| \neq |W_{011}|$. At $r = 1$, the conduction state (cyan curve) becomes unstable and bifurcates into four stable 2D rolls (shown as purple curves) and four unstable SQ patterns (shown as black dashed lines) through a codimension-2 pitchfork bifurcation associated with double zero eigenvalues [118]. With an increase of r , the stable 2D rolls bifurcate into stable ASQ patterns shown as the solid blue lines in Fig. 3.4. These ASQ patterns lose stability at some point through a Hopf bifurcation. With a further increase in r , the unstable branch of the ASQ solutions (dashed blue curves) regains stability through an inverse Hopf bifurcation resulting in stable ASQ solutions (solid blue curves). These stable ASQ solutions subsequently meet the unstable SQ patterns (represented by dashed black curves originating from $r = 1$) in yet another inverse bifurcation, and stable SQ patterns (solid black curves) are formed. These stable SQ patterns subsequently lose stability beyond $r = 1.25$ and complex chaotic attractors are generated. An analysis in this regime is, however, beyond the scope of the present study. This sequence of fixed points remains the same for all finite but small values of P . However, the range of r corresponding to various states changes with P .

We will describe the above-mentioned fixed points and associated time-dependent patterns using a bifurcation diagram in the range of $0.95 \leq r \leq 1.25$. Fig. 3.5 illustrates the bifurcation diagram for $P = 0.02$ where we plot the modulus of $(W_{101})_{extremum}$ as a function of r . At $r = 1$ the conduction state bifurcates to stationary 2D rolls (purple curve) through a codimension-2 pitchfork bifurcation. As described above, unstable stationary SQ patterns (shown as a dashed black curve) with $W_{101} = \pm W_{011}$, are also generated as a result of this bifurcation. As r is increased further, at $r \approx 1.0035$, the stationary 2D rolls bifurcate to ASQ patterns (solid blue curves) through another pitchfork bifurcation. Subsequently, at $r \approx 1.0114$, the ASQ patterns bifurcate to limit cycles

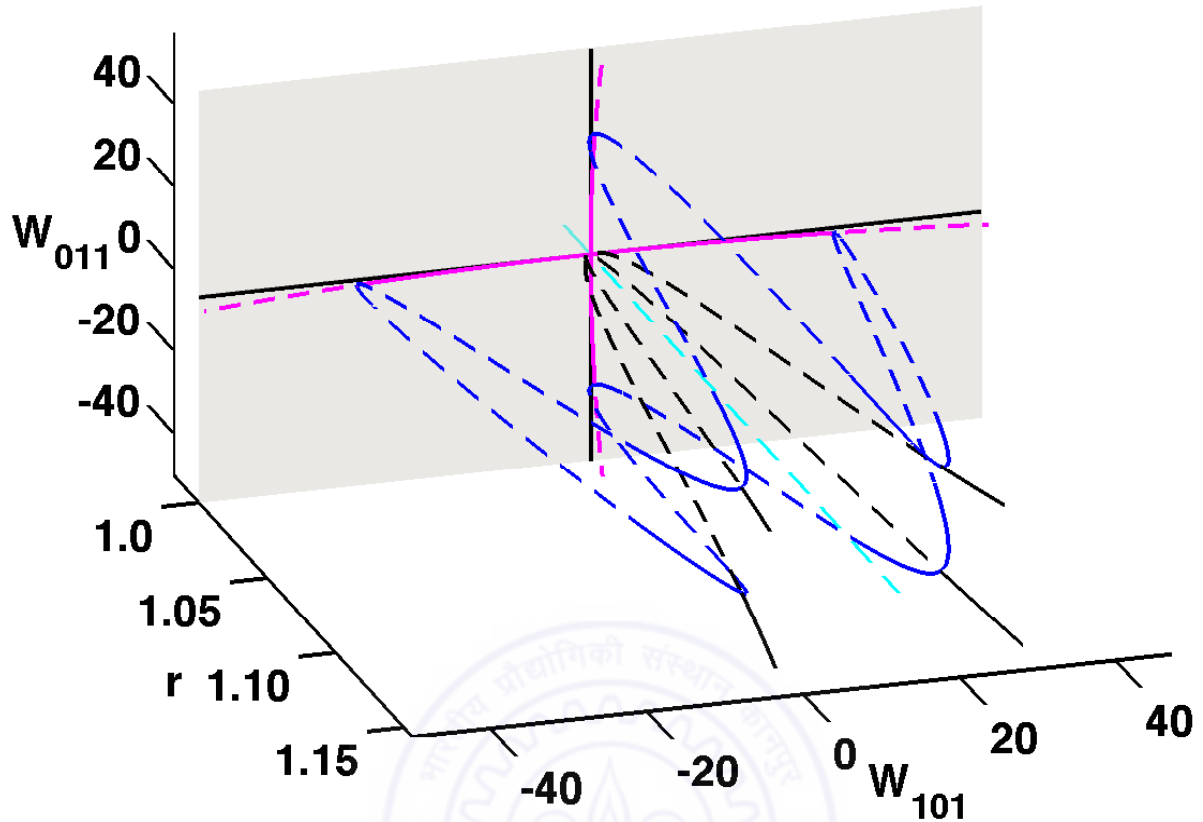


Figure 3.4: For $P = 0.02$, the three-dimensional view of the bifurcation diagram computed from the low-dimensional model exhibiting stable fixed points (solid curves), and unstable fixed points (dashed curves). The purple solid and dashed lines represent the stable and unstable 2D roll solutions respectively. The black, blue, and cyan curves depict stationary squares (SQ), asymmetric stationary squares (ASQ), and the conduction state, respectively. This Figure is taken from [38].

(red curves) through a Hopf bifurcation. These limit cycles represent OASQ patterns. Figs. 3.6((a),(b)) illustrate the projection of two of these stable limit cycles for $r = 1.016$ on the W_{101} - W_{011} plane. Note that the limit cycles are quite close to the axes. The oscillatory patterns corresponding to these limit cycles form standing waves along the roll axis that have been discussed earlier by Thual [12]. The time-period and amplitude of these limit cycles increase as r is increased. At $r \approx 1.0184$, these limit cycles collide with the unstable SQ fixed points (saddles) originating from $r = 1$ and form homoclinic orbits. The phase space projection of the homoclinic orbit on the W_{101} - W_{011} plane is shown in Figs. 3.6((c),(d)).

Beyond $r \approx 1.0184$, there is a smooth transition from homoclinic orbits to regular limit

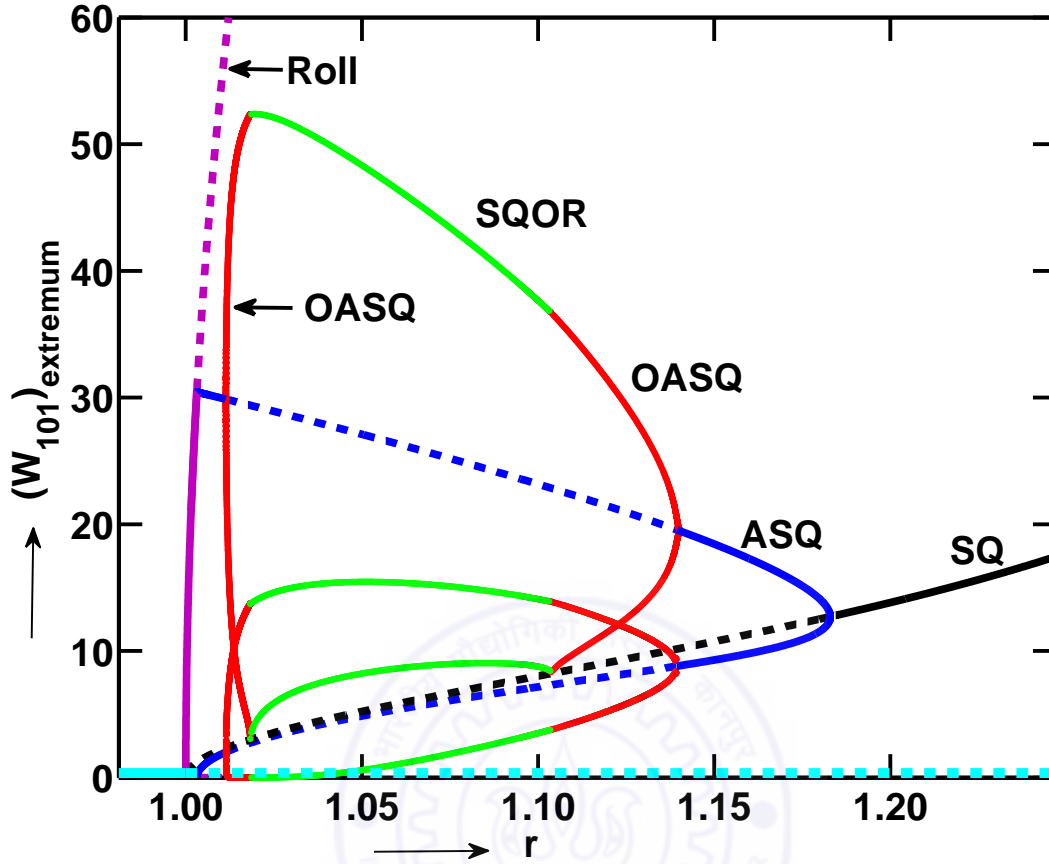


Figure 3.5: Bifurcation diagram of the low-dimensional model for $P = 0.02$ in the range $0.95 \leq r \leq 1.25$. The stable branches corresponding to the conduction state, 2D rolls, SQ, and ASQ are represented by solid cyan, solid purple, solid black, and solid blue curves respectively. The red and green curves depict the extrema of OASQ and SQOR, respectively. The dashed curves represent unstable solutions. This Figure is taken from [38].

cycles corresponding to SQOR, illustrated as green curves in the bifurcation diagram. Figure 3.7 shows the dynamical behaviour of the W_{101} and W_{011} modes in the SQOR regimes. Fig. 3.7(a) shows the time plot of the W_{101} and W_{011} modes in the SQOR regime at $r = 1.034$. We find an alternate but periodic growth and decay of the W_{101} and W_{011} modes. As the energy corresponding to the W_{101} mode grows at a particular instance, the energy corresponding to the W_{011} mode remains close to zero. At some point, the energy corresponding to the W_{101} mode reaches a peak value and then it starts transferring its energy to the W_{011} mode through non-linear interaction. Subsequently, the energy contained in the W_{011} mode grows while energy in the other mode (W_{101}) remains

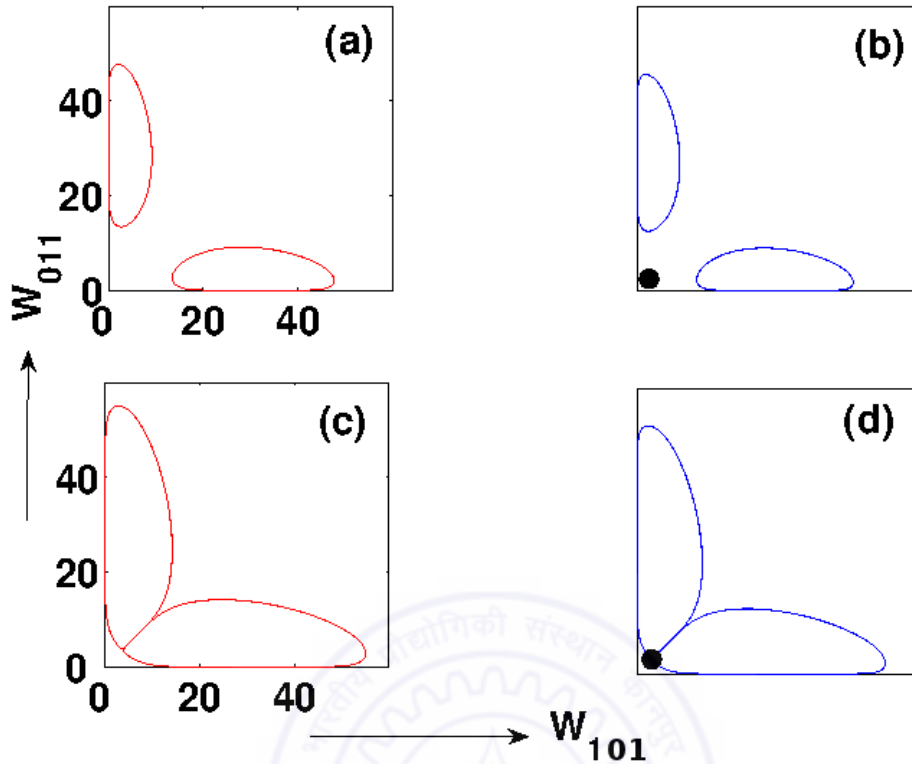


Figure 3.6: Phase space projection on the $W_{101} - W_{011}$ plane is shown to make a comparison between the DNS results and the model results in the OASQ and the SQOR regimes of convection for $P = 0.02$. Red and blue curves show the results obtained from the DNS and the model, respectively. (a) The limit cycle obtained in DNS at $r = 1.016$. (b) The limit cycle obtained in model for $r = 1.0129$. (c) The homoclinic orbit obtained in DNS at $r = 1.027$. (d) The homoclinic orbit at $r = 1.0184$ for model. The black dots shown in (b) and (d) indicate the symmetric square saddle points. Note that the two limit cycles corresponding to OASQ in the homoclinic orbit are very close but they don't touch each other.

close to zero. This alternate growth and decay of the modes occurs in a periodic way. Fig. 3.7(b) illustrates the projection of the SQOR limit cycle on the $W_{101} - W_{011}$ plane at $r = 1.034$. The flow pattern in this regime changes in time from an approximate pure roll in one direction to a symmetric square, and then to an approximate pure roll in the perpendicular direction. The flow pattern corresponding to the SQOR pattern is shown in Fig. 3.2. The limit cycles corresponding to SQOR form another set of homoclinic orbits at $r \approx 1.1034$ after which each of the homoclinic orbits bifurcate into two separate limit cycles. These limit cycles (OASQ, shown as red curves) diminish in size as r is increased until they transform to stable fixed points (ASQ, shown as blue curves) through an inverse Hopf bifurcation. As r is increased further, at $r \approx 1.183$, the stable ASQ branches meet

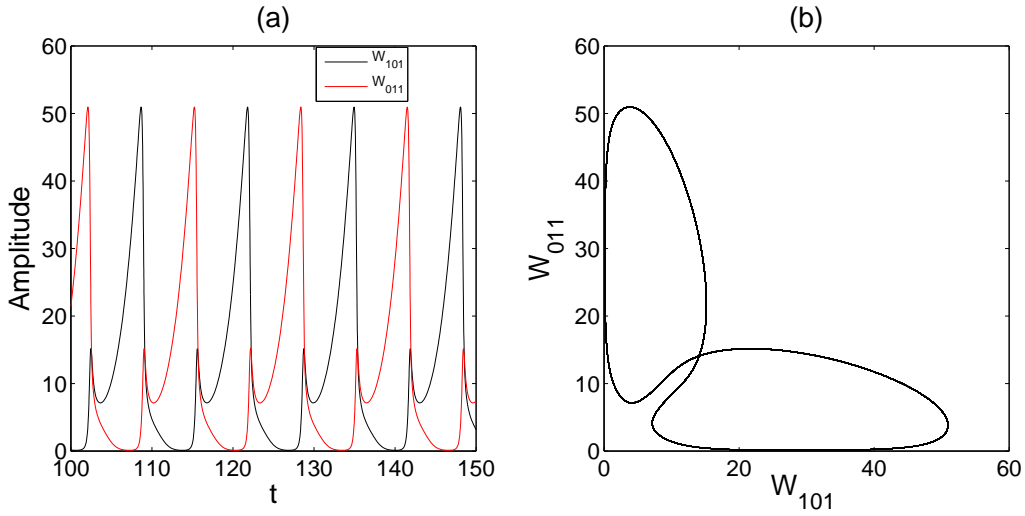


Figure 3.7: (a) The time series of W_{101} and W_{011} . (b) The phase space projection on the W_{101} - W_{011} plane in the SQOR regime for $P = 0.02$ at $r = 1.034$.

the unstable SQ branch (the dashed black curve) resulting in the stabilization of the SQ pattern (solid black curves) as a consequence of an inverse pitchfork bifurcation. Thus, low-dimensional model for $P = 0.02$ exhibits SQ, ASQ, OASQ, and SQOR patterns that are consistent with the earlier numerical investigations for low- P convection of Thual [12].

The DNS and low-dimensional results for $P = 0.02$ are in good agreement with each other (see also Table 3.2). In the following discussion we will consider the bifurcation diagrams for lower Prandtl numbers ($P = 0.005, 0.002, \&0.0002$) for which we observe the presence of several chaotic attractors near the onset of convection.

The bifurcation diagram for $P = 0.005$, shown in Fig. 3.8, is similar to the corresponding figure for $P = 0.02$ with a major difference being that for $P = 0.005$, the chaotic attractors appear near the onset in the band of $r = 1.000685 - 1.0068$. The chaotic attractors have three different forms: *Ch1*, *Ch2*, and *Ch3* as shown in the inset of Fig. 3.8 as (i), (ii), and (iii), respectively. The phase space projection for these three solutions ((iii),(ii) and (i)) are depicted in Figs. 3.9((b,c,d)) for $r = 1.0023$, $r = 1.0053$, and $r = 1.0064$, respectively. In the following, we will explore the origin of these chaotic

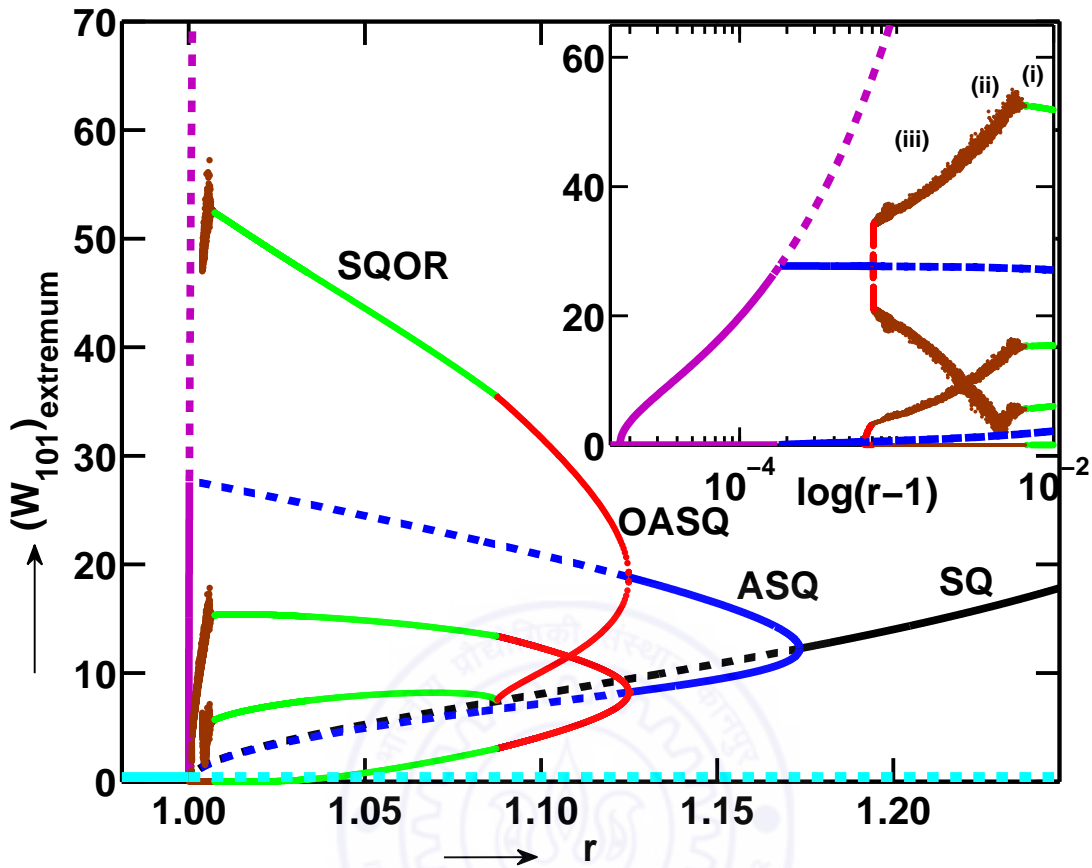


Figure 3.8: Bifurcation diagram of the low-dimensional model for $P = 0.005$ in the range $0.95 \leq r \leq 1.25$. The colour convention is the same as that for $P = 0.02$ (Fig. 3.5). The chaotic attractors are shown in brown. A zoomed view of the bifurcation diagram for the chaotic regime is shown in the inset where the x -axis is chosen as $\log(r - 1)$ to highlight the behaviour near $r = 1$. The three attractors $Ch1$, $Ch2$ and $Ch3$ are shown as (i), (ii), and (iii), respectively. This Figure is taken from [38].

attractors.

As we increase r from 1, we observe 2D straight rolls, ASQ, and OASQ just like in the $P = 0.02$ case, however, at lower r values (see Table 4.1). The phase space projection on the W_{101} - W_{011} plane of two of the limit cycles corresponding to OASQ are shown in Fig. 3.9(a). Subsequently, these limit cycles appear to approach their basin boundary (the horizontal axis of the figure), and the system becomes chaotic. This phenomenon is due to a “gluing bifurcation” [119], and it could be related to the “attractor merging crisis” [120]. The gluing bifurcation and the attractor merging crisis refer to the phenomena wherein two or more distinct attractors simultaneously hit their common basin boundaries to give

Flow patterns	r (Model)	r (DNS)
Roll	1 - 1.0032	1 - 1.0038
ASQ	1.0033 - 1.0122	1.0039 - 1.0114
OASQ	1.0123 - 1.0183	1.0115 - 1.0236
SQOR	1.0184 - 1.1027	1.0237 - 1.0874
OASQ	1.1028 - 1.1402	1.0875 - 1.1407
ASQ	1.1403 - 1.1830	1.1408 - 1.2015
SQ	1.1831 - 1.4859	1.2015 - 1.2528

Table 3.2: Range of the reduced Rayleigh number r corresponding to various flow patterns observed in the 30-mode model and the DNS for $P = 0.02$. Here SQ, ASQ, OASQ, and SQOR represent stationary squares, stationary asymmetric squares, oscillatory asymmetric squares, and relaxation oscillation of squares, respectively.

rise to a single large attractor. The former is used when the pre-bifurcation attractors are regular, e.g., limit cycles, while the latter involves chaotic attractors. The resulting chaotic attractor, whose phase space projection is shown in Fig. 3.9(b) is labelled as the *Ch3*. As r is increased further, the various *Ch3* attractors merge together in yet another crisis to form a single large chaotic attractor *Ch2*. At a larger r value, the *Ch2* attractor breaks into four separate chaotic attractors, each labelled as *Ch1*. Phase space projections of the chaotic attractors *Ch2* and *Ch1* for $P = 0.005$ are shown in Figs. 3.9(c) and 3.9(d) respectively. The *Ch1* chaotic attractors become regular for $r \geq 1.0068$ giving rise to the SQOR limit cycles. The subsequent patterns and the bifurcation diagram are the same as those for $P = 0.02$. Note that the *Ch1* chaotic attractors are generated as a result of “homoclinic chaos”, where the stable and unstable manifolds of a saddle intersect each other rather than merge smoothly to form a homoclinic orbit. Note that for $P = 0.02$, the window of chaos (*Ch1* to *Ch3*) is absent as the homoclinic intersection point of the left OASQ limit cycle precedes the gluing bifurcation point. The patterns and chaotic attractors observed in the low-dimensional model for $P = 0.005$ are also observed in the DNS. Phase space projections of the chaotic attractors (*Ch3* and *Ch1*) obtained in the DNS are shown in Fig. 3.10(a) (for $r = 1.0023$) and Fig. 3.10(b) (for $r = 1.0068$), respectively. The chaotic attractors obtained from the DNS data are quite thin. However an enlarged view of the attractors in the insets show that the attractors are chaotic.

When we lower the value of the Prandtl number even further from $P = 0.005$, the

P	r_p	r_t	ω
0.02	1.0035	1.01139	1.15×10^{-3}
0.005	1.000179	1.000683	2.9×10^{-5}
0.002	1.000042	1.00012	1.15×10^{-5}
0.0002	$1+2.5 \times 10^{-7}$	1.000018	1.15×10^{-7}

Table 3.3: Table depicting the reduced Rayleigh numbers r_p at which the 2D rolls bifurcate to ASQ, r_t where the ASQ patterns bifurcate to limit cycles, and the frequency ω of the limit cycle at the Hopf bifurcation point. These values are computed for Prandtl numbers $P = 0.02, 0.005, 0.002$, and 0.0002 . This Table is taken from [38].

stationary 2D rolls and the associated ASQ patterns occur even nearer to $r = 1$ as evident from the entries of Table 4.1. It can be noted from Fig. 3.11 that the windows of the 2D rolls and ASQ for $P = 0.0002$ are very small. The 2D rolls and ASQ occur for $1 < r < 1 + 2.5 \times 10^{-7}$ and $1 + 2.5 \times 10^{-7} < r < 1 + 1.8 \times 10^{-7}$, respectively. Consequently, it would be very difficult to observe these 2D rolls and the related ASQ patterns in experiments and in the DNS; a small experimental or numerical noise will be sufficient to push the system out of this narrow ordered region to chaos *Ch1-Ch3*. Later on in this chapter we will show that for zero-P convection chaotic attractors (*Ch3-Ch1*) appear at the onset itself.

It can be seen from Table 4.1 that the branch points corresponding to ASQ (r_p) and OASQ (r_t) asymptotically approach $r = 1$ as $P \rightarrow 0$. In Table 4.1, we also list the imaginary part of the eigenvalue (ω) of the stability matrix at the Hopf bifurcation ($r = r_t$). We observe that $r_p - 1$, $r_t - 1$, and ω appear to vary approximately as P^2 with prefactors around 10, 30, and 3 respectively. The P^2 dependence is consistent with the theoretical predictions of Busse [13] that $r_t - 1 \geq 0.310P^2$ for free-slip boundary conditions. However, the multiplying factor of Busse and our model differ by an order of magnitude. Also, Busse and Bolton [15] predict an absence of stable 2D rolls for $P < P_c = 0.543$. Our analysis, however, indicates stable 2D rolls for non-zero P , with the range of $r_p - 1$ decreasing rapidly with the lowering of P . Earlier, Krishnamurti [29] had found stable 2D rolls for mercury ($P = 0.025$) near the onset ($R \approx (2.3 \pm 0.1) \times 10^3$) in her experiments with no-slip boundary conditions, thus indicating that the P_c predicted by Busse and Bolton [15] is an overestimate. Regarding ω , Busse [13] predicts that ω (in

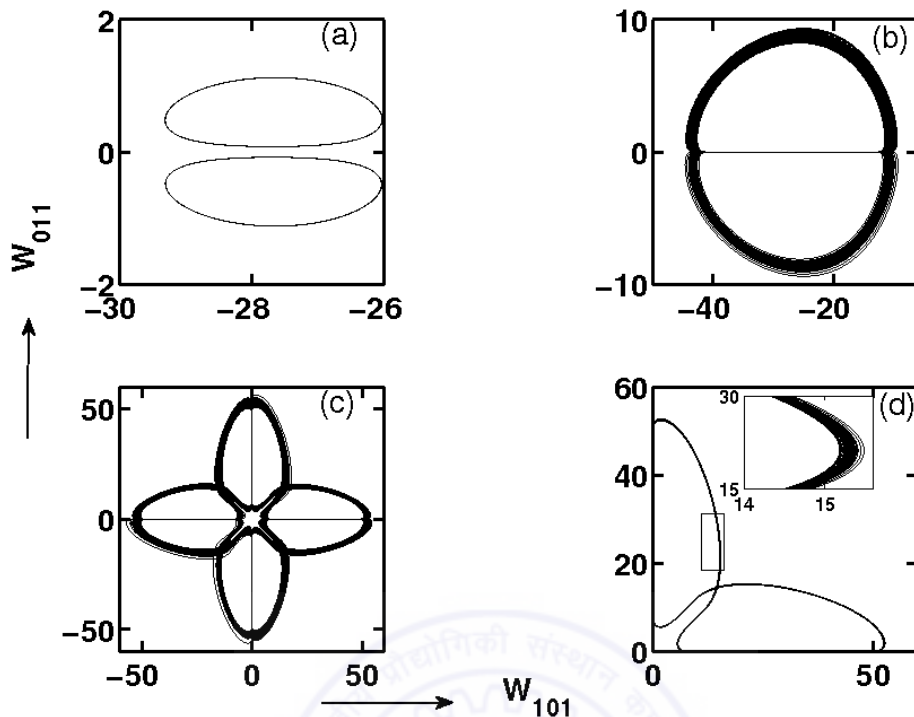


Figure 3.9: Phase space projections of the attractors on the W_{101} - W_{011} plane obtained from the low-dimensional model for $P = 0.005$ near $r = 1$: (a) two of the limit cycles at $r = 1.0006844$; (b) the chaotic attractor *Ch3* at $r = 1.0023$; (c) the chaotic attractor *Ch2* at $r = 1.0053$; (d) the chaotic attractor *Ch1* at $r = 1.0064$, with the inset depicting the chaotic nature of the attractor. This Figure is taken from [38].

units of ν/d^2) is independent of the Prandtl number, which is in contrast to our finding that $\omega \sim P^2$ near the onset of convection. In a related work on convection, Mercader *et al.* [121] have shown that the relationship between ω and P depends critically on the aspect ratio and they have reported both linear and quadratic dependence. Recently, Pal *et al.* [115] found that ω is independent of the Prandtl number when oscillatory modes like Z_{010} , etc., are included in the model.

We could not go below $P = 0.0002$ in the DNS and even in the low-dimensional model because the computations take a lot of time. Thual [12] showed for the first time that the convection patterns near the onset for $P \rightarrow 0$ are very similar to the pattern near $P = 0$. In the next section, we present our bifurcation study for $P = 0$ convection and establish the similarity between the $P \rightarrow 0$ and $P = 0$ cases.

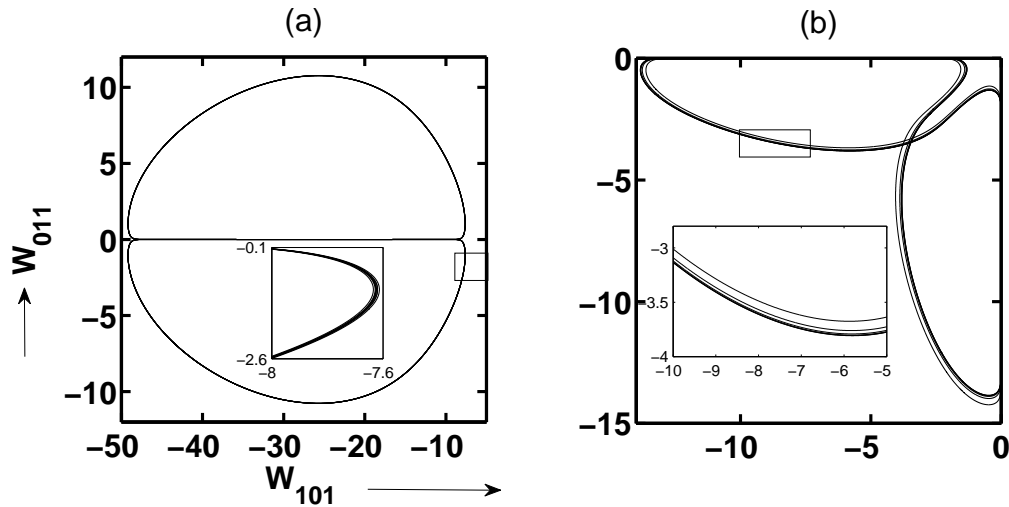


Figure 3.10: Phase space projections of the chaotic attractors on the W_{101} - W_{011} plane obtained from DNS with $P = 0.005$: (a) *Ch3* for $r = 1.0023$; (b) *Ch1* for $r = 1.0068$. The insets show an enlarged view of the boxed region. This Figure is taken from [38].

3.3 Zero-P Convection

In this section we present the numerical simulations and bifurcation analysis of zero-P convection by Pal *et al.* [43]. This analysis was performed along similar lines as described for low-P convection. Spiegel [5] and Thual [12] derived the equations for the zero-P limit under the Boussinesq limit. The dynamical equations related to zero-Prandtl number convection are Eqs. (1.26) - (1.29) described in Chapter 1. We consider perfectly conducting and free-slip boundary conditions at the top and bottom plates, and periodic boundary conditions along the horizontal directions.

We performed around 100 DNS runs for zero-P convection (Eqs. (1.26) - (1.29)) using a pseudo-spectral code for various r values ranging from $r = 0.95$ - 1.5 on a 64^3 box. The aspect ratio of the simulation was $2\sqrt{2} : 2\sqrt{2} : 1$. For zero-P DNS, Pal *et al.* [43] observed stationary squares (SQ), stationary asymmetric squares (ASQ), oscillatory asymmetric squares (OASQ), relaxation oscillations with squares (SQOR), and chaos as we observe

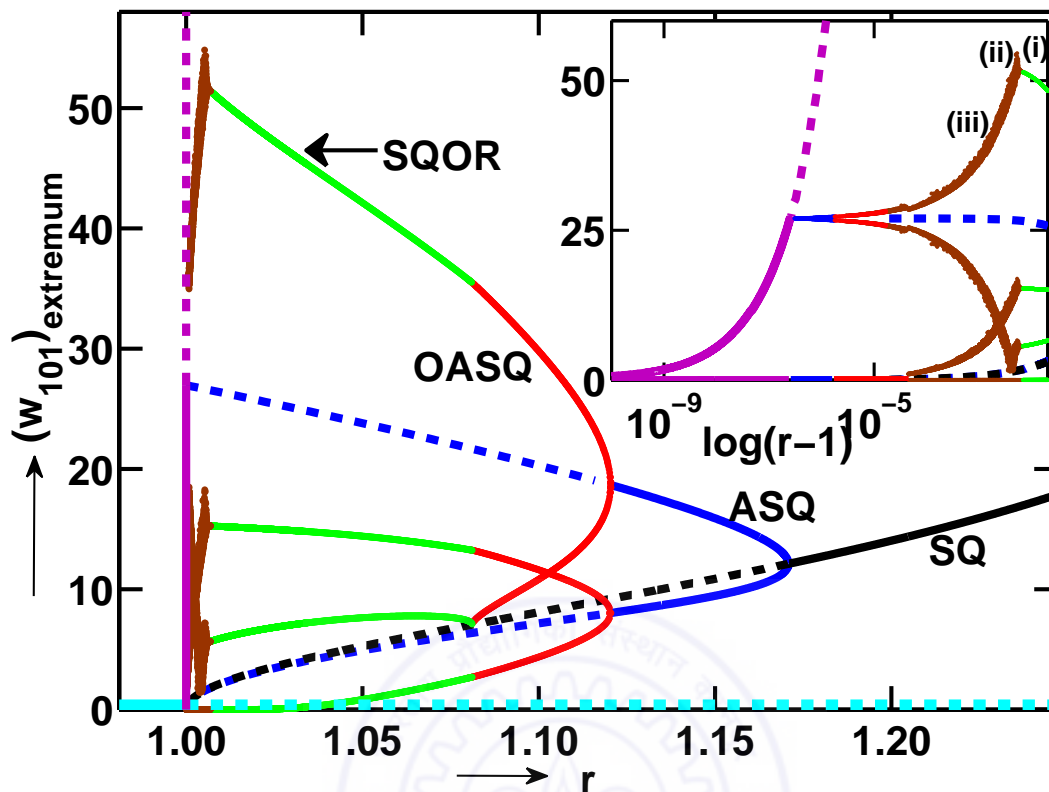


Figure 3.11: Bifurcation diagram of the low-dimensional model for $P = 0.0002$ in the range $0.95 \leq r \leq 1.25$. The colour convention is same as that for $P = 0.005$ (Fig. 3.8). This Figure is taken from [38].

for low-P convection. In the next subsection we present the detailed bifurcation analysis for zero-P convection observed by Pal *et al.* [43].

3.3.1 Low-dimensional model

For the bifurcation analysis, Pal *et al.* [43] constructed a low-dimensional model using the energetic modes of the above-mentioned simulation in the range of $r = 1 - 1.4$ along similar lines as we have used for low-Prandtl number convection. Pal *et al.* [43] picked 9 large-scale vertical velocity modes (real Fourier amplitudes): W_{101} , W_{011} , W_{202} , W_{022} , W_{103} , W_{013} , W_{112} , W_{121} , and W_{211} ; and 4 large-scale vertical vorticity modes (real Fourier amplitudes): Z_{110} , Z_{112} , Z_{121} , and Z_{211} . Note that for zero-Prandtl number convection, the temperature modes becomes enslaved to the vertical velocity. Hence they can be calculated from the vertical velocity modes. The cumulative energy contained in these

modes ranges from 85% to 98% of the total energy of the DNS, and each of these modes has 1% or more of the total energy.

The vertical velocity field (v_3) and the vertical vorticity field (ω_3) of the low-dimensional model are

$$\begin{aligned}
v_3(x, y, z, t) = & W_{101}(t) \cos(kx) \sin(\pi z) + W_{011}(t) \cos(ky) \sin(\pi z) \\
& + W_{112}(t) \cos(kx) \cos(ky) \sin(2\pi z) + W_{211}(t) \cos(2kx) \cos(ky) \sin(\pi z) \\
& + W_{121}(t) \cos(kx) \cos(2ky) \sin(\pi z) + W_{202}(t) \cos(2kx) \sin(2\pi z) \\
& + W_{022}(t) \cos(2ky) \sin(2\pi z) + W_{103}(t) \cos(kx) \sin(3\pi z) \\
& + W_{013}(t) \cos(ky) \sin(3\pi z), \tag{3.4}
\end{aligned}$$

$$\begin{aligned}
\omega_3(x, y, z, t) = & Z_{110}(t) \sin(kx) \sin(ky) + Z_{112}(t) \sin(kx) \sin(ky) \cos(2\pi z) \\
& + Z_{211}(t) \sin(2kx) \sin(ky) \cos(\pi z) \\
& + Z_{121}(t) \sin(kx) \sin(2ky) \cos(\pi z). \tag{3.5}
\end{aligned}$$

Pal *et al.* [43] derived the model equations using the Galerkin projection of Eqs. (1.26) - (1.27) on the subspace of these modes. This results in thirteen coupled ordinary differential equations for the above variables. The low-dimensional model captures all the flow patterns of the DNS mentioned above. The range of r for these patterns for the model and the DNS are shown in Table 3.4, and they are reasonably close to each other. Interestingly, the stable steady values of the modes W_{101} , W_{011} , W_{112} , W_{121} , and W_{211} for SQ and ASQ patterns match with the corresponding DNS values within 10%.

Flow patterns	r (Model)	r (DNS)
Chaotic	1 - 1.0045	1 - 1.0048
SQOR	1.0045 - 1.0175	1.0048 - 1.0708
OASQ	1.0175 - 1.0703	1.0709 - 1.1315
ASQ	1.0703 - 1.2201	1.1316 - 1.2005
SQ	1.2201 - 1.4373	1.2006 - 1.4297

Table 3.4: The range of the reduced Rayleigh number r corresponding to various flow patterns observed in the model and the DNS for $P = 0$. Here SQ, ASQ, OASQ, and SQOR represent stationary squares, stationary asymmetric squares, oscillatory asymmetric squares, and relaxation oscillation of squares, respectively.

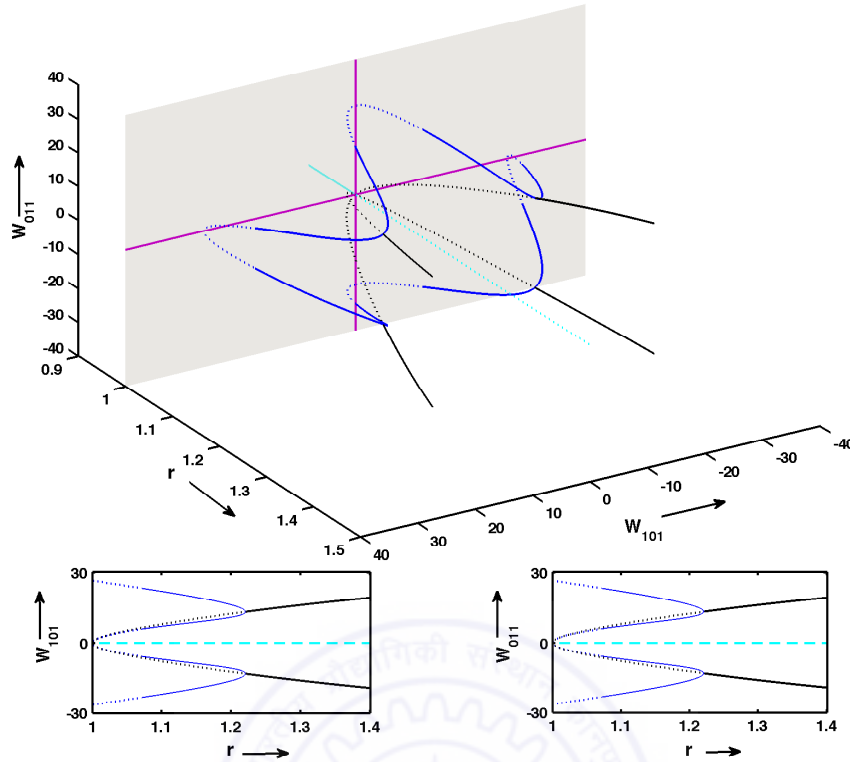


Figure 3.12: Three-dimensional view of the bifurcation diagram showing the fixed points with solid and dashed curves representing the stable and unstable fixed points, respectively. Black, blue, and cyan curves represent stationary squares (SQ), asymmetric stationary squares (ASQ), and the conduction state, respectively. All the points on the axis (purple lines) are 2D roll solutions. Below the 3D diagram, we plot the values of W_{101} and W_{011} vs. r . These plots indicate xy symmetry in the system. This Figure is taken from [43].

In the following, we present the bifurcation analysis of Pal *et al.* [43] for zero-Prandtl number convection and compare it with low-Prandtl number convection. Fig. 3.12 shows the plot of the numerical values of the fixed points W_{101} and W_{011} for $P = 0$ as a function of r . For $r < 1$, the origin is the unique stable fixed point corresponding to the pure conduction state. There is a double zero eigenvalue at $r = 1$ [118], and all the fixed points (13 in number) arising from $r = 1$ are unstable for $r > 1$ in contrast with the low- P convection where we observe a fixed roll solution above the onset. Fixed points for zero- P are shown as dotted lines in Fig. 3.12. Four of these branches of fixed points bifurcate from the origin; these fixed points satisfy $|W_{101}| = |W_{011}|$. The other 8 branches of unstable fixed points emerge from non-zero W_{101} or W_{011} , and they obey $|W_{101}| \neq |W_{011}|$ (see Fig. 3.12). With an increase of r , these 8 branches become stable and merge with

the 4 branches that originate from the origin. For a clear visualization, the bottom of Fig. 3.12 contains projections only on the individual modes.

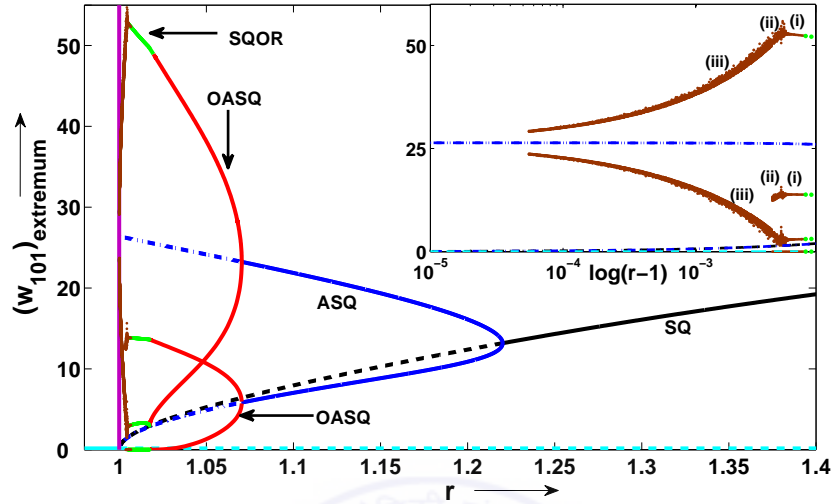


Figure 3.13: Bifurcation diagram of the model for $0.95 \leq r \leq 1.4$. The stable branches corresponding to stationary squares (SQ) and stationary asymmetric squares (ASQ) are represented by solid black and solid blue lines, respectively. Red, green, and brown curves represent the extrema of oscillatory asymmetric squares (OASQ), relaxation oscillation of squares (SQOR), and chaotic solutions respectively. A zoomed view of the bifurcation diagram for the chaotic regime is shown in the inset. In the inset, the x -axis is chosen as $\log(r-1)$ to highlight the behaviour near $r=1$. Branches corresponding to the unstable fixed points are represented by dashed lines. The cyan line represents the conduction state. This Figure is taken from [43].

The bifurcation diagram of zero-Prandtl number convection in the range $1 \leq r \leq 1.4$ is shown in Fig. 3.13. For $P=0$, chaotic solutions are observed at the onset of convection itself, i.e., just above $r=1$. The nature of the chaotic attractors denoted as (i), (ii) and (iii) in the inset of Fig. 3.13 are the same as that observed for low-Prandtl number convection. The phase space projection for these three attractors are depicted in Fig. 3.14 for $r=1.0041$, 1.0038 and 1.0030 for the 13-mode model, and for $r=1.0045$, 1.0032 , and 1.0023 in the DNS for zero-P convection. The bifurcation scenario for low-P and zero-P from SQ to SQOR for the larger r values are topologically equivalent (see Fig. 3.13). We observe two major differences between the bifurcation diagrams of zero-P convection and low-P convection: (a) no chaos for $P \geq 0.02$ near the onset; and (b) existence of stable 2D rolls and associated ASQ and OASQ patterns for $P \neq 0$ near the onset. For $P=0.02$, we find only stationary and time-periodic solutions near the onset which is in agreement

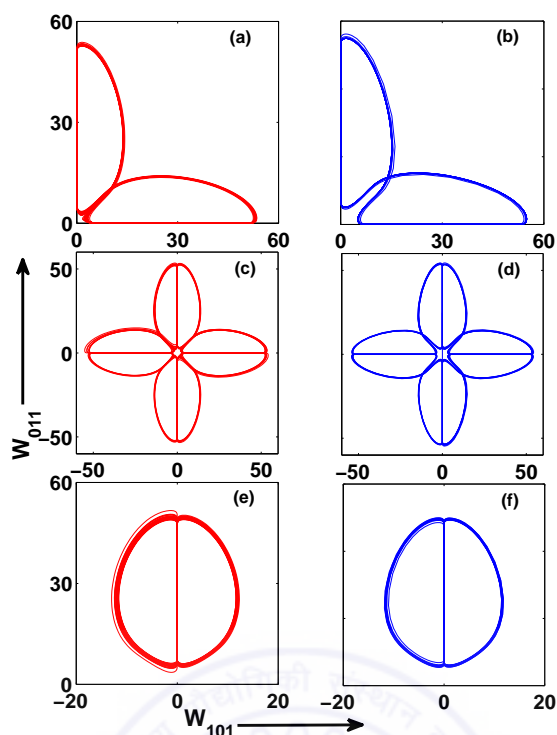


Figure 3.14: The three different chaotic solutions observed near $r = 1$: Ch1 at $r = 1.0041$ for the model (a) and at $r = 1.0045$ in DNS (b); Ch2 at $r = 1.0038$ for the model (c) and at $r = 1.0030$ in DNS (d); Ch3 at $r = 1.0030$ for the model (e) and at $r = 1.0023$ in DNS (f). These solutions belong to (i), (ii), and (iii) regimes in the bifurcation diagram (Fig. 3.13). This Figure is taken from [43].

with the results of Meneguzzi *et al.* [32] for $P = 0.025$ and Thual [12] for $P = 0.02$ and 0.2 . However, for $P \leq 0.005$, we observe chaotic attractors $Ch1$, $Ch2$, and $Ch3$ between OASQ (closer to $r = 1$) and SQOR. The stationary 2D rolls and associated ASQ and OASQ patterns are observed in a narrow window between the conduction state and the chaotic states.

Thus, our study indicates that zero- P convection is an appropriate limiting case of low- P convection in terms of bifurcations near the onset. For practical purposes, the bifurcation diagram for low- P convection is topologically equivalent to that of zero- P convection.

3.4 Conclusion

In this chapter, we presented a detailed bifurcation structure and associated flow patterns for low-Prandtl number ($P = 0.0002, 0.002, 0.005$, and 0.02) and zero-Prandtl number ($P = 0$) Rayleigh-Bénard convection near its onset. We used both direct numerical simulations and a low-dimensional models for this study. We proposed a 30-mode model for low-Prandtl number convection. The results of the low-dimensional models are in good agreement with those of the DNS since the model is derived using DNS by choosing most of the relevant modes. We observed that low-Prandtl number and zero-Prandtl number convection exhibit patterns, namely, squares, asymmetric squares, oscillating asymmetric squares, and relaxation oscillations. We observed that the bifurcation diagram for low-P convection is very similar to that of zero-P convection, except near the onset of convection where 2D stationary rolls, and stationary and oscillatory asymmetric squares are observed for nonzero Prandtl numbers. The range of Rayleigh numbers for which 2D rolls and associated ASQ and OASQ are observed shrinks rapidly ($\sim P^2$) as P is decreased. This result is in qualitative agreement with the results of Busse [13]. For $P \leq 0.0002$, the range of reduced Rayleigh numbers for which the stationary 2D rolls could be observed is too narrow ($< 1 + 10^{-7}$) to be observed in experiments or in DNS. Our results predict the critical Prandtl number P_c , i.e., the Prandtl number below which the stable roll solution does not exist, is $P \sim 0.0002$, which is much lower than that predicted by Busse and Bolton [15].

Our bifurcation analysis provides very useful insights into the origin of patterns and chaos for low-P and zero-P convection. Furthermore, our comparative study of low-P convection with that of zero-P convection of Pal *et al.* [43] shows how the limiting behaviour of zero-P convection is obtained as P approaches zero. We also show how the chaos near onset disappears as the Prandtl number is increased to $P = 0.02$.

Chapter 4

Energy spectra and fluxes for Rayleigh-Bénard convection

4.1 Introduction

In this chapter, we present a numerical study of the nature of the velocity and temperature spectra in the inertial range of convective turbulence for a wide range of Prandtl numbers: zero-Prandtl number ($P = 0$), low-Prandtl number ($P = 0.02$, and 0.2), moderate Prandtl number ($P = 1$), and high-Prandtl number ($P = 6.8$). This work is published in *Phys. Rev. E* [122]. The previous works related to the spectra and fluxes have been described in Section 1.3.2 of Chapter 1.

The presence of a buoyancy term makes the energy transfer in the inertial range of convective turbulence quite interesting and complicated [45, 46]. For turbulent Rayleigh-Bénard convection, Procaccia and Zeitak [49], L'vov [50], and Falkovich and L'vov [51] predicted that the kinetic energy spectrum scales as $E^u(k) \sim k^{-11/5}$ and the temperature (entropy) spectrum as $E^\theta(k) \sim k^{-7/5}$ [Bolgiano-Obukhov (BO) scaling] for scales above the Bolgiano length ($l_B < l < L$) in which buoyancy is the dominant force. For $l_d < l < l_B$, the inertia term dominates over the buoyancy force, and consequently, the kinetic and entropy spectra follow the Kolmogorov-Obukhov (KO) scaling, i.e., $E^u(k) \sim k^{-5/3}$, and $E^\theta(k) \sim k^{-5/3}$. Here, k is the wavenumber, L is the characteristic length scale, l_B is the buoyancy length scale, and l_d is the Kolmogorov length scale. In the BO regime, the

entropy flux (Π^θ) is constant, while the kinetic energy flux (Π^u) varies as $k^{-4/5}$. However, in KO regime, both the entropy and kinetic energy flux remain constant.

It was shown that for $P < 1$ (low-P fluid), l_B is of the order of the characteristic scale L of the system, and hence, only KO scaling is expected in the inertial range [46, 52, 53, 69]. However, for $P > 1$ (high-P fluid), l_B is smaller than the characteristic length scale, which gives rise to the co-existence of the two scalings in the inertial range [49, 52, 53, 69]. A series of experiments [53, 60, 61, 62, 63, 64, 65, 67, 68, 69] and numerical simulations [57, 58, 70, 71, 75] have been performed to test the above phenomenologies. Many experiments [53, 66, 67] performed in the range of $P \geq 0.7$ appear to support BO scaling, while experiments [53, 69] performed in the range of $P \leq 0.7$ tend to support KO scaling. Note, however, that Mashiko *et al.* [60] report only the presence of BO scaling for mercury ($P = 0.02$). Niemela *et al.* [68] reported the co-existence of both the scalings (BO and KO) in the inertial range of the temperature spectra for gaseous helium ($P \sim 0.7$) contained in a cylindrical container of aspect ratio one. A detailed review of these works are presented in Chapter 1 (see Sec. 1.3.2).

In this chapter, we compute the energy spectra and cascade rates for the velocity and temperature fields using the pseudo-spectral method on 512^3 grids with free-slip boundary conditions. Our computations include the zero-Prandtl number (zero-P), low-P, and large-P convection regimes ($P = 0, 0.02, 0.2, 1, \text{ and } 6.8$), hence, we have a reasonable number of numerical runs to test the convective turbulence phenomenology. We also construct phenomenological arguments to understand the zero-P and low-P numerical results. We find that for zero-P and low-P convection, the spectra and the fluxes of the velocity and temperature fields in the inertial range support KO scaling. However, for large-Prandtl-number ($P = 6.8$) convection, we observe only the presence of BO scaling in the inertial range.

In the following sections, we present our numerical results pertaining to the calculation of the spectra and the fluxes of the velocity and temperature fields for zero-P, low-P and high-P convection.

4.2 Governing equations

We numerically solve the non-dimensionalized Rayleigh-Bénard equations under the Boussinesq approximation [12]:

$$\frac{\partial \mathbf{u}}{\partial t} + (\mathbf{u} \cdot \nabla) \mathbf{u} = -\nabla \sigma + P \theta \hat{z} + \sqrt{\frac{P}{R}} \nabla^2 \mathbf{u}, \quad (4.1)$$

$$P \left(\frac{\partial \theta}{\partial t} + (\mathbf{u} \cdot \nabla) \theta \right) = u_3 + \sqrt{\frac{P}{R}} \nabla^2 \theta, \quad (4.2)$$

$$\nabla \cdot \mathbf{u} = 0, \quad (4.3)$$

where $\mathbf{u} = (u_1, u_2, u_3)$ is the velocity field, θ is the perturbation in the temperature field from the mean temperature, σ is the deviation of the pressure from the conduction state, $R = \alpha g(\Delta T) d^3 / \nu \kappa$ is the Rayleigh number, $P = \nu / \kappa$ is the Prandtl number, and \hat{z} is the buoyancy direction. Here, ν and κ are the kinematic viscosity and thermal diffusivity, respectively, d is the vertical height of the container, and ΔT is the temperature difference between the plates. For the non-dimensionalization we have used d as the length scale, $\sqrt{\alpha(\Delta T)gd}$ as the velocity scale, and $\nu(\Delta T)/\kappa$ as the temperature scale. For large- P convection, the temperature scale is taken as ΔT , and the governing equations are altered accordingly.

Zero-Prandtl number (zero- P) convection is the limiting case of low- P convection. The corresponding dimensionless equations for zero- P convection are Eqs. (1.16) - (1.18) as described in Chapter 1. Note that for zero-Prandtl number convection, we use d as the length scale, ν/d as the velocity scale, and $\nu(\Delta T)/\kappa$ as the temperature scale.

Boundary conditions of the system strongly affect the properties of the convective flow [55, 71]. We employ free-slip and conducting boundary conditions on the horizontal plates and periodic boundary conditions are applied along the horizontal directions. The viscous boundary layer is weak under the free-slip boundary conditions, however thermal boundary layers are present due to the conducting boundary conditions. Hence, our simulation results are expected to resemble the bulk flow due to the absence of the viscous boundary layer.

The energy spectra of the velocity field ($E^u(k)$), and the temperature field ($E^\theta(k)$) are

calculated, respectively, using the expressions

$$E^u(k) = \sum_{k \leq k' < k+1} \frac{1}{2} |u(\mathbf{k}')|^2, \quad (4.4)$$

$$E^\theta(k) = \sum_{k \leq k' < k+1} \frac{1}{2} |\theta(\mathbf{k}')|^2. \quad (4.5)$$

Here, the summation is being performed over all the Fourier modes in the shell $[k, k+1)$. We will compute these spectra numerically at the steady state. Note that the magnitude of the wavevectors in the Fourier space is

$$k = \left((i_x \pi / \sqrt{2})^2 + (i_y \pi / \sqrt{2})^2 + (i_z \pi)^2 \right)^{1/2}. \quad (4.6)$$

Here, we use the fact that the aspect ratio of the box is $2\sqrt{2}$ [87].

The energy flux is a measure of the non-linear energy transfers in turbulence [123, 124, 125]. The energy flux for a given wavenumber sphere is the total energy transferred from the modes within the sphere to the modes outside the sphere. The energy flux for fluid and magneto-hydrodynamic turbulence have been studied in great detail [124]. However, there are only a very few works on the flux computations in convective turbulence [126, 57, 58]. Toh and Suzuki [126] defined the kinetic energy flux $\Pi^u(k_0)$, and the entropy flux $\Pi^\theta(k_0)$ based on Kraichnan formalism [125] as

$$\begin{aligned} \Pi^u(k_0) &= \frac{1}{2} \sum_{k > k_0} \sum_{p, q < k_0} \delta_{\mathbf{k}, \mathbf{p} + \mathbf{q}} i \frac{k_l k_m}{k_n} (1 - \delta_{l,n}) \\ &\quad \times u_l^*(\mathbf{k}) u_m(\mathbf{p}) u_n(\mathbf{q}), \end{aligned} \quad (4.7)$$

$$\begin{aligned} \Pi^\theta(k_0) &= \frac{1}{2} \sum_{k > k_0} \sum_{p, q < k_0} \delta_{\mathbf{k}, \mathbf{p} + \mathbf{q}} i (\mathbf{k} \cdot \mathbf{u}(\mathbf{q})) \\ &\quad \times (\theta^*(\mathbf{k}) \theta(\mathbf{p})). \end{aligned} \quad (4.8)$$

These quantities represent the net cascade of $|\theta|^2/2$ and $|\mathbf{u}|^2/2$, respectively, from the modes within the wavenumber sphere of radius k_0 to the modes outside the sphere.

The energy fluxes defined above can also be defined quite conveniently using the “mode-to-mode energy transfers” formalism discussed by Verma [124]. According to this

formalism, the kinetic energy flux and the entropy flux are respectively,

$$\Pi^u(k_0) = \sum_{k \geq k_0} \sum_{p < k_0} \delta_{\mathbf{k}, \mathbf{p} + \mathbf{q}} \Im([\mathbf{k} \cdot \mathbf{u}(\mathbf{q})][\mathbf{u}^*(\mathbf{k}) \cdot \mathbf{u}(\mathbf{p})]), \quad (4.9)$$

$$\Pi^\theta(k_0) = \sum_{k \geq k_0} \sum_{p < k_0} \delta_{\mathbf{k}, \mathbf{p} + \mathbf{q}} \Im([\mathbf{k} \cdot \mathbf{u}(\mathbf{q})][\theta^*(\mathbf{k})\theta(\mathbf{p})]), \quad (4.10)$$

where \Im represents the imaginary part of the argument. We compute the spectra and fluxes of the velocity and temperature fields using numerical simulations [124]. These results will be described in the next section.

4.3 Numerical simulations and results

As described in the previous section, the dynamical equations of RBC are Eqs. (4.1) - (4.3) for low-P convection and Eqs. (1.16) - (1.18) for zero-P convection. The equations for large-P convection are similar. We solve these equations numerically using a pseudo-spectral method under free-slip boundary conditions for the horizontal plates, and periodic boundary conditions along the horizontal directions. The details of the numerical schemes used to solve the dynamical equations of RBC in a 3D box have been discussed in Chapter 2.

For the random initial input, an initial form of the spectra is chosen and the energy is assumed to be equally distributed on the thin shells. The unidirectional initial energy and entropy spectra for the initial conditions are both of the form

$$E(k) = \frac{ak^4}{(k^4 + q^4)^{1+\alpha}} \exp(-bk^{1.1}), \quad (4.11)$$

where $b = 0.02$, $q = 1.5$, $\alpha = 2.8/12$, and a as a free parameter [127]. The initial phases are generated randomly. We start our simulation on a smaller grid and run it until the steady state is reached. We then use the steady solution of the lower grid as an initial condition for simulations on a larger grid size at a larger R . We continue this procedure till the turbulent state is reached. The final runs were performed on 512^3 grid for 20 large-eddy turnover time on 8 nodes (64 cores) and 16 nodes (128 cores) of EKA,

the supercomputer at the Computational Research Laboratory, Pune. Zero-P convection runs were performed on a 256^3 grid. The values of $k_{max}\eta$, where η is the Kolmogorov length, for our simulations are always greater than one indicating that our simulations are well-resolved.

For the energy flux calculation, we divide the wavenumber space into 20 shells. The first three shells are $k = (0, 2)$, $[2, 4)$, and $[4, 8)$, while the last shell contains all modes beyond $k = 568$. Between $k = 8$ and $k = 568$, the wavenumber space is split into shells bounded by $[k_n, k_{n+1})$ with $k_n = 8 \times 2^{s(n-4)}$ where $s = (1/15) \log_2(568/8)$.

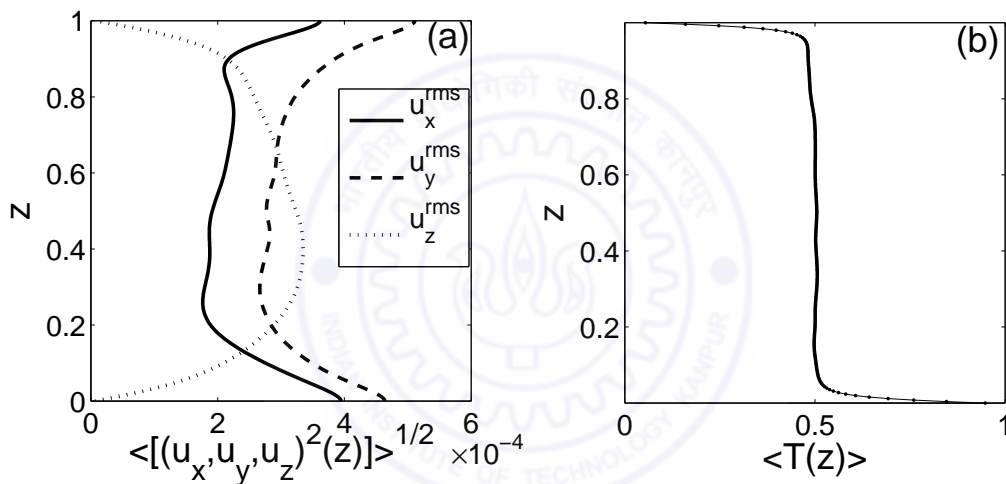


Figure 4.1: For $R = 6.6 \times 10^6$ and $P = 6.8$: (a) the vertical variation of the velocity fluctuations averaged over the horizontal planes. The solid, dashed, and dotted lines represent the rms values of u_x^{rms} , u_y^{rms} , and u_z^{rms} , respectively; and (b) the vertical variation of the horizontally averaged mean temperature. This Figure is taken from [122].

For free-slip boundary conditions, the viscous boundary layer is practically absent, while the thermal boundary layer is significant [128]. To probe the existence of these boundary layers, we compute the average value of the rms velocity fluctuations and the temperature field over the horizontal planes. Figs. 4.1(a) & 4.1(b), respectively, exhibit these quantities as a function of the vertical height for $R = 6.6 \times 10^6$ and $P = 6.8$. We observe a thin thermal boundary layer near the horizontal plates ($\delta/d \sim 0.05$). The

slow variation of the velocity fluctuations, however, demonstrate the insignificance of the viscous boundary layer. Our results are consistent with an earlier work on boundary layers [128].

No-slip boundary conditions are encountered more often in convection experiments. In our work we use free-slip boundary conditions for simplification. An added advantage of the free-slip boundary conditions could be a reduction in the complexity of the viscous boundary layer, as a result of which the energy spectrum of the flow may reflect the bulk properties. Thus, we may be able to probe the validity of the KO or BO scaling for the bulk flow using these simulations. Note that several properties of convection are the same for both free-slip and no-slip boundary conditions, e.g., the scaling exponent of the Nusselt number vs. Rayleigh number is the same for the two boundary conditions [129].

We choose five representative Prandtl numbers $P = 0, 0.02, 0.2, 1,$ and 6.8 for our energy spectra and flux studies. We compute the energy spectra and fluxes, and the Nusselt number using the numerically generated data. We also compute $\epsilon^u, \epsilon^\theta$ using the exact relationships [Eqs. (1.37) - (1.38)]. Kolmogorov's dissipation wavenumber (k_d) and "Kolmogorov's diffusion wavenumber" (k_c) are also computed using the phenomenology of passive scalar turbulence [123]:

$$k_d = \left(\frac{\epsilon^u}{\nu^3} \right)^{1/4}, \quad (4.12)$$

$$k_c = \left(\frac{\epsilon^u}{\kappa^3} \right)^{1/4}, \quad (4.13)$$

$$\implies \frac{k_c}{k_d} = P^{3/4}. \quad (4.14)$$

In Table 4.1, we list the numerically computed and the estimated ϵ^u and ϵ^θ , k_c , k_d , and inverse of the Bolgiano length. The Bolgiano length is calculated by using Eq. 1.36. The estimated values of ϵ^u and ϵ^θ match quite well with the simulation results, thus validating our simulations.

In the following, we discuss our numerical results on the energy spectra and fluxes for the chosen Prandtl numbers.

Table 4.1: Estimates of the viscous dissipation (ϵ^u) and the thermal diffusion (ϵ^θ) rates from numerical simulations and by using theoretical relationships [Eqs. (1.37) - (1.38)], the inverse of the Bolgiano length (l_B^{-1}), Kolmogorov's dissipative wavenumber (k_d), and Kolmogorov's diffusive wavenumber (k_c). The reported quantities are nondimensional: $\epsilon^u = (Nu - 1)/\sqrt{RP}$, $\epsilon^\theta = Nu/\sqrt{RP}$, $k_d = [(Nu - 1)R/P^2]^{1/4}$, and $k_c = [(Nu - 1)RP]^{1/4}$.

P	R	Nu	ϵ^u (estim.)	ϵ^u (comp.)	ϵ^θ (estim.)	ϵ^θ (comp.)	l_B^{-1}	k_d	k_c
0.02	2.6×10^6	8.5	0.033	0.032	0.037	0.037	5.2	470.3	25.0
0.2	6.6×10^6	17	0.014	0.014	0.015	0.015	8.2	227.0	68.0
1.0	6.6×10^6	32	0.012	0.0082	0.013	0.0085	9.0	108.6	108.6
6.8	6.6×10^6	30	0.004	0.0043	0.0042	0.0042	15.0	44.2	186.2

4.3.1 Prandtl number $P = 0$

For $P = 0$, the temperature fluctuations can be expressed as $\theta(\mathbf{k}) = u_3(\mathbf{k})/k^2$ [see Eq. (1.17)]. Consequently $E^\theta(k) \approx E^u(k)/k^4$. Hence the entropy spectrum is very steep for zero-P convection, and we can safely assume that the velocity field is buoyantly forced only at very large scales (small k). Hence, Kolmogorov's argument for fluid turbulence must be valid for zero-Prandtl number convection. These arguments closely resemble the mathematical derivation of Spiegel [5].

We performed the DNS for $P = 0$ at $R = 1.97 \times 10^4$ and computed the energy spectrum using the steady-state data. In Fig. 4.2, we plot the compensated energy spectra $E(k)k^{5/3}$ (KO) and $E(k)k^{11/5}$ (BO). Clearly, the numerical plots fit better with the KO scaling than the BO scaling, thus verifying the above phenomenological arguments. Using the simulation data, we also compute the kinetic energy flux which is plotted in Fig. 4.3. The kinetic energy flux is flat in the inertial range, which is in agreement with the KO scaling. The Kolmogorov constant for $P = 0$ is around 1.8 (with significant error) which is in a reasonable agreement with the expected value of 1.6 (Kolmogorov's constant for fluid turbulence).

In the next subsection, we discuss the numerical results for $P = 0.02$, which can be taken as a representative case for low-Prandtl number convection.

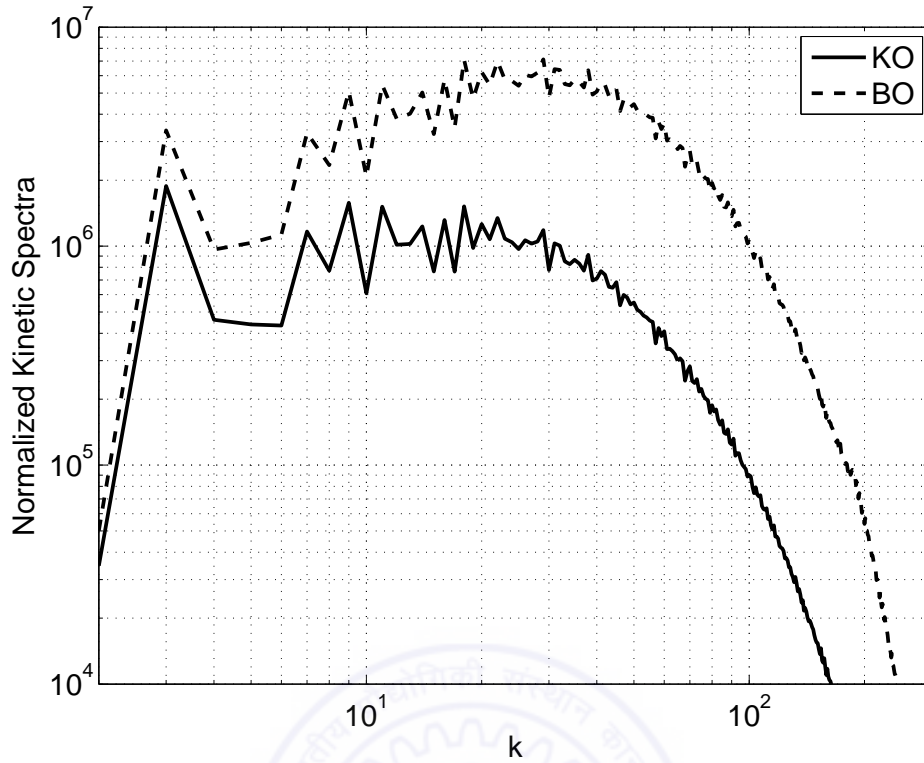


Figure 4.2: Plot of the compensated kinetic energy spectra $E^u(k)k^{5/3}$ (KO) and $E^u(k)k^{11/5}$ (BO) vs. k for $R = 1.97 \times 10^4$ and $P = 0$ on a 256^3 grid. The DNS spectrum matches with the KO spectrum quite well. This Figure is taken from [122].

4.3.2 Prandtl number $P = 0.02$

In the previous subsection, we showed that Kolmogorov's scaling (KO) is expected to hold for zero- P convection because buoyancy in this case is dominant at very small wavenumbers only. Here, we will attempt to extend the above arguments to low-Prandtl number convection. The inertial range for the velocity and temperature fields extends almost up to the Kolmogorov dissipative wavenumber (k_d) and the Kolmogorov diffusive wavenumber (k_c), respectively. For low- P convection, where thermal diffusivity dominates kinematic viscosity, we expect $k_c \ll k_d$ [see Eq. (4.14)]. According to the turbulence phenomenology of passive scalar turbulence, $E^\theta(k)$ is a power law for $k < k_c$, and it decays exponentially for $k > k_c$. Hence the buoyancy, which is proportional to θ (cf. Eq. (4.1)), would be dominant only for low wavenumbers ($k \leq k_c$), and we expect Kolmogorov's spectrum for the kinetic energy $E^u(k)$ for $k_c < k < k_d$.

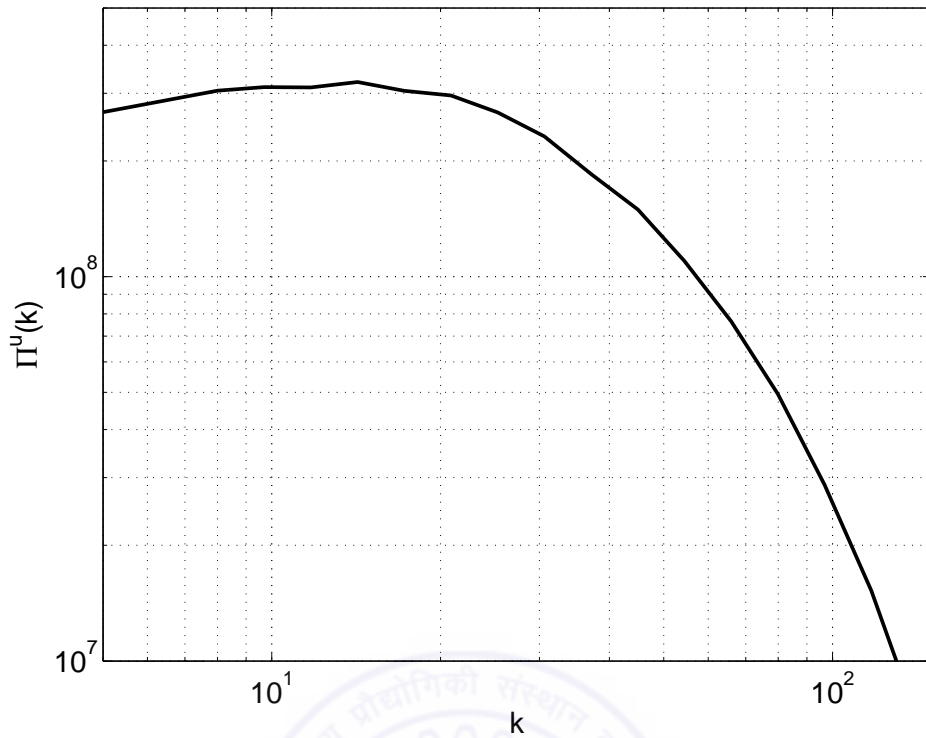


Figure 4.3: Plot of the kinetic energy flux vs. k for $R = 1.97 \times 10^4$ and $P = 0$ on a 256^3 grid. The constancy of the flux in the inertial range indicates that zero- P convection follows Kolmogorov’s scaling. This Figure is taken from [122].

According to Eq. (4.13), for small ϵ^u and large κ , k_c could be rather small. Under such situations, the above phenomenological arguments indicate that the velocity field follows Kolmogorov’s spectrum, and the temperature field exhibits a diffusive energy spectrum. Interestingly, the above arguments for low-Prandtl number convections are consistent with the zero- P convection case for which $k_c \rightarrow 0$ (asymptotic case). As argued by Grossmann and L’vov [52], the Bolgiano length for low- P convection could be of the order of the box size, and so BO scaling is not expected for low- P convection.

When k_c is large, we need more rigorous theoretical arguments to predict the energy spectra for $k < k_c$. Possibly, the buoyancy term is irrelevant in the “renormalization group” sense (see [130]), and both the velocity and temperature fields may follow KO scaling for $k < k_c$ in the inertial range. This scenario is observed for $P = 0.2$, which will be discussed in the next subsection.

In the following discussion, we will compare the above phenomenological predictions

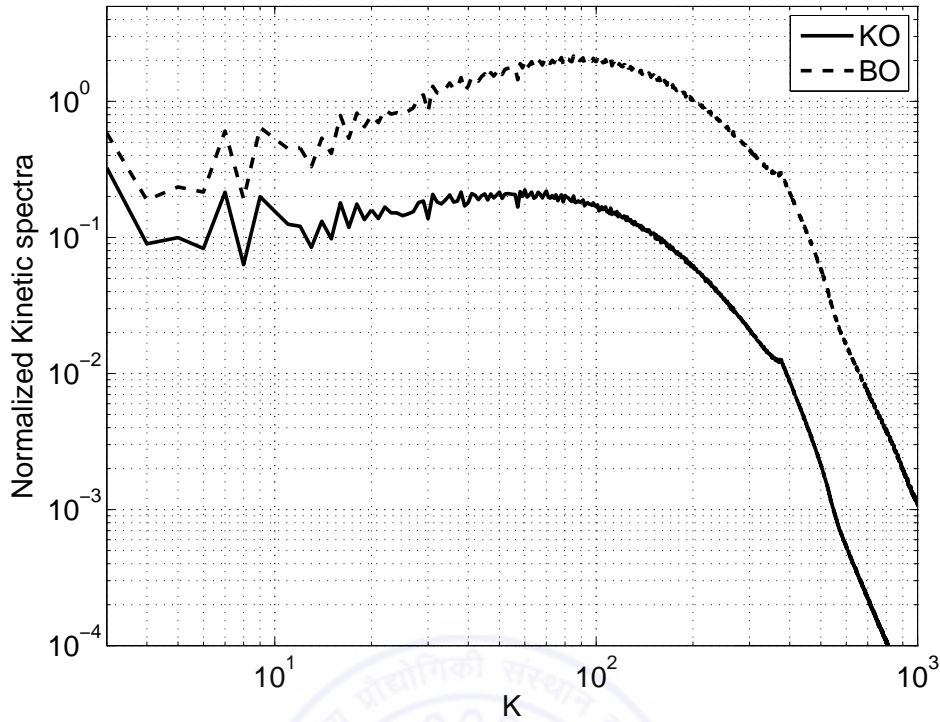


Figure 4.4: Plot of the compensated kinetic energy spectra $E^u(k)k^{5/3}$ (KO) and $E^u(k)k^{11/5}$ (BO) vs. k for $R = 2.6 \times 10^6$ and $P = 0.02$ on a 512^3 grid. The KO scaling is in better agreement than the BO scaling. This Figure is taken from [122].

with the numerical results. For $P = 0.02$, we perform numerical simulations at $R = 2.6 \times 10^6$ which is at the lower end of the turbulent convection regime. We compute k_c , k_d , ϵ^u , ϵ^θ , l_B^{-1} , and the energy spectra and fluxes using the numerical data. As evident from the entries of Table 4.1, $k_c \simeq 25$, which is much smaller than $k_d \simeq 470$. According to the arguments given above, we expect a diffusive entropy spectrum for $k_c < k < k_d$. We do not expect to observe KO scaling for $k < k_c$ since k_c is too small. Fig. 4.4 shows the compensated kinetic energy spectra for both the KO and BO scaling. The KO scaling fits better with the numerical data than the BO scaling, consistent with the above phenomenological arguments. Fig. 4.5 exhibits the entropy spectrum which contains two distinct branches similar to those observed by Vincent and Yuen [72] and Paul *et al.* [73] in their 2D spectral simulations with similar boundary conditions as ours. In the Appendix A we construct phenomenological arguments based on the energy equations and numerical results to estimate the values of the temperature modes $\theta(0, 0, 2n)$. We observe that the

P	$\theta(0, 0, 2)$	$\theta(0, 0, 4)$	$\theta(0, 0, 6)$	$\theta(0, 0, 8)$
6.8	-0.16	-0.077	-0.050	-0.036
0.2	-0.15	-0.061	-0.031	-0.017
0.02	-0.13	-0.040	-0.017	-0.0081
$-\frac{1}{2n\pi}$	-0.16	-0.080	-0.053	-0.040

Table 4.2: Numerical values of $\theta(0, 0, 2)$, $\theta(0, 0, 4)$, $\theta(0, 0, 6)$, and $\theta(0, 0, 8)$ modes for $P = 6.8, 0.2$ and 0.02 . Our phenomenological arguments with numerical ingredients indicate that $\theta(0, 0, 2n) \simeq -1/(2n\pi)$. This Table is taken from [122].

maximum entropy transfers from the modes $\theta(n, 0, n)$ and $\theta(0, n, n)$ are to the modes $\theta(0, 0, 2n)$ (the three indices are i_x, i_y , and i_z respectively). These arguments lead to our predictions that $\theta(0, 0, 2n) \simeq -1/(2n\pi)$, and $E^\theta(2n) \simeq 1/(4n^2\pi^2)$. For $P = 0.02$ we have listed the values of $\theta(0, 0, 2n)$ for $n = 1$ to 4 in Table 4.2. Here $\theta(0, 0, 2) \simeq -1/2\pi$, but for higher n 's, $|\theta(0, 0, 2n)| < 1/(2n\pi)$, possibly due to significant entropy transfers to other modes or due to higher thermal diffusion for low- P convection. As we will show later, the relationship $\theta(0, 0, 2n) \simeq -1/(2n\pi)$ works quite well for large- P convection. However, a common feature borne out for all Prandtl numbers is that the entropy contents of $\theta(0, 0, 2n)$ modes are much larger than those of the other thermal Fourier modes, thus, consequently, yielding two branches of the entropy spectrum.

We compare the entropy spectrum with both power law and exponential fits (see Fig. 4.5). As evident from the figure, $E^\theta(k) \sim \exp(-ak)$ (the inset), which is in agreement with the phenomenological arguments given in the beginning of this subsection. We complement our spectral analysis with energy flux studies. Fig. 4.6 shows the kinetic energy and entropy fluxes. The kinetic energy flux is flat for more than a decade indicating Kolmogorov's spectrum for the velocity field, which is in agreement with KO scaling for the velocity field. The entropy flux, however, drops sharply, which is consistent with the exponential nature of the entropy spectrum. Using Eqs. (1.37) & (1.38), we compute ϵ^u and ϵ^θ , which turn out to be close to the numerically computed energy and entropy fluxes (see Table 4.1). Also, the numerical estimates of k_c and k_d are in general agreement with the spectra and flux plots.

On the whole, the numerical results for $P = 0.02$, which is a representative of low- P convection, appear to favour KO scaling for the velocity field. The temperature spectrum

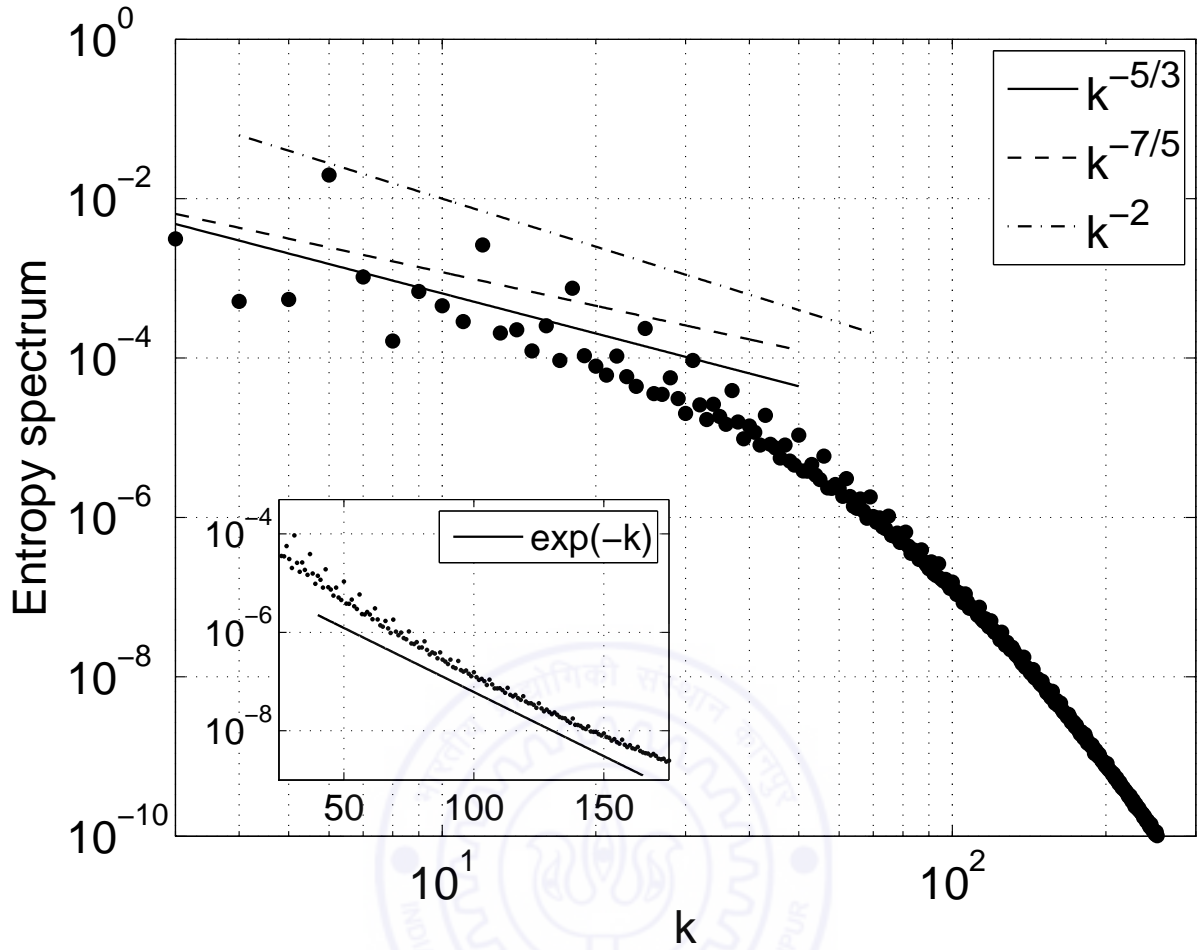


Figure 4.5: Plot of the entropy spectrum for $R = 2.6 \times 10^6$ and $P = 0.02$ on a 512^3 grid. The exponential fit in the inset indicates the diffusive nature of the entropy spectrum. The upper part of the entropy spectrum corresponds to the $\theta(0, 0, 2n)$ modes. This Figure is taken from [122].

appears to be diffusive for most of the wavenumber region. These numerical results are in good agreement with the phenomenological arguments presented above for low- P convection.

In the next subsection, we report the energy spectra and fluxes for the $P = 0.2$ case.

4.3.3 Prandtl number $P = 0.2$

We now present our numerical results for $P = 0.2$ at $R = 6.6 \times 10^6$. In Fig. 4.7, we plot the compensated kinetic energy spectra $E^u(k)k^{5/3}$ (KO) and $E^u(k)k^{11/5}$ (BO). Even though both the BO and KO scaling do not fit very well with the numerically computed

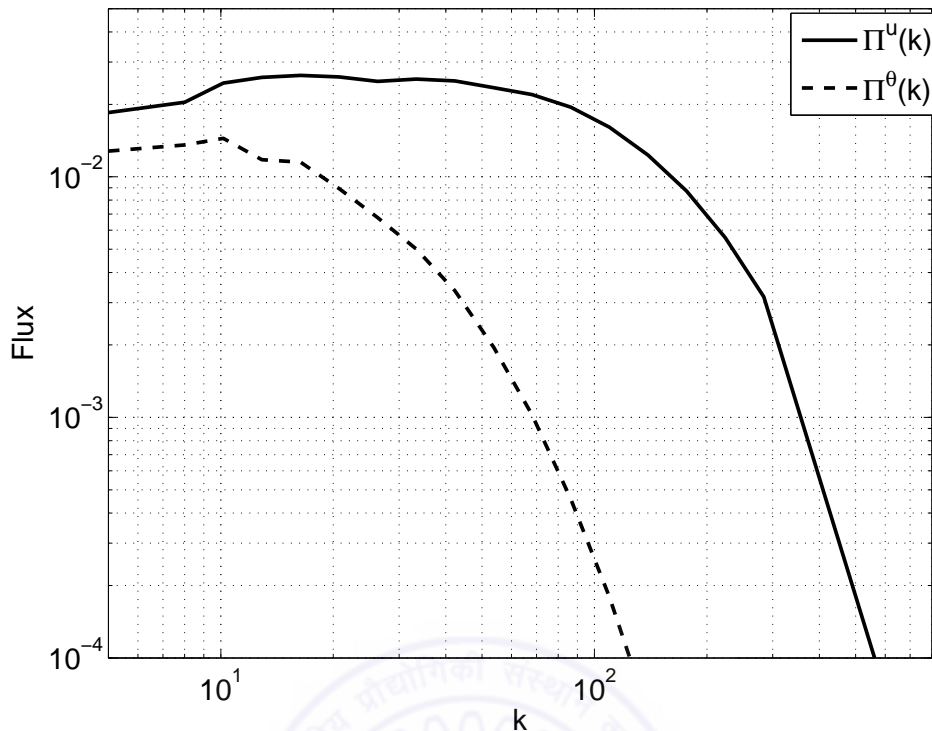


Figure 4.6: Plot of the kinetic energy flux (solid line) and the entropy flux (dashed line) vs. k for $R = 2.6 \times 10^6$ and $P = 0.02$ on a 512^3 grid. The kinetic energy flux is constant in a narrow inertial range, indicating agreement with Kolmogorov's scaling for the velocity field. The entropy flux appears to decay rather sharply suggesting diffusive entropy spectrum. This Figure is taken from [122].

energy spectrum, yet the KO scaling is in better agreement with the numerical data than the BO scaling.

In Fig. 4.8, we plot the entropy spectrum, which has a significant inertial range. Note that $k_c = 68$ (see Table 4.1). We obtain bi-spectra similar to $P = 0.02$ case. As described in the Appendix A, the upper curve represent the spectrum of the Fourier modes $\theta(0, 0, 2n)$, which matches reasonably well with the k^{-2} fits. As evident from the entries of Table 4.2, $\theta(0, 0, 2n)$ matches with $-1/(2n\pi)$ with a scaling factor of 2. The lower curve, however, appears to fit better with KO scaling than BO scaling. Note that the upper curve of the entropy spectrum contains a small number of Fourier modes, and hence, the non-linear energy transfers from these modes may be insignificant. There are a large number of Fourier modes associated with the lower branch of $E^\theta(k)$, and the energy flux possibly results from the nonlinear interactions among these modes. For this reason, we compare the lower branch of the entropy spectrum to either KO or BO scaling.

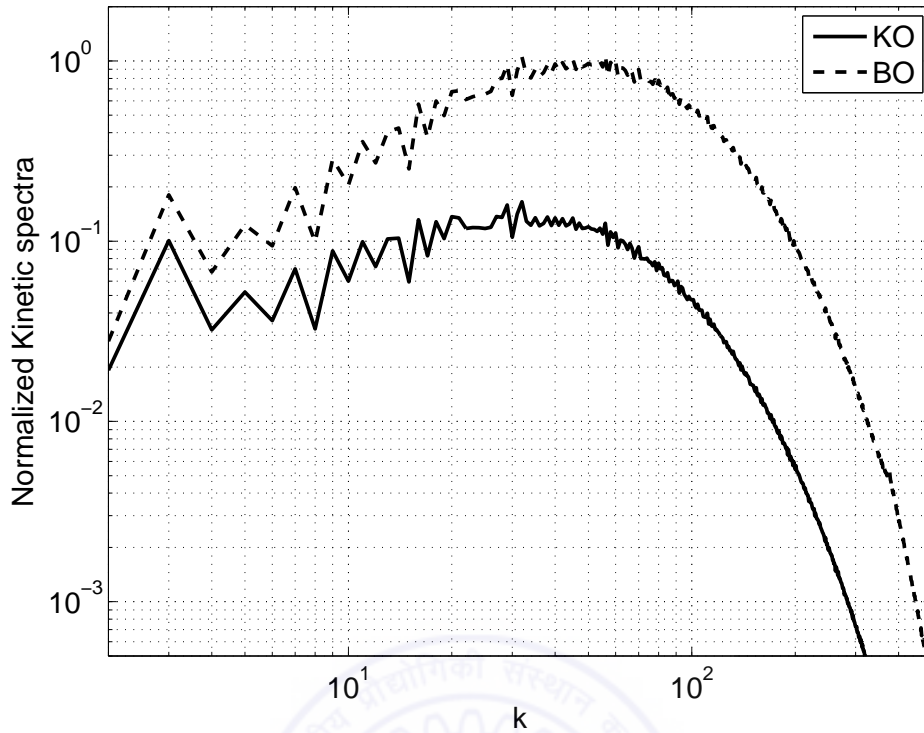


Figure 4.7: Plot of the compensated kinetic energy spectra $E^u(k)k^{5/3}$ (KO) and $E^u(k)k^{11/5}$ (BO) vs. k for $R = 6.6 \times 10^6$ and $P = 0.2$ on a 512^3 grid. The numerical results match better with the KO scaling than the BO scaling. This Figure is taken from [122].

Next, we compute the energy fluxes for the velocity and temperature fields for the same run. We observe constant fluxes for both the velocity and temperature fields as exhibited in Fig. 4.9. Thus, both energy spectra and flux results appear to favour the KO scaling more than the BO scaling. Given the kinetic energy spectrum and flux (in the common inertial range), we compute Kolmogorov's constant using Eq. (1.34) which yields $K_{Ko} \approx 2.0$ with significant error. Considering the uncertainties in the numerical fits, this value is in a reasonable agreement with Kolmogorov's constant for fluid or passive-scalar turbulence measured earlier using experiments and numerical simulations.

We also compute ϵ^u , ϵ^θ , k_d , and k_c using Eqs. (1.37), (1.38), & (4.12,4.13). These numbers are listed in Table 4.1. The predicted values of ϵ^u and ϵ^θ are in general agreement with the simulation results. We observe that $k_c < k_d$, which is also evident in the spectra and flux plots. An important point to note is that $k_c \sim 68$ is rather large. Hence, the arguments presented in the previous subsection for low-P convection will not hold here.

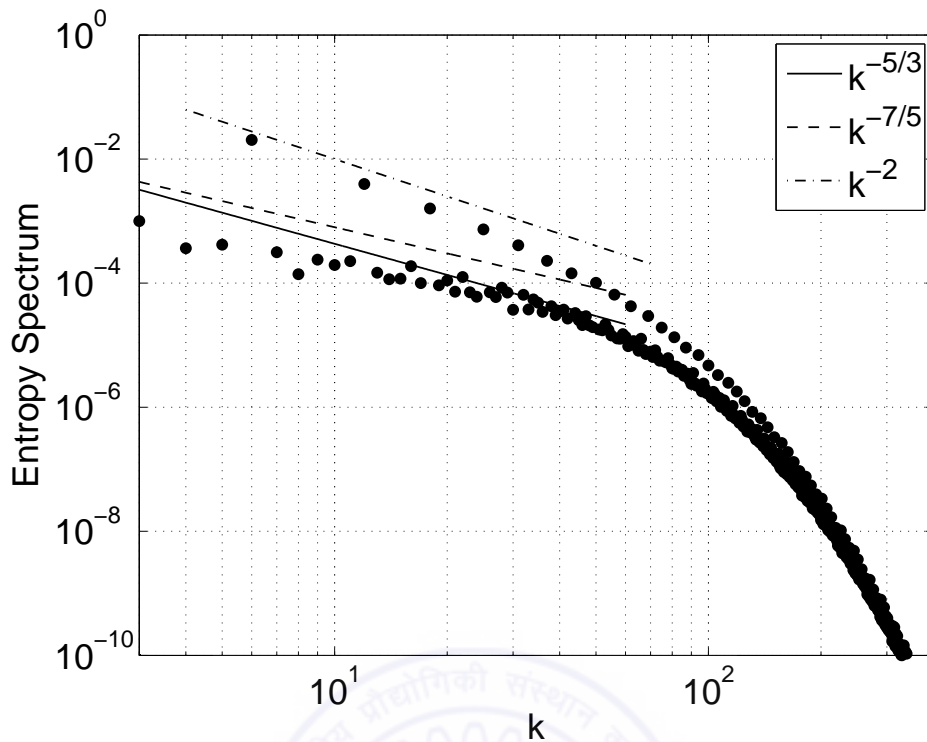


Figure 4.8: Plot of the entropy spectrum vs. k for $R = 6.6 \times 10^6$ and $P = 0.2$ on a 512^3 grid. The lower part of the entropy spectrum matches better with KO scaling than BO scaling. The upper part of the entropy spectrum corresponds to the $\theta(0, 0, 2n)$ modes, and is in general agreement with the k^{-2} fit. This Figure is taken from [122].

More rigorous arguments are required to understand the phenomenology for $P = 0.2$.

After considering $P = 0.2$, we turn to convection with $P = 1$.

4.3.4 Prandtl number $P = 1$

Next, we present the energy spectra and fluxes for the kinetic energy and entropy for $P = 1$ at $R = 6.6 \times 10^6$. Figs. 4.10 and 4.11 exhibit the compensated kinetic energy spectra and entropy spectrum respectively. The kinetic energy spectra plots are inconclusive since both the compensated plots for the KO and BO scalings are equally flat, albeit at different wavenumber ranges.

The entropy spectrum, shown in Fig. 4.11, has two distinct branches similar to the low- P cases. In agreement with the arguments of the Appendix A, the upper branch of the entropy spectrum follows $E^\theta(2n) \sim n^{-2}$. A comparison of the lower curve with the

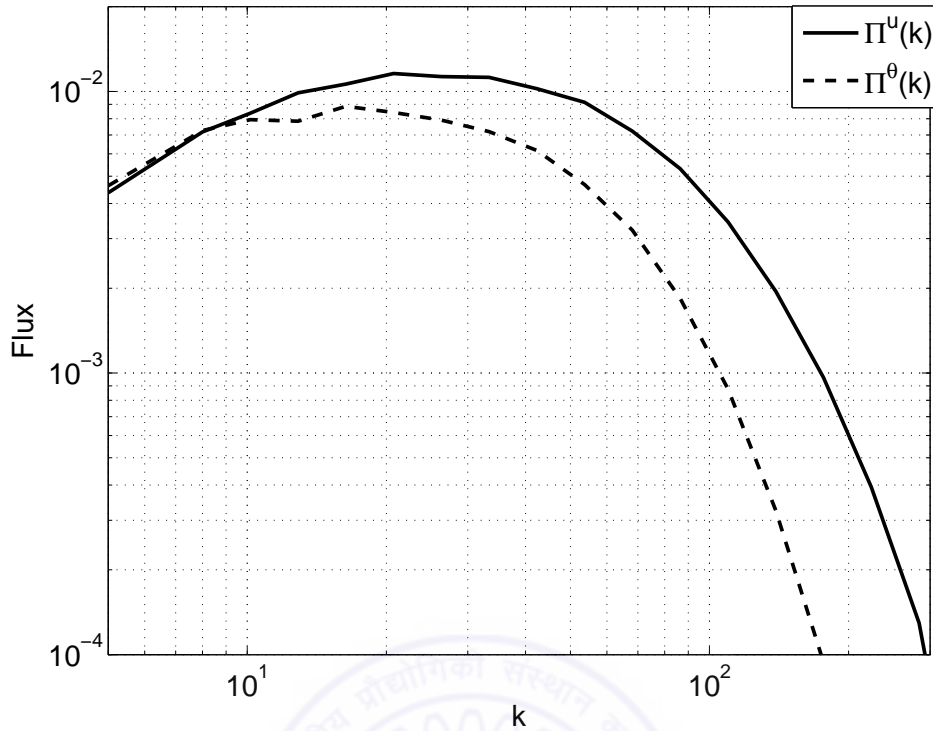


Figure 4.9: Plot of the kinetic energy flux (solid line) and the entropy flux (dashed line) vs. k for $R = 6.6 \times 10^6$ and $P = 0.2$ on a 512^3 grid. The kinetic energy and entropy fluxes are constant in the narrow inertial range indicating a general agreement with the KO scaling. This Figure is taken from [122].

BO or KO scaling indicates that neither of the scaling fits well with the numerical data. Fig. 4.12 shows the kinetic energy and entropy fluxes along with the compensated kinetic energy flux $\Pi^u(k)k^{4/5}$. The flux plots are also inconclusive.

Overall, the numerical results for $P = 1$ are rather inconclusive. The inverse Bolgiano length for $P = 1$ is approximately 9.0 (see Table 1), and, hence, the phenomenologies predict BO scaling for $k < 9\pi \sim 28$ and KO scaling for $28 < k < k_d$. Clearly, the wavenumber range of BO or KO scaling is too small to be able to infer any scaling. Also, the arguments put forth for the validity of the KO scaling for low- P convection were based on the dominance of buoyancy force for low wavenumbers and those cannot be extended to $P \geq 1$.

In the next subsection, we discuss the simulation results on convective turbulence for $P = 6.8$.

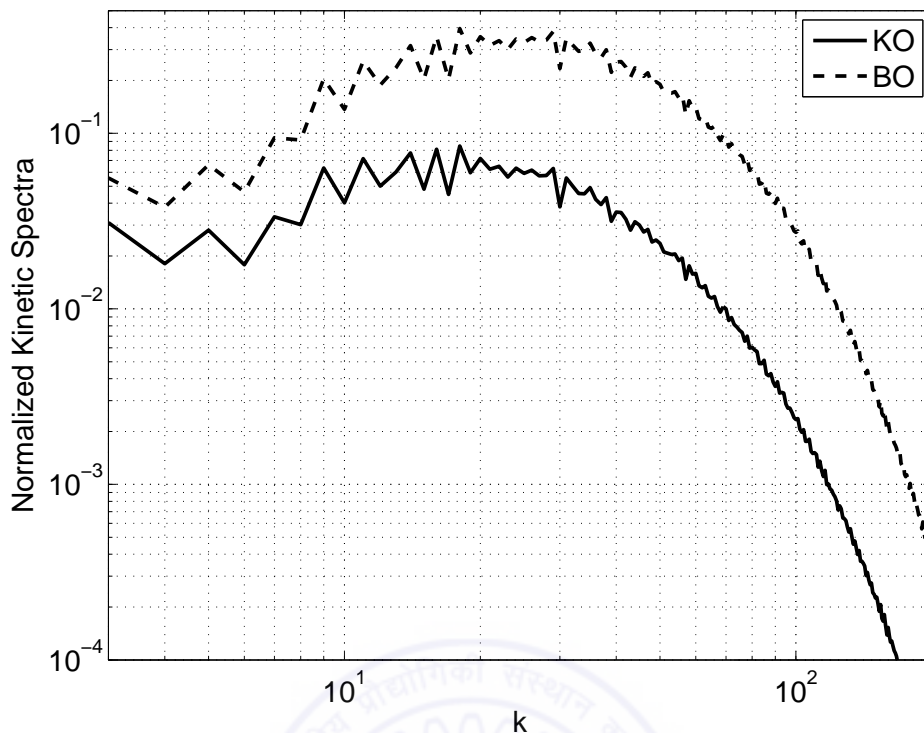


Figure 4.10: Plot of the compensated kinetic energy spectra $E^u(k)k^{5/3}$ (KO) and $E^u(k)k^{11/5}$ (BO) vs. k for $R = 6.6 \times 10^6$ and $P = 1$ on a 512^3 grid. We cannot infer which phenomenology fits better with the plots. This Figure is taken from [122].

4.3.5 Prandtl number $P = 6.8$

Finally, we present the kinetic energy spectrum for $P = 6.8$ at $R = 6.6 \times 10^6$. In Fig. 4.13, we plot the compensated kinetic energy spectra $E^u(k)k^{5/3}$ (KO) and $E^u(k)k^{11/5}$ (BO). The flat regions in both the plots are rather short, but still the BO curve appears to be in better agreement with the numerical results than the KO curve. The inverse Bolgiano length, l_B^{-1} , is around 15.0. Hence, according to the convective turbulence phenomenology discussed in Section 1.3.2, the BO scaling hold for $k < \pi l_B^{-1}$, and the KO scaling should hold for $k > \pi l_B^{-1}$. The BO scaling appears to be present in our numerical results, but the KO scaling is not observable. The dominance of the dissipation for modes with $k > \pi l_B^{-1}$ in our 512^3 simulation may be a reason for the absence of the KO scaling. We need higher resolution simulation to investigate this issue.

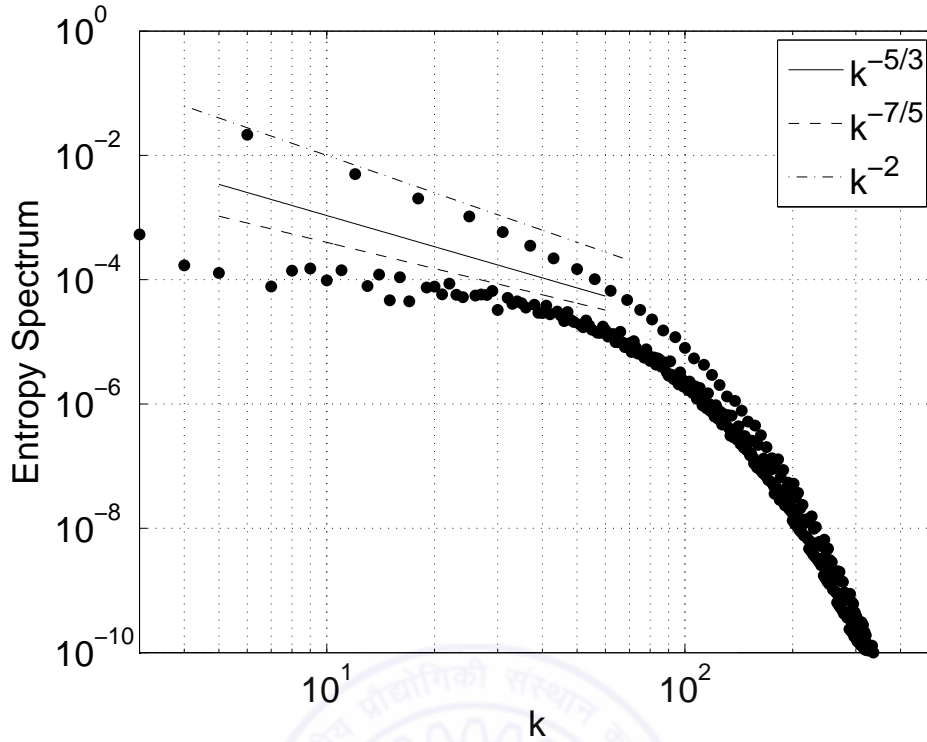


Figure 4.11: Plot of the entropy spectrum vs. k for $R = 6.6 \times 10^6$ and $P = 1$ on a 512^3 grid. Both the KO and BO lines do not fit with the lower branch of the entropy spectrum. The upper part of the entropy spectrum matches with k^{-2} quite well. This Figure is taken from [122].

Fig. 4.14 exhibits dual branches in the entropy spectrum similar to those discussed earlier. The upper spectral curves representing the modes $\theta(0, 0, 2n)$ follow the k^{-2} scaling as predicted in the Appendix A. The Fourier modes $\theta(0, 0, 2n) \simeq -1/(2n\pi)$, as evident from Table 4.2. For the lower branch, both the KO and BO scalings are not in good agreement with the entropy spectrum, yet the BO scaling fits better with the numerical data than the KO scaling.

Recall that for large- P convection, under the BO scaling, the entropy flux is constant but the energy flux varies as $k^{-4/5}$ (see Eq. (1.33)). By contrast, in the KO scaling the fluxes of the kinetic energy and the entropy are constant. In Fig. 4.15, we plot both the fluxes as well as the compensated kinetic energy flux $\Pi^u(k)k^{4/5}$. We observe that $\Pi^u(k)$ falls rather steeply as a function of the wavenumber k , but the compensated kinetic energy flux is constant in a narrow band of the inertial range. The entropy flux is also constant for a significantly large wavenumber range. Thus, the flux results tend to favor BO scaling

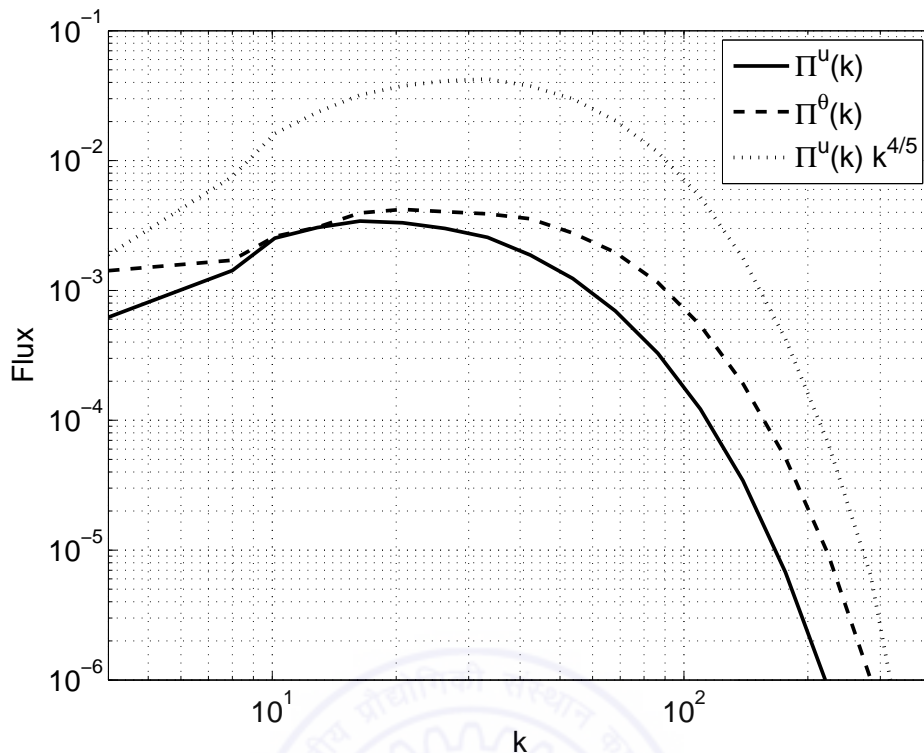


Figure 4.12: Plot of the kinetic energy flux (solid line) and the entropy flux (dashed line) vs. k for $R = 6.6 \times 10^6$ and $P = 1$ on a 512^3 grid. The dotted line represents the $\Pi^u(k)k^{4/5}$ curve. The flux results are inconclusive about the nature of the scaling. This Figure is taken from [122].

for $P = 6.8$.

Our numerical results on the energy spectra and fluxes are somewhat inconclusive, but the BO scaling appears to fit better with the simulation results.

4.4 Conclusions

In this chapter, we numerically computed the spectra and fluxes of the velocity and temperature fields of convective turbulence using the pseudo-spectral method. We performed these simulations for a large range of Prandtl numbers—zero-P, low-P, and large-P. The Rayleigh number of our simulations was around a million, which is at the lower end of the turbulent convection regime. We applied free-slip and thermal boundary conditions for our simulations. As a result, the viscous boundary layer was rather weak, but the thermal boundary layer was quite significant. Consequently, our numerical results possibly reflect

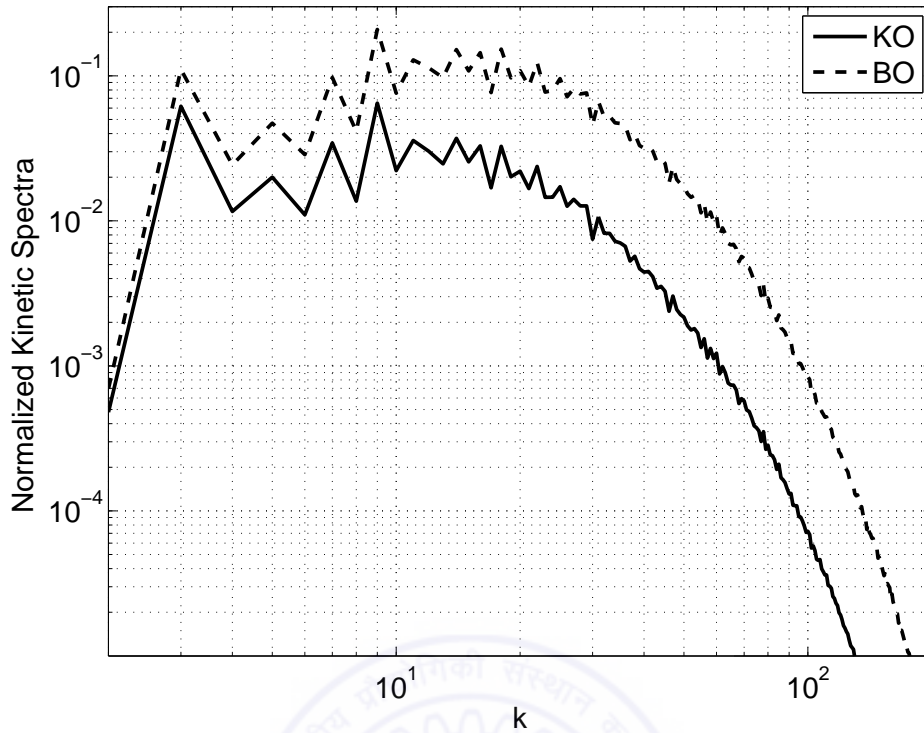


Figure 4.13: Plot of the compensated kinetic energy spectra $E^u(k)k^{5/3}$ (KO) and $E^u(k)k^{11/5}$ (BO) vs. k for $P = 6.8$ and $R = 6.6 \times 10^6$ on a 512^3 grid. The fit is somewhat inconclusive, yet the BO scaling appears to fit better with the numerical data than the KO scaling. This Figure is taken from [122].

the scaling for the bulk convective flow. The simulation results of the kinetic energy and entropy fluxes were in good agreement with their estimates using exact relations, thus validating our numerical simulations.

We found that for non-zero Prandtl numbers, the entropy spectrum exhibited dual branches. Our simulation results indicated that the maximum entropy transfer from the modes $\theta(n, 0, n)$ and $\theta(0, n, n)$ were to the modes $\theta(0, 0, 2n)$. These observations combined with the entropy evolution equations yielded $\theta(0, 0, 2n) \simeq -1/(2n\pi)$, and $E^\theta(2n) \simeq 1/(4n^2\pi^2)$. For large-P convection, these predictions fit very well with the upper branch of the entropy spectrum. The upper branch, however, had only a small number of modes, and they probably did not contribute significantly to the entropy flux. For this reason, we compared the lower branch of the entropy spectrum to either the Kolmogorov-Obukhov (KO) or the Bolgiano-Obukhov (BO) scaling.

For zero-P convection, the temperature field is expected to be active only for very

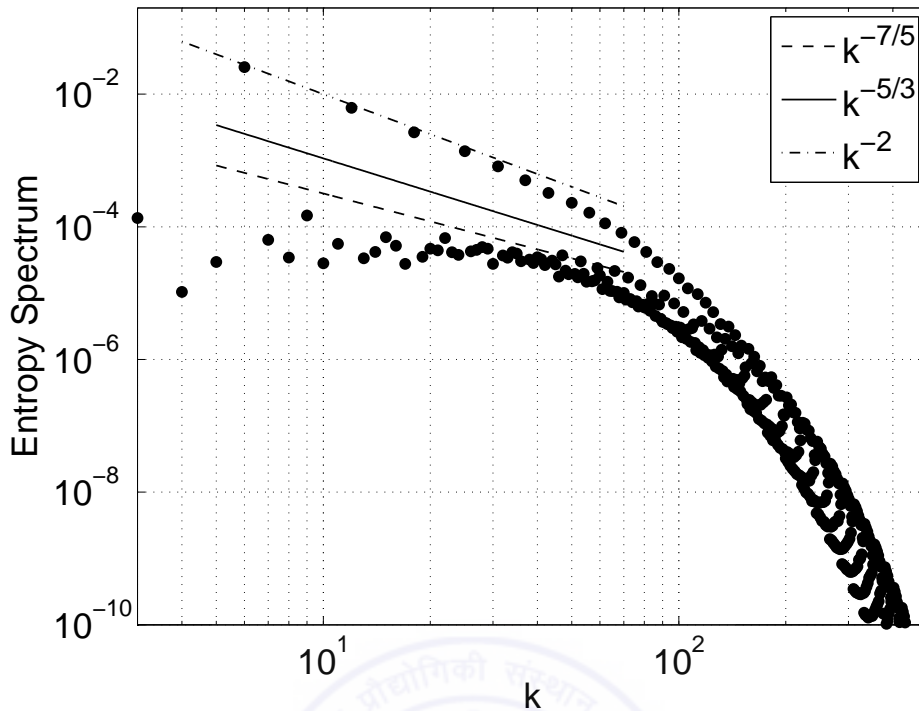


Figure 4.14: Plot of the entropy spectrum $E^\theta(k)$ vs. k for $P = 6.8$ and $R = 6.6 \times 10^6$ on a 512^3 grid. Even though both the KO and BO lines do not fit well with the data, the BO line is closer to the lower part of the spectrum. The upper branch matches with k^{-2} quite well. This Figure is taken from [122].

small wavenumbers since $E^\theta(k) \sim E^u(k)/k^4$. Hence, buoyancy is likewise expected to be active only for very small wavenumbers leading to Kolmogorov's scaling just like in fluid turbulence ($E^u(k) \sim k^{-5/3}$ and $\Pi^u(k) \sim \text{const.}$). We observed such behaviour in our numerical simulation.

The above phenomenological arguments for zero-P convection can be extended to low-P convection. For this case, Kolmogorov's diffusive wavenumber k_c is much smaller than Kolmogorov's dissipation wavenumber k_d . Hence, the temperature field will be diffusive for $k > k_c$, and the forcing due to the buoyancy is active only for low wavenumbers ($k < k_c$). Consequently, we expect Kolmogorov's spectrum for the velocity field for $k_c < k < k_d$. We numerically computed the energy spectra and fluxes for $P = 0.02$, and observed a diffusive spectrum for the temperature field and Kolmogorov's spectrum for the velocity field. Thus, the phenomenological arguments presented above were in agreement with our simulations. For $k < k_c$, the inertial range was too narrow to ascertain either of the KO or BO scalings. A large Rayleigh number simulation could possibly resolve the

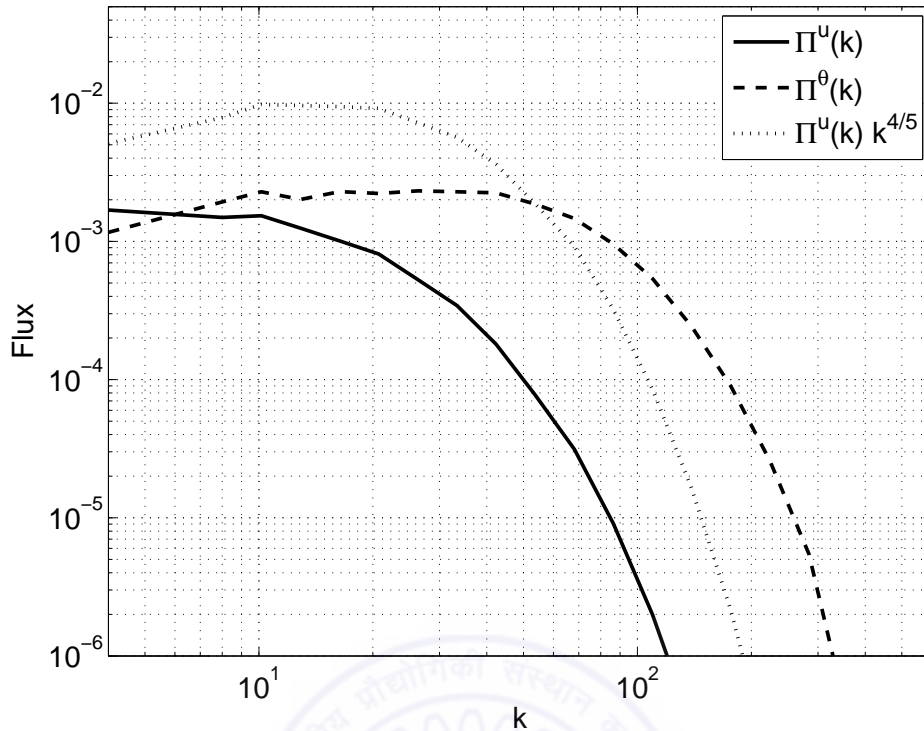


Figure 4.15: Plot of the kinetic energy flux (solid line) and the entropy flux (dashed line) vs. k for $R = 6.6 \times 10^6$ and $P = 6.8$ on a 512^3 grid. The normalized kinetic energy flux (multiplied by $k^{4/5}$) is also shown in the figure as a dotted line. $\Pi^u(k)k^{4/5}$ and $\Pi^\theta(k)$ are constant for a range of wavenumbers. This Figure is taken from [122].

scaling in this range.

We also computed the spectra and fluxes for $P = 0.2$. For this case, the KO scaling appeared to fit better than the BO scaling with the energy spectra and fluxes of the velocity and temperature fields as $E^u(k) \sim k^{-5/3}$, $E^\theta(k) \sim k^{-5/3}$, $\Pi^u(k) \sim const.$, and $\Pi^\theta(k) \sim const.$, respectively. Numerical results for $P = 1$ were inconclusive regarding the phenomenology. Simulations results for $P = 6.8$, which is a sample of large- P convection, were inconclusive, too. However, the BO scaling appeared to fit better than the KO scaling in this case. $P = 1$ and large- P convection require more refined simulations for resolving these issues.

When we compare our results with earlier experiments and simulations, we observe general agreement with the findings of Cioni *et al.* [69] where they reported KO scaling for mercury ($P = 0.02$, low- P), as also those of Chillá *et al.* [53], Zhou and Xia [62], and Shang and Xia [63], who performed experiments on water and reported the BO scaling

for it. A word of caution is in order: our simulations use free-slip boundary conditions which differ from the no-slip boundary conditions of the experiments. Also, realistic convective flows are quite complex due to the presence of boundary layers, anisotropic forcing (buoyancy), plumes, large scale circulation (LSC), etc., all of which have not been analyzed carefully in our analysis. Several past numerical simulations and experiments have attempted to study these features [76]. Our emphasis has been on the bulk energy spectrum and fluxes. Note that the plumes and LSC typically affect the low-wavenumber regime of the energy spectrum, and may not significantly affect the inertial-range isotropic energy spectra being investigated in this chapter.

In summary, we observe KO scaling for zero-P and low-P convection in our numerical simulations. For large-P convection, the numerical results are not very convincing, yet the BO scaling matches with the numerical results better than the KO scaling. These results are in general agreement with some of the earlier experimental and numerical results. We provide phenomenological arguments to support KO scaling for low-P and zero-P convection. More rigorous theories like renormalization group analysis and very high resolution simulations could be very useful in providing further insights into this complex problem. Unfortunately, convective turbulence simulations beyond 512^3 grids are prohibitively expensive at this stage. Also, more complex features like inhomogeneity, anisotropy, and the presence of boundary layers need to be investigated. Future experiments, simulations, and theoretical modeling will hopefully resolve this outstanding problem.

In the next chapter, we will describe large scale circulation and dynamics of wind reversals.

Chapter 5

Dynamics of reorientations and reversals of large scale flow in Rayleigh-Bénard convection

5.1 Introduction

In this chapter, we present a numerical study of the dynamics of large scale circulation (LSC), in particular, that related with azimuthal reorientations and reversals, for a convective fluid ($P = 0.7$) contained in a cylindrical container of aspect ratio one. The work described in this chapter is to appear in J. Fluid Mech. [131]. Earlier work related to LSC and wind reversals have been reviewed in Sec.1.3.2. Here, we will describe these works very briefly.

LSC, a coherent large scale structure which appears in the turbulent range of convection, exhibits many interesting dynamics: regular oscillations at the interval of one eddy turn-over time [80, 81, 86, 90, 94, 95], spontaneous azimuthal meandering in the azimuthal direction [86] and reorientations in the azimuthal direction of a cylindrical container of aspect ratio one [81, 84, 85], and random reversals [68, 82, 83]. It is observed experimentally that the plane containing the LSC exhibits diffusive motion along the azimuthal direction, and sometimes the orientation of the plane of the LSC changes by a significant angle. This

is called the reorientation of the LSC [84, 85]. The reorientation can occur in two ways: (i) without changing the strength of the flow, called rotation-led reorientation [81, 84, 85, 86], and (ii) through cessation of the LSC, in which the strength of the flow vanishes during the reorientation, called cessation-led reorientation [84, 86]. These aspects of the reorientations have been widely studied in laboratory experiments [68, 81, 82, 84, 85, 86, 93] and phenomenological models [83, 96, 97, 98, 99]. However, very few numerical studies have been performed to investigate the dynamics of reversals and reorientations of LSC. In a cylindrical container of aspect ratio one, Benzi and Verzicco [102] numerically studied the statistics of reversals of the flow for $R = 6 \times 10^5$ by adding random noise in the heat equation. There are a few numerical works in a 2D box which report the reversals of LSC due to cessation [103, 104, 105] or due to chaotic movement of rolls perpendicular to the roll-axis [106]. The numerical simulations are very demanding in the turbulent regime. So, some efforts have been put to understand the detailed dynamics of LSC using shell models. Benzi [96] used a SABRA shell model to investigate the dynamics of flow reversals observed in the laboratory experiment. However, the shell model could not capture many of the features, e.g., cessation and rotation led partial reorientations observed in the laboratory experiment and numerical simulation. We have presented a detailed review of the works related with experimental, numerical, and phenomenological investigations of LSC dynamics in Chapter 1.

The main goal of the present numerical study is to understand better the dynamics of convective flow during both the cessation- and rotation-led reorientations of LSC observed in laboratory experiments. In this chapter, we study the dynamics of reversals of convective structures using the direct numerical simulation (DNS) of turbulent RBC for $P = 0.7$ in a cylinder of aspect ratio one with a similar configuration as considered in the laboratory experiments. We choose a range of Rayleigh numbers varying from 6×10^5 to 3×10^7 for our study. We apply conducting boundary conditions on the top and bottom plates, and adiabatic boundary conditions on the lateral walls of the container. No-slip boundary conditions are applied on all the surfaces of the container. Our simulations indicate a regular oscillation in the LSC at an interval of one eddy-turn over time for high Rayleigh number ($R = 2 \times 10^7$ and $R = 3 \times 10^7$). Furthermore, we observe rotation-led

and cessation-led reorientations of the LSC similar to those observed in experiments. We compute the amplitudes and phases of the Fourier modes of the vertical velocity measured near the lateral wall in the mid-plane, and establish that the dynamics of the LSC can be captured quite well by the low wavenumber Fourier modes. We find that the amplitude of the second Fourier mode dominates over that of the first Fourier mode during cessation-led reorientations.

We present our simulation details in Section 5.2. The results pertaining to the observations of large scale circulations and their reorientations are presented in Section 5.3. We conclude by summarizing our results in Section 5.4.

5.2 Simulation details

We numerically simulate the convective flow in a cylinder. The Boussinesq approximation is assumed for the buoyancy term in the fluid. The relevant non-dimensionalized dynamical equations for the fluid are

$$\frac{\partial \mathbf{u}}{\partial t} + (\mathbf{u} \cdot \nabla) \mathbf{u} = -\nabla \sigma + T \hat{z} + \sqrt{\frac{P}{R}} \nabla^2 \mathbf{u}, \quad (5.1)$$

$$\frac{\partial T}{\partial t} + (\mathbf{u} \cdot \nabla) T = \frac{1}{\sqrt{PR}} \nabla^2 T, \quad (5.2)$$

$$\nabla \cdot \mathbf{u} = 0, \quad (5.3)$$

where $\mathbf{u} = (u_x, u_y, u_z)$ is the velocity field, T is the temperature field, σ is the deviation of the pressure from the conduction state, $R = \alpha g(\Delta T)d^3/\nu\kappa$ is the Rayleigh number, $P = \nu/\kappa$ is the Prandtl number, and \hat{z} is the buoyancy direction. Here, ν and κ are the kinematic viscosity and thermal diffusivity, respectively, d is the vertical height of the container, and ΔT is the temperature difference between the bottom and top plates. For the non-dimensionalization, we have used d as the length scale, $\sqrt{\alpha(\Delta T)gd}$ (free-fall velocity) as the velocity scale, and ΔT as the temperature scale. Consequently, $d/\sqrt{\alpha g \Delta T d}$ is the time scale of our simulation. The aspect ratio of the container is taken to be one. We confine our study to $P = 0.7$, which is a typical Prandtl number for air.

The above non-dimensionalized Eqs. (5.1) - (5.3) are solved numerically for a cylin-

dricl geometry using a finite-difference scheme. The details of the numerical techniques used for this study have been discussed in Chapter 2. The convective parts of the equations are discretized in cylindrical coordinates using Tam and Webb's fourth-order central explicit scheme with enhanced spectral resolution [111]. The diffusive part is discretized using the second-order central-difference scheme. For the time-advancement, we use the second-order Adam-Bashforth scheme for the nonlinear terms, and the Crank-Nicholson scheme for the diffusive terms. We perform simulations for Rayleigh numbers $R = 6 \times 10^5$, 8×10^6 , 2×10^7 , and 3×10^7 . A comparison with experimental results show that these Rayleigh numbers are near the threshold of the strong turbulence regime [95].

R	$N_r \times N_\theta \times N_z$	$\Delta_{min.}$	$\Delta_{max.}$	$l_{max.}$	η_h	N_{BL}	dt	Nu (comp)
6×10^5	$33 \times 49 \times 97$	0.007	0.02	0.064	0.057	9	0.001	7.6
6×10^5	$33 \times 90 \times 97$	0.006	0.017	0.035	0.057	9	0.001	7.4
8×10^6	$75 \times 96 \times 145$	0.003	0.011	0.033	0.025	7	0.001	15.1
8×10^6	$100 \times 120 \times 201$	0.002	0.008	0.026	0.025	9	0.0005	15.6
2×10^7	$100 \times 120 \times 201$	0.002	0.008	0.026	0.018	7	0.0005	22.1
2×10^7	$100 \times 180 \times 201$	0.002	0.007	0.017	0.018	7	0.0005	22.3
3×10^7	$100 \times 120 \times 201$	0.0018	0.008	0.026	0.016	6	0.0005	24.03

Table 5.1: N_r , N_θ , and N_z are the number of grids along the radial, azimuthal, and vertical directions of the cylindrical container; Δ_{min} and Δ_{max} are the minimum and maximum mean-grid sizes; $l_{max} = \max(2\pi r/N_\theta)$; η_h is the Kolmogorov length scale calculated using the expression $\eta_h \simeq \pi(P^2/R * Nu)^{1/4}$; N_{BL} is the number of points inside the thermal boundary layer; dt is the time resolution considered; and Nu (comp) is the Nusselt number obtained from the simulation.

The cylinder volume is discretized into variable grids with finer resolution near the boundary layers. Since the boundary layers significantly affect the dynamics of LSC in convective turbulence, it is necessary to resolve the regions near the top and bottom plates, and the lateral walls [132]. In our simulations, we choose uniform grids along the azimuthal direction, and non-uniform ones along the radial and vertical directions. For the grid-spacing, the Grötzbach condition [133] is used, according to which the mean-grid size $\Delta = (r\Delta\theta\Delta r\Delta z)^{1/3}$ should be smaller than the Kolmogorov and thermal diffusion length scales. Note that the Kolmogorov length scale (η_h) is estimated using the formula $\eta_h \simeq \pi(P^2/(R * Nu))^{1/4}$, where Nu is the Nusselt number. We also calculate the width of the thermal boundary layer using the formula $\delta_T \sim \frac{1}{2Nu}$ and ensure that the minimum

number of grid points inside the boundary layer (N_{BL}) should be in the range of 3 to 5. Number of grid points inside the thermal boundary layer is given in Table 5.1, and they satisfy the above condition. As our studies are related with the “reorientations” and

R	$N_r \times N_\theta \times N_z$	$\langle \epsilon_c^u \rangle / \langle \epsilon_a^u \rangle$	$\langle \epsilon_c^T \rangle / \langle \epsilon_a^T \rangle$	u_z^{rms}	T_{eddy}
6×10^5	$33 \times 49 \times 97$	0.93	1.26	0.078	26
6×10^5	$33 \times 90 \times 97$	0.93	1.34	0.083	24
8×10^6	$75 \times 96 \times 145$	1.00	1.33	0.118	17
8×10^6	$100 \times 120 \times 201$	1.10	1.34	0.107	19
2×10^7	$100 \times 120 \times 201$	1.12	1.35	0.185	11
2×10^7	$100 \times 180 \times 201$	1.08	1.34	0.174	12
3×10^7	$100 \times 120 \times 201$	-	-	0.201	10

Table 5.2: N_r , N_θ , and N_z are the number of grids along the radial, azimuthal, and vertical directions of the cylindrical container; $\langle \epsilon_c^u \rangle = \nu \langle |\nabla \mathbf{u}|^2 \rangle$ and $\langle \epsilon_c^T \rangle = \kappa \langle |\nabla T|^2 \rangle$ are the numerically calculated viscous and thermal dissipation rates, respectively; and $\langle \epsilon_a^u \rangle = \nu^3 (Nu - 1) RP^{-2} / d^4$ and $\langle \epsilon_a^T \rangle (= \kappa (\Delta T)^2 Nu / d^2)$ are the analytical values of the viscous and thermal dissipation rates, respectively. The third and fourth column show $\langle \epsilon_c^u \rangle / \langle \epsilon_a^u \rangle$ and $\langle \epsilon_c^T \rangle / \langle \epsilon_a^T \rangle$, respectively. u_z^{rms} is the rms value of the vertical speed of the flow, and $T_{\text{eddy}} = 2d / u_z^{\text{rms}}$ is the circulation time of the large scale flow.

“reversals” of the LSC, which require a longer time series, we choose smaller but adequate grid sizes for our simulation. For the present study, we choose: $33 \times 49 \times 97$ grids for the $R = 6 \times 10^5$ simulation, $75 \times 96 \times 145$ for $R = 8 \times 10^6$ simulation, and $100 \times 120 \times 201$ for $R = 2 \times 10^7$ simulation. Our simulations satisfy the Grötzsch condition as the minimum of the mean-grid sizes (Δ_{min}) is smaller than η_h (see Table 5.1). Note, however, that the maximum grid size $l_{\text{max}} = \max(2\pi r / N_\theta)$ is sometimes larger than η_h . To validate our code, we compare the numerically computed Nusselt numbers at two different grid sizes (one more resolved than the other) and find that the Nusselt numbers for the two different grids are quite close. We also calculate the kinetic energy dissipation rate $\langle \epsilon_c^u \rangle (= \nu \langle |\nabla \mathbf{u}|^2 \rangle)$ and the thermal dissipation rate $\langle \epsilon_c^T \rangle (= \kappa \langle |\nabla T|^2 \rangle)$ using the numerical data and compare them with their theoretical estimates $\langle \epsilon_a^u \rangle (= \nu^3 (Nu - 1) RP^{-2} / d^4)$ and $\langle \epsilon_a^T \rangle (= \kappa (\Delta T)^2 Nu / d^2)$, respectively [54]. The ratios $\langle \epsilon_c^u \rangle / \langle \epsilon_a^u \rangle$ and $\langle \epsilon_c^T \rangle / \langle \epsilon_a^T \rangle$ are listed in the Table 5.2. Clearly, the numerical kinetic dissipation rate is quite close to its analytical counterpart, with the maximum difference at 12%. For the thermal dissipation, the numerical value always seems to be higher than the analytical value, with the maximum difference around 35%. However, note that the theoretical estimates of $\langle \epsilon_c^u \rangle$ and $\langle \epsilon_c^T \rangle$ are

functions of the Nusselt number for which we substitute its numerically computed value. Our numerical results on dissipation rates appear to be less accurate as compared to those by Stevens *et al.* [132]. Also, our numerical thermal dissipation rates are always larger than the theoretical estimate in contrast to those by Stevens *et al.* [132] who report lower values compared to the corresponding theoretical estimate. The above discrepancies are probably due to the differences in the time integration schemes and the spatial derivative schemes used by us and Stevens *et al.* [132].

We use a fixed time-step dt which is listed in Table 5.1. Due to the computational complexity, the longest computer run for the $R = 2 \times 10^7$ case took approximately 45 days on 32 cores of the CHAOS cluster at IIT Kanpur. To ensure that the initial conditions do not affect our final results, we start every run with a conductive state modulated with random noise. We validate our numerical code by comparing our results with past numerical results. For example, our numerical results of the Nusselt number (Nu) for different Rayleigh numbers fit with a relation $Nu \simeq 0.143R^{0.297}$ which is in good agreement with the earlier numerical results of Stringano and Verzicco [101], and Verzicco and Camussi [134], and the experimental observations of Niemela *et al.* [68].

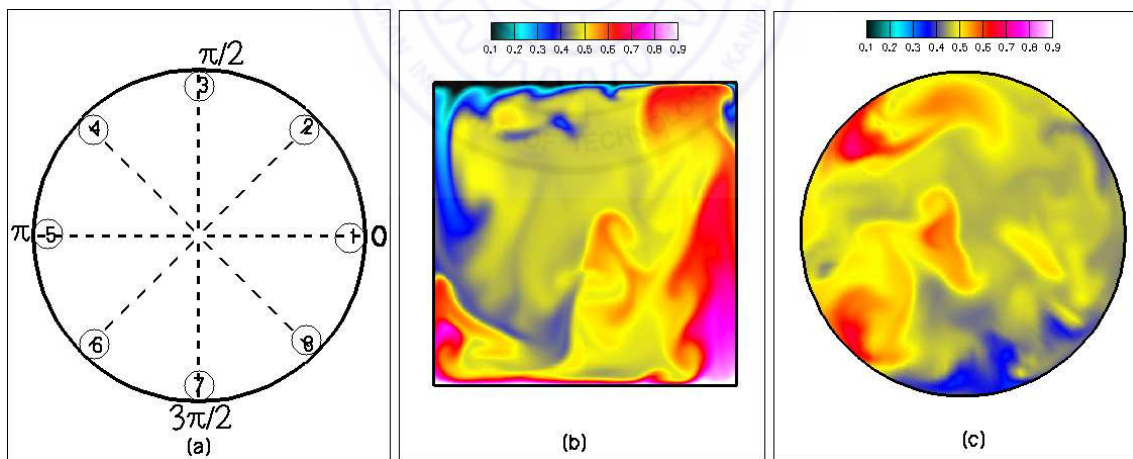


Figure 5.1: (a) Some of the velocity and temperature probes placed inside the cylinder. For most of our discussions in this chapter, we use the probes at $z = 0.5$, $r = 0.48$, and $\theta = j\pi/4$ with $j = 0 : 7$ as shown in the figure. (b) Temperature profile in the vertical plane $\theta = 3\pi/4$ for $R = 2 \times 10^7$ on a $100 \times 120 \times 201$ grid. A hot plume ascends from the right wall and a cold plume descends from the left wall confirming the presence of a large scale structure. (c) Temperature profile in the horizontal section $z = 0.5$ for $R = 2 \times 10^7$ on a $100 \times 120 \times 201$ grid. This Figure is taken from [131].

Similar to some of the earlier experiments [81, 84, 85, 93], we place “probes” in the

bulk and in the boundary layers of the cylinder to record the time series of the velocity and temperature fields. The probes are located at $\theta = \theta_j = j\pi/4$ ($j = 0 : 7$), the vertical heights of $z = 0.02, 0.25, 0.5, 0.75$, and 0.98 ; and radial distances of $r = 0.15, 0.3$, and 0.48 from the axis. The bottom and top probes are inside the thermal boundary layers. A schematic diagram of the probes in the middle plane is depicted in Fig. 5.1(a). The non-dimensional rms values of the velocity u_z^{rms} , and the eddy turn-over time ($T_{\text{eddy}} = 2d/u_z^{\text{rms}}$) for various R 's are listed in Table 5.2. The u_z^{rms} values have been computed by taking the time average of $\frac{1}{8}(\sum_{i=1}^8 (u_z^i)^2)^{1/2}$ for the eight probes placed at $z = 0.5$ and $r = 0.48$. The eddy turnover time ranges from 26 to 10 free fall times for the range of Rayleigh numbers studied here; its value decreases with an increase of the Rayleigh number, which is consistent with the earlier results of Qiu and Tong [94].

In the next section, we will study the properties of the temperature and velocity time series, and relate them to the earlier experimental results on the reversals of LSC.

5.3 Numerical results

5.3.1 Large scale circulation

The time series measured by the probes in Fig. 5.1(a) carries the signature of the LSC which will be described below. Later on in this section, we will relate the reversals of the vertical velocity field with the reorientation of the LSC. In Figs. 5.1(b) and 5.1(c), we display the temperature profiles for $R = 2 \times 10^7$ for a vertical plane ($\theta = 3\pi/4$) and the middle horizontal plane ($z = 0.5$), respectively. As a supplementary material [135], we also provide two short movies depicting the flow behaviour for the above two sections. These figures and movies clearly indicate the presence of convective structures in the flow.

In Figs. 5.2(a,b,c,d) we plot the normalized autocorrelation function $g_c(\tau) = \langle \delta T(t) \delta T(t + \tau) \rangle / \sigma_T^2$ at $\theta = 0, r = 0.48$, and $z = 0.5$ for $R = 6 \times 10^5, 8 \times 10^6, 2 \times 10^7$, and 3×10^7 , respectively. Here $\delta T(t) = T(t) - \bar{T}$ (\bar{T} is the mean temperature) and $\sigma_T^2 = \overline{T(t)^2} - (\bar{T})^2$, and time is measured in the units of eddy turnover time. The autocorrelation functions

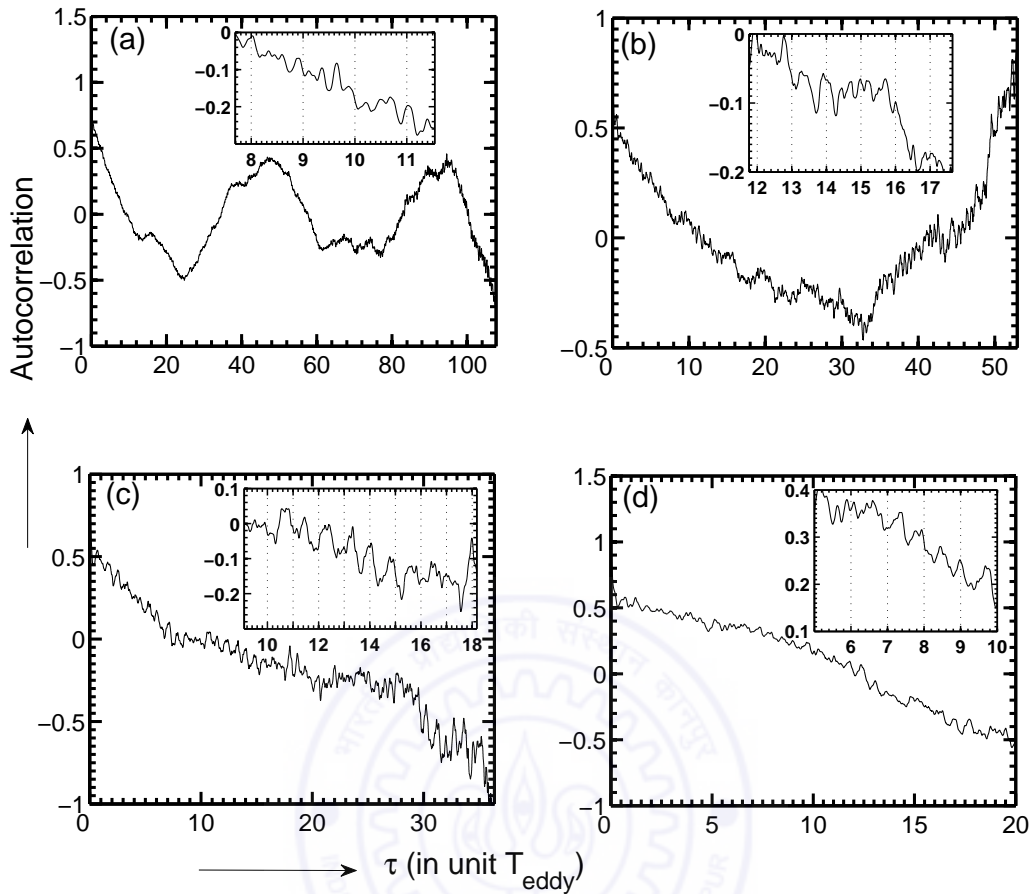


Figure 5.2: Plot of the autocorrelation function $g_c(\tau) = \langle \delta T(t) \delta T(t + \tau) \rangle / \sigma_T^2$ vs. delay time τ (in units of large eddy turnover time) for a probe at $r = 0.48$, $\theta = 0$, and $z = 0.5$: (a) $R = 6 \times 10^5$ on a $(33 \times 49 \times 97)$ grid, (b) $R = 8 \times 10^6$ on a $75 \times 96 \times 145$ grid, (c) $R = 2 \times 10^7$ on a $100 \times 120 \times 201$ grid, and (d) $R = 3 \times 10^7$ on a $100 \times 120 \times 201$ grid. The insets show oscillations on the eddy turn-over time scale. This Figure is taken from [131].

indicate two time scales in the system. Variations at the shorter time scale, shown in the insets, are due to the statistical return of the convective flow after one eddy turnover time or less (see Table 5.1). For $R = 6 \times 10^5$ and 8×10^6 , the oscillations are somewhat irregular. However for $R = 2 \times 10^7$ and 3×10^7 , the oscillations in the insets are quite regular, and the oscillation time period of the autocorrelation function is around one eddy turnover time. This is also evident from the plot of the cross-correlation function of the temperature between two azimuthally opposite probes placed at $\theta = 0$ and $\theta = \pi$, in the mid-plane ($z = 0.5$) at $r = 0.48$ (see Fig. 5.3). The cross-correlation function also shows

oscillations with approximately one eddy turnover time as the time period, which is in general agreement with the observations of Castaing *et al.* [80], Sano *et al.* [95], Qiu and Tong [94], and Xi *et al.* [86]. The above correlations are related to the peak in the power spectrum at frequency corresponding to $1/T_{eddy}$. The peak in the spectrum, however, tends to be overshadowed by noise. Consequently, the correlation function appears to be a good tool to analyze these oscillations. Note that the autocorrelation studies tend to become strongly periodic when the LSC direction is locked, e.g., by a small tilt of the cylinder [136].

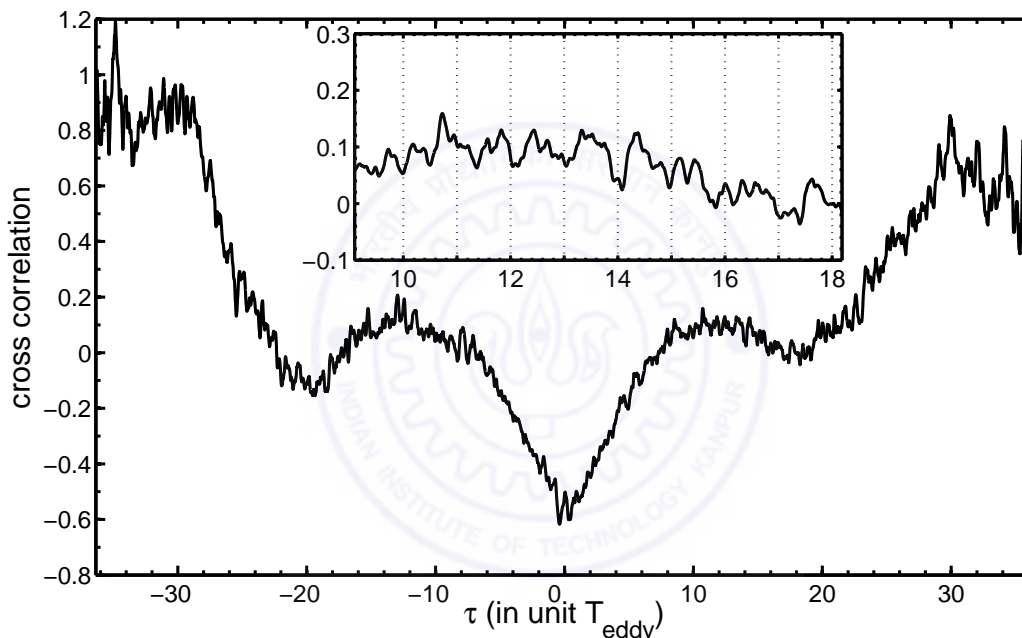


Figure 5.3: For $R = 2 \times 10^7$ on a $100 \times 120 \times 201$ grid, the cross-correlation function between the temperature measured at two azimuthally opposite probes at $\theta = 0$ and $\theta = \pi$ in the mid-plane at $r = 0.48$. The inset shows oscillations on the eddy turn-over time scale. This Figure is taken from [131].

In addition to the above, we observe variations in the above autocorrelation and cross-correlation functions at much larger time-scales. For $R = 6 \times 10^5$ (see Fig. 5.2(a)), there is a significant decrease in the correlations till $\tau \simeq 23T_{eddy}$, after which the correlations rise again to reach a maximum value at $\tau \simeq 46T_{eddy}$. These variations possibly correspond to the reorientations of the LSC. Similar features are observed for $R = 8 \times 10^6$ (see Fig. 5.2(b)). For $R = 2 \times 10^7$ and 3×10^7 , the auto-correlation functions decrease with

time (see Figs. 5.2(c,d)). Incidentally, the cross-correlation function for $R = 2 \times 10^7$ shows a minima at $\tau = 0$ and then at $\tau \approx 20T_{eddy}$, and a maximum at $\tau \approx 10T_{eddy}$, which possibly indicates reversals of the flow at $\tau \approx 10T_{eddy}$, and reoccurrence at $\tau \approx 20T_{eddy}$. We could not perform longer statistics since the computer simulations of the RBC flows for large Rayleigh numbers are computationally very expensive. The auto-correlation and cross-correlation function studies are inconclusive due to averaging, yet, the above observations indicate with some certainty that LSC exists in RBC. The reversal time could not be deduced from the present correlation functions.

The presence of LSC becomes more apparent when we study the time series of the velocity and temperature fields in the next sub-section.

5.3.2 Measure of reorientations of LSC

The time series of the vertical velocity field for $R = 6 \times 10^5, 8 \times 10^6$, and 2×10^7 recorded by the probes at $\theta_j = j\pi/4$ ($j = 0 : 7$), $r = 0.48$, and $z = 0.5$ are shown in Figs. 5.4, 5.5, and 5.6, respectively. Here, time is measured in the units of free-fall time ($d/\sqrt{\alpha g(\Delta T)d}$). The figures clearly show that the vertical velocity at probes θ_j and $(\theta_j + \pi) \bmod 2\pi$ are clearly anti-correlated. These observations indicate the presence of a large scale convective structure (see Figs. 5.1(b,c)). As shown in Figs. 5.4-5.6 the local mean value (in time) of the vertical velocity changes sign, and this feature is called the “reversal” of LSC in the literature.

In the following discussions, we will show that the above-mentioned reversals are connected to the “reorientations” of the LSC. To quantify the reorientations, we Fourier transform the vertical velocity field measured at $r = 0.48$ and $z = 0.5$. Note that these probes are near the lateral wall in the mid-plane. The velocity signal at a given probe

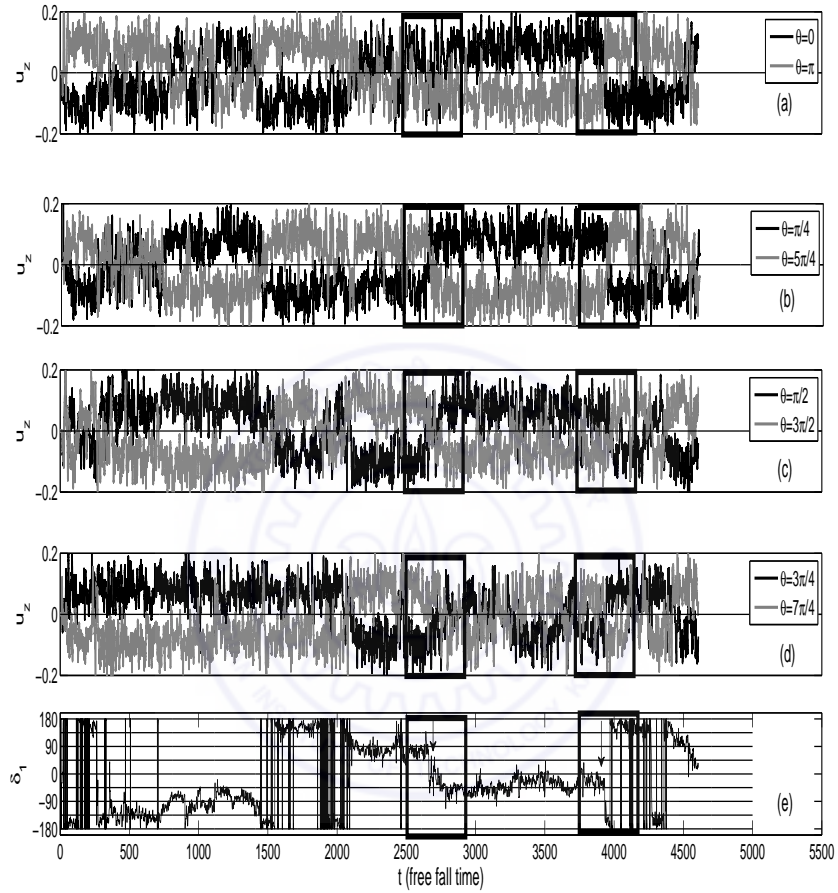


Figure 5.4: For $R = 6 \times 10^5$ on a $33 \times 49 \times 97$ grid, the time series of the vertical velocity measured by the probes at $z = 0.5$ (mid- plane) and $r = 0.48$ for: (a) $\theta = 0$ and $\theta = \pi$, (b) $\theta = \pi/4$ and $\theta = 5\pi/4$, (c) $\theta = \pi/2$ and $\theta = 3\pi/2$, and (d) $\theta = 3\pi/4$ and $\theta = 7\pi/4$. The time series of the phase of the first Fourier mode of the vertical velocity (δ_1) is shown in subfigure (e). Time is measured in units of the free-fall time $d/\sqrt{\alpha g(\Delta T)d}$. The arrows (inside the boxed regions) in (e) indicate a partial reorientation ($\delta_1 \simeq 135^\circ$) near $t \simeq 2700$, and a complete reversal ($\delta_1 = 180^\circ$) near $t \simeq 3900$. This Figure is taken from [131].

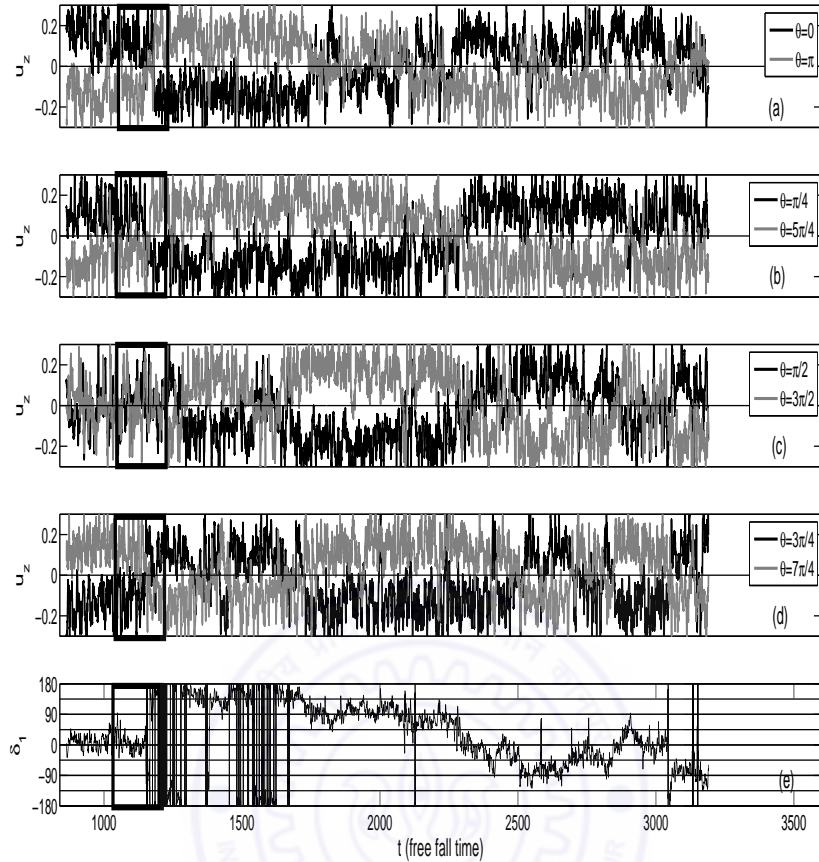


Figure 5.5: For $R = 8 \times 10^6$ on a $75 \times 96 \times 145$ grid, the time series of the vertical velocity measured by the probes at $z = 0.5$ (mid- plane) and $r = 0.48$, and the phase of the first Fourier mode of the vertical velocity. Details of the figures are the same as in Fig. 5.4. A complete reversal of the flow occurs in the boxed region. This Figure is taken from [131].

can be expressed in terms of its Fourier transform as

$$u_j(t) = \sum_{k=-4}^4 \hat{u}_k \exp(ik\theta_j) \quad (5.4)$$

$$= \sum_{k=-4}^4 |\hat{u}_k| \exp(ik\theta_j + \delta_k) \quad (5.5)$$

$$= u_{\text{mean}} + \sum_{k=1}^4 2|\hat{u}_k| \cos(k\theta_j + \delta_k), \quad (5.6)$$

where $\theta_j = j\pi/4$ ($j = 0 : 7$), and δ_k is the phase of the k -th Fourier mode. Note that the

reality condition $\hat{u}_{-k} = \hat{u}_k^*$ is used to derive Eq. (5.6). In our simulations, we observe that the first Fourier mode ($k = 1$) dominates over the other modes except possibly during the reversals. Note that Cioni *et al.* [81], and Brown and Ahlers [85] have analyzed the properties of $\hat{u}_1(t)$ and $\delta_1(t)$ using only their experimental data. In the later part of our discussion, we will compute the amplitudes of the Fourier modes using the vertical velocity fields measured by the probes at $z = 0.5$ and $r = 0.48$.

For quantitative analysis, Brown *et al.* [84] and Brown and Ahlers [85] proposed that the phase of the first Fourier mode δ_1 can be used as an approximate measure of the orientation of the plane of the LSC. Using this criteria, they defined “reorientation of the LSC” as a sudden and significant rotation of the plane containing the LSC. They used two selection criteria for the reorientation of the LSC: (a) the magnitude of the angular change in orientation $|\Delta\delta_1|$ should be greater $\pi/4$, and (b) the azimuthal rotation rate $|\dot{\delta}_1|$ should be greater than $\pi/(5T_{eddy})$, where T_{eddy} is the eddy turn-over time. We apply the same criteria for the selection of reorientation events in our simulations.

In Figs. 5.4-5.6 we plot the phase of the first Fourier mode (δ_1), which is a measure of the plane of the LSC. Note that the discontinuities from 180^0 to -180^0 in the δ_1 diagrams are not reorientations; they simply indicate jitters near 180 degree. In all the time series of the vertical velocity and the phase of the first Fourier mode plots, we observe that the mean value of the vertical velocity changes sign but not necessarily simultaneously for all the probes. For example, in Fig. 5.4, the vertical velocity u_z measured by all the probes reverse sign near $t \simeq 3900$ (the right boxed region of Fig. 5.4). This reorientation is a “complete reversal” of the LSC, and it corresponds to a change in δ_1 by around π , i.e., $\Delta\delta_1 \approx \pi$. Near $t \simeq 2700$ (the left boxed region of Fig. 5.4), however, u_z changes sign for all the probes except at $\theta = 0$ and π . This kind of reorientation will be termed as a “partial reversal”, and it corresponds to $\Delta\delta_1 \neq \pi$. Near $t \simeq 2700$, $\Delta\delta_1 \approx 135^0$. The time series shown in Figs. 5.4-5.6 exhibit several partial and complete reversals. For example, we observe complete reversals for $R = 8 \times 10^6$ and 2×10^7 in the boxed regions shown in the figures.

A careful analysis of the Fourier modes reveals that complete and partial reversals are intimately related to the changes in orientations of the convective structures by $\Delta\delta_1$.

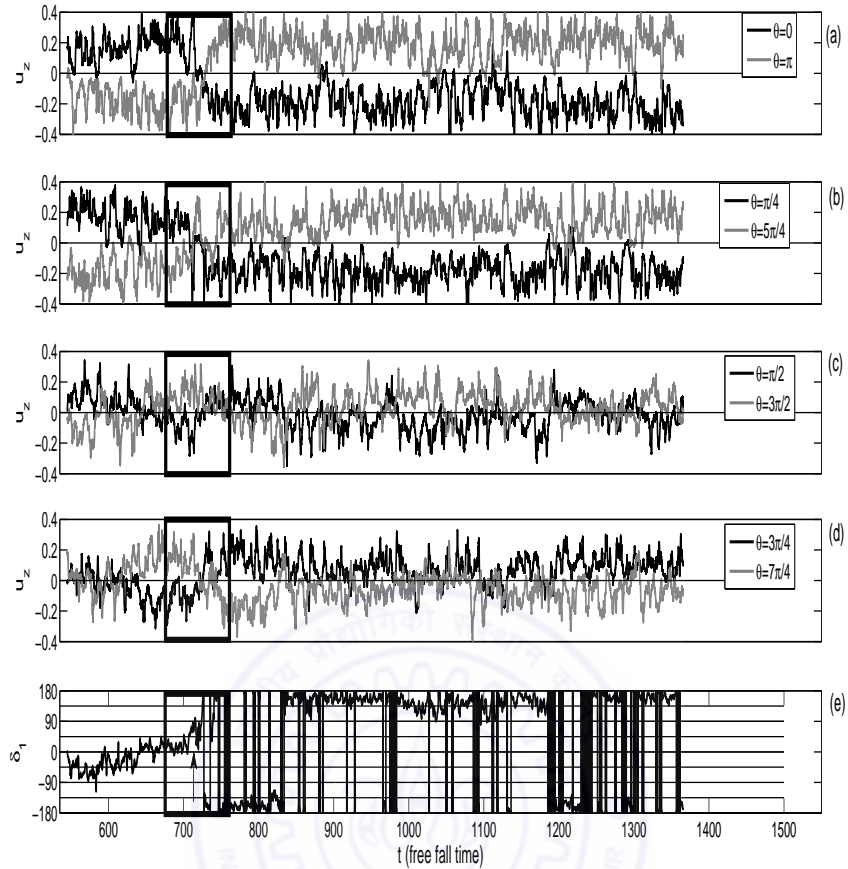


Figure 5.6: For $R = 2 \times 10^7$ on a $100 \times 120 \times 201$ grid, the time series of the vertical velocity measured by the probes at $z = 0.5$ (mid- plane) and $r = 0.48$, and the phase of the first Fourier mode of the vertical velocity. Details of the figures are the same as in Fig. 5.4. A complete reversal of the flow occurs in the boxed region. This Figure is taken from [131].

We take the real space u_z data before and after the reversals for the three cases marked with arrows in the δ_1 time series of Figs. 5.4 and 5.6. In Figs. 5.7(a,c,e) we illustrate the azimuthal profile of the vertical velocity at $z = 0.5$ and $r = 0.48$ before and after the reorientations as solid and dashed lines respectively. We calculate $\Delta\delta_1$, the change in the phase of the first Fourier mode, during the reorientations of the structures. If the convective structure rotates by an angle $\Delta\delta_1$ during a reorientation, then, according to Eq. (5.6), we can cancel the effects of this reorientation by subtracting $k\Delta\delta_1$ from the phases of all the positive k modes, and by adding $k\Delta\delta_1$ to all the negative k modes of the data recorded after the reorientation (Note that the $k = 0$ mode is left unaltered).

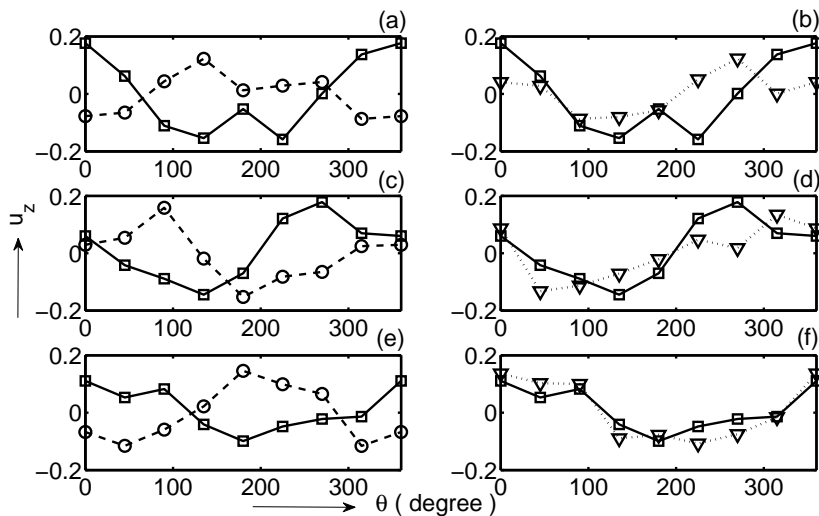


Figure 5.7: Azimuthal profile of the vertical velocity at $z = 0.5$ and $r = 0.48$ before (solid line) and after reorientation (dashed line): (a) $R = 2 \times 10^7$ at $t = 695$ & 750 , (c) $R = 6 \times 10^5$ at $t = 2548$ & 2850 , and (e) $R = 6 \times 10^5$ at $t = 3400$ & 4050 . During the reorientations the phase of the first Fourier mode changes by $\Delta\delta_1 = 180^\circ$, 135° , and 180° , respectively. For the reoriented time series, we subtract $\Delta\delta_1$ from the positive k modes, add $\Delta\delta_1$ to the negative k modes, and construct a modified velocity profile (dotted line). As seen in the sub-figures (b), (d), and (f), the reconstructed velocity profiles match quite well with the profiles before the reorientation. This Figure is taken from [131].

We perform the above exercise on the Fourier modes of the data sets recorded after the specified reversals or reorientations. Subsequently, we compute the velocity fields from the modified Fourier coefficients. The modified velocity fields, shown as dotted lines in Figs. 5.7(b,d,f), match quite well with the corresponding velocity profiles before the reorientations. Thus, we show that the convective structures essentially rotate by $\Delta\delta_1$ during the reorientations.

The above features of our simulations are in general agreement with the experimental results by Cioni *et al.* [81], Brown *et al.* [84], Brown and Ahlers [85], and Xi *et al.* [86]. Note that the numbers of reorientations in the convection experiments are much larger than those observed in numerical simulations. In the next subsections we analyze the detailed dynamics of the reorientation of LSC using numerical data.

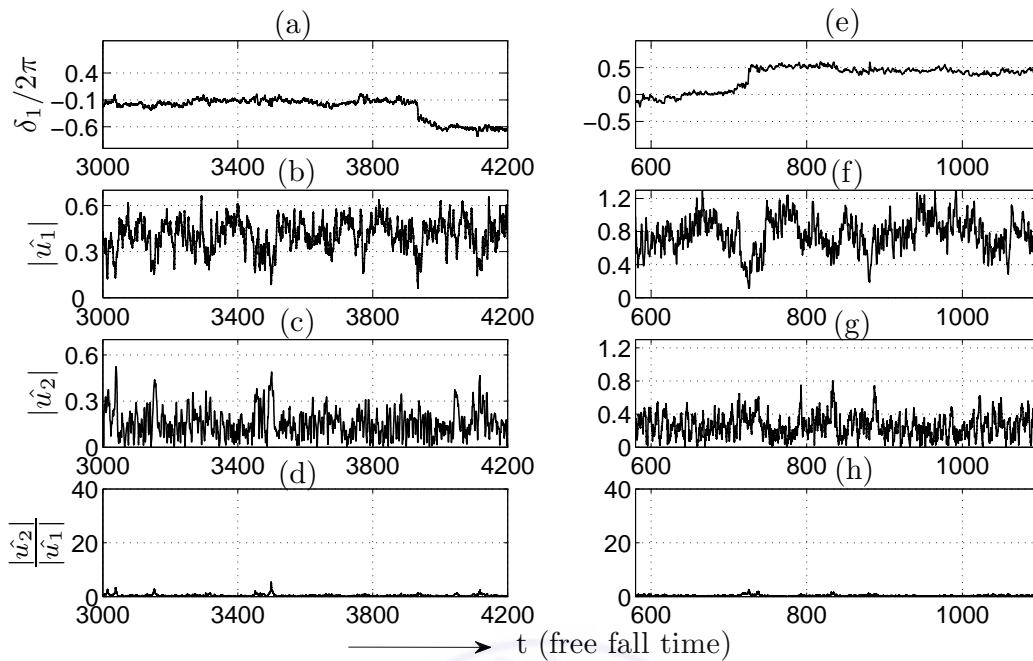


Figure 5.8: Time series of the phase of the first Fourier mode δ_1 (in units of 2π), amplitude of the first Fourier mode $|\hat{u}_1|$, and amplitude of the second Fourier mode $|\hat{u}_2|$ during the rotation-led reversals. Panels (a), (b), (c), and (d) show the time series of δ_1 , $|\hat{u}_1|$, $|\hat{u}_2|$, and $|\hat{u}_2|/|\hat{u}_1|$, respectively, for $R = 6 \times 10^5$ on a $33 \times 49 \times 97$ grid in which the reversal takes place near $t = 3950$. (e), (f), (g), and (h) show the time series of δ_1 , $|\hat{u}_1|$, $|\hat{u}_2|$, and $|\hat{u}_2|/|\hat{u}_1|$, respectively, for $R = 2 \times 10^7$ on a $100 \times 120 \times 201$ grid with a reorientation event near $t = 700$. This Figure is taken from [131].

5.3.3 Dynamics of reorientations

A careful analysis of the phases and amplitudes of the Fourier modes provides important clues about the dynamics of the reorientations of LSC and the reversals of the vertical velocity. The amplitudes of the Fourier modes vary significantly over time. We observe that during some of the reversals or reorientations, the amplitude of the first Fourier mode almost vanishes; these reorientations are termed as “cessation led”. In the other reorientations, which are termed as “rotation led”, the Fourier modes continue to fluctuate around their mean values. These kinds of reversals were reported by Brown *et al.* [84], Brown and Ahlers [85], and Xi *et al.* [86] based on their RBC experiments. In this subsection, we probe the dynamics of reversals using numerical simulations.

In Fig. 5.8, we plot the phases and amplitudes of the first two Fourier modes during two rotation-led reorientations. For $R = 6 \times 10^5$ Fig. 5.8(a) exhibits the time series of the

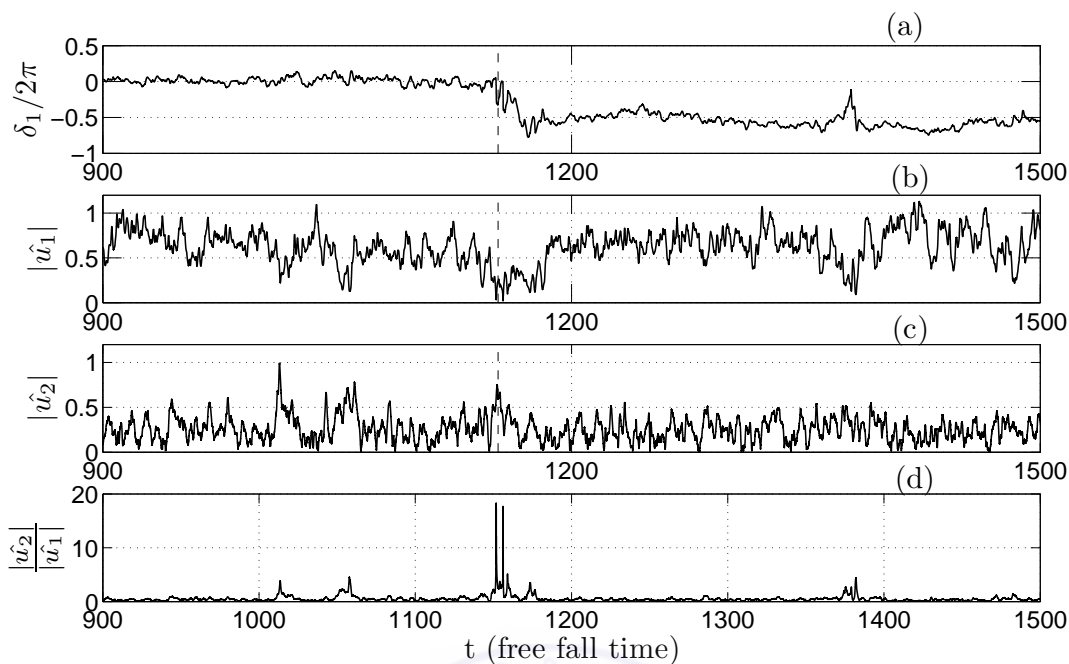


Figure 5.9: Time series of δ_1 , $|\hat{u}_1|$, $|\hat{u}_2|$, and $|\hat{u}_2|/|\hat{u}_1|$ indicating cessation-led reorientation near $t \sim 1175$ for $R = 8 \times 10^6$ on a $75 \times 96 \times 145$ grids. The strength of $|\hat{u}_1|$ decreases significantly, while $|\hat{u}_2|/|\hat{u}_1|$ increases during this event. This Figure is taken from [131].

phase $\delta_1/2\pi$ (i.e., in units of 2π). Figs. 5.8(b,c) show the amplitudes of the first and second Fourier modes $|\hat{u}_1|$ and $|\hat{u}_2|$, respectively, while Fig. 5.8(d) shows their ratio $|\hat{u}_2|/|\hat{u}_1|$. As shown in the figures, δ_1 changes by approximately π near $t \approx 3900$, but $|\hat{u}_1|$ and $|\hat{u}_2|$ continue to fluctuate around their average values. However, $|\hat{u}_1|$ always dominates over $|\hat{u}_2|$, as is evident from the plot of $|\hat{u}_2|/|\hat{u}_1|$ shown in Fig. 5.8(d). Figures 5.8(e,f,g,h) exhibit similar features for $R = 2 \times 10^7$. Note, however, that $|\hat{u}_1|$ tends to have a small dip during the reorientation, but $\Delta|\hat{u}_1|$ is much smaller as compared to the cessation-led reversals to be described later. Note that both the above events lead to “complete reversals” since $\Delta\delta_1 \approx \pi$.

In the other set of reversals or reorientations, we observe that the amplitude of the first Fourier mode $|\hat{u}_1|$ tends to vanish during the event. These sets of reversals were termed as “cessation led” by Brown *et al.* [84], Brown and Ahlers [85], and Xi *et al.* [86]. We illustrate the cessation-led reversals using the following examples.

Figs. 5.9(a) and 5.9(b) exhibit the time series plots of δ_1 and $|\hat{u}_1|$, respectively, for

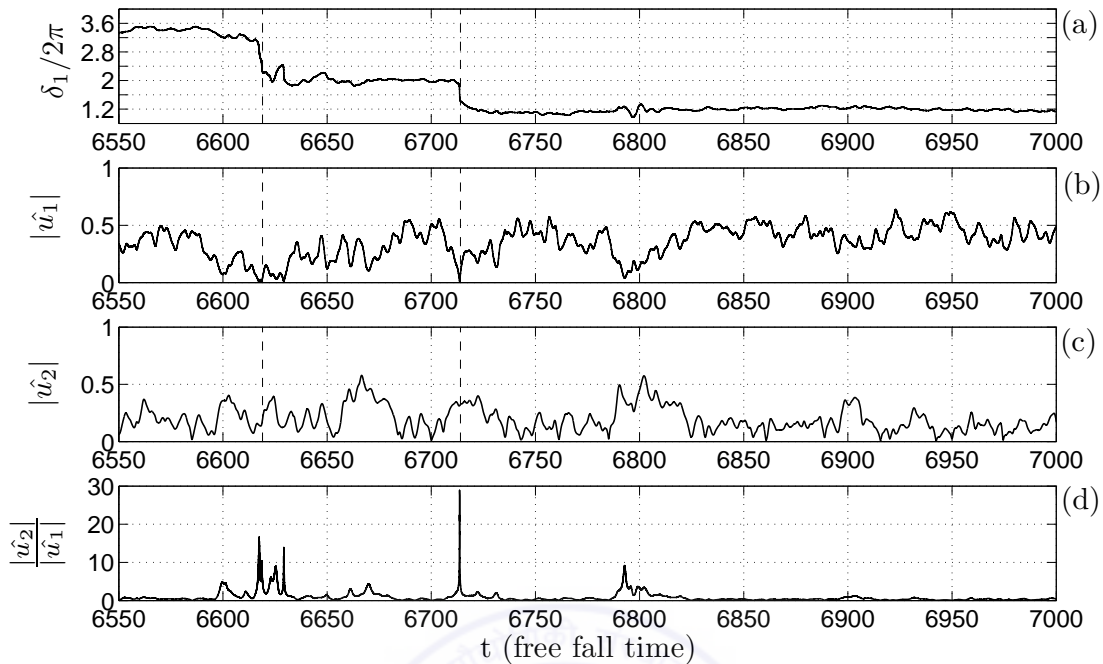


Figure 5.10: Time series of δ_1 , $|\hat{u}_1|$, $|\hat{u}_2|$, and $|\hat{u}_2|/|\hat{u}_1|$ indicating cessation-led partial reorientations near $t \sim 6625$ and 6710 for $R = 6 \times 10^5$ ($33 \times 49 \times 97$ grid). For both the events $\Delta\delta_1 \approx 72^\circ$. This Figure is taken from [131].

$R = 8 \times 10^6$. During the cessation at $t \sim 1175$, $\Delta\delta_1 \approx \pi$ and $|\hat{u}_1|$ tends to zero. The amplitude of the second Fourier mode $|\hat{u}_2|$ however increases slightly above its average value during this event (see Fig. 5.9(c)). The fluctuations in $|\hat{u}_1|$ and $|\hat{u}_2|$, however, tend to hide the above features. Therefore, we use $|\hat{u}_2|/|\hat{u}_1|$ to amplify the decrease in $|\hat{u}_1|$ and the increase in $|\hat{u}_2|$ to be able to identify the cessation-led reversals clearly. In Fig. 5.9(d), we plot $|\hat{u}_2|/|\hat{u}_1|$ which exhibits a sharp peak during the event. This is an example of cessation-led complete reversal since $\Delta\delta_1 \approx \pi$. Fig. 5.10 shows the corresponding quantities for another set of cessation-led reorientations for $R = 6 \times 10^5$. As is evident from the time series, near $t \sim 6620$, $\Delta\delta_1 \sim (3.2 - 2) * 2\pi \approx 72^\circ$. Later at $t \sim 6720$, $\Delta\delta_1 \sim (2 - 1.2) * 2\pi \approx -72^\circ$. These two reorientations as shown in Fig. 5.10 are partial ones, and the LSC comes back to its original configuration after the two reorientations ($\Delta\delta_1 = (3.2 - 1.2) * 2\pi$). During both these events $|\hat{u}_2|/|\hat{u}_1|$ has a sharp peak.

In our simulations, we also observe reorientations involving “double cessations”, first observed by Xi *et al.* [86] in their experiments. During these events, the phase δ_1 changes

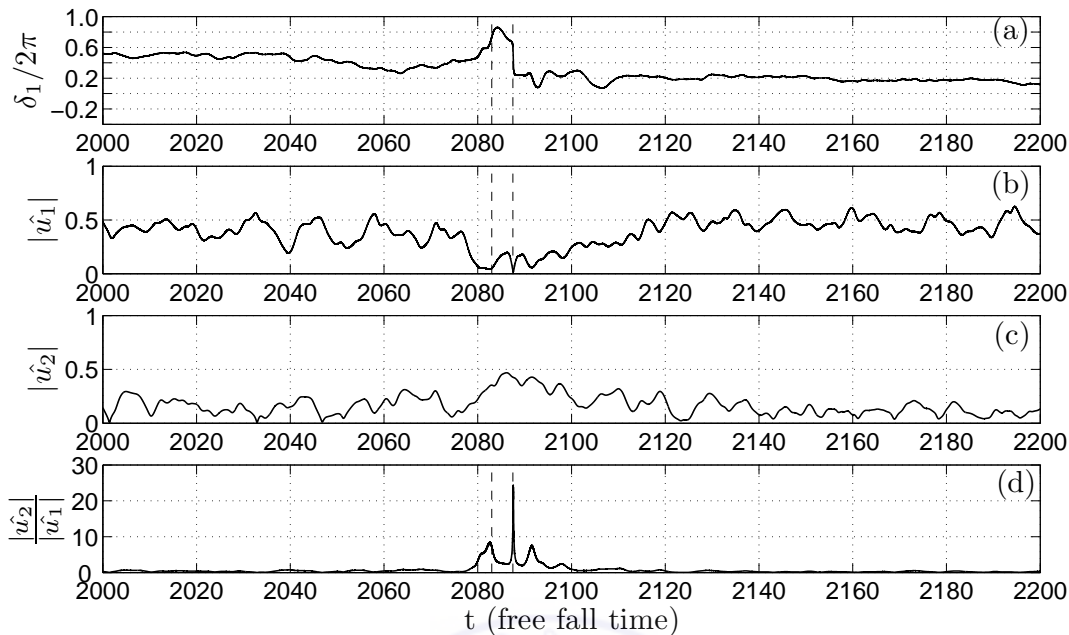


Figure 5.11: Time series of δ_1 , $|\hat{u}_1|$, $|\hat{u}_2|$, and $|\hat{u}_2|/|\hat{u}_1|$ indicating double-cessation for $R = 6 \times 10^5$ on a $33 \times 49 \times 97$ grid. The first cessation occurs at $t \sim 2083$ and second one occurs at $t \sim 2088$. During both the events, $|\hat{u}_1|$ becomes weak and $|\hat{u}_2|$ dominates. Panel (d) shows the two spikes in $|\hat{u}_2|/|\hat{u}_1|$ during these events. This Figure is taken from [131].

in two stages in quick succession, first by θ_1 and then by θ_2 . Therefore, the net $\Delta\delta_1 \approx \theta_1 + \theta_2$. During double cessation, $|\hat{u}_1|$ vanishes on two occasions separated by a small time gap (within an eddy turnover time), while $|\hat{u}_2|$ tends to increase during these times, hence, $|\hat{u}_2|/|\hat{u}_1|$ exhibits two peaks within a short time interval. Two independent double cessation events have been illustrated in Fig. 5.11(a) and Fig. 5.12(a) for $R = 6 \times 10^5$. In Fig. 5.11(a), we observe the first cessation at $t \approx 2083$ followed by the second cessation at $t \approx 2088$, with $\theta_1 \approx -\theta_2 \approx \pi$. In Fig. 5.12(a), the first cessation occurs at $t \approx 2464$ followed by the second cessation at $t \approx 2466$ with $\theta_1 \approx -\theta_2 \approx 0.8\pi$. Since the net change in the phase δ_1 is approximately zero, the final configuration of the LSC is similar to its original configuration. Note that one eddy turn over time for the corresponding run is approximately 26 free fall time (see Table 5.2). Hence, the two double-cessations occur within 0.2 and 0.08 eddy turnover time respectively, which is consistent with the experimental result of Xi *et al.* [86].

For $R = 6 \times 10^5$, we observe two events that are similar to the above-mentioned double-

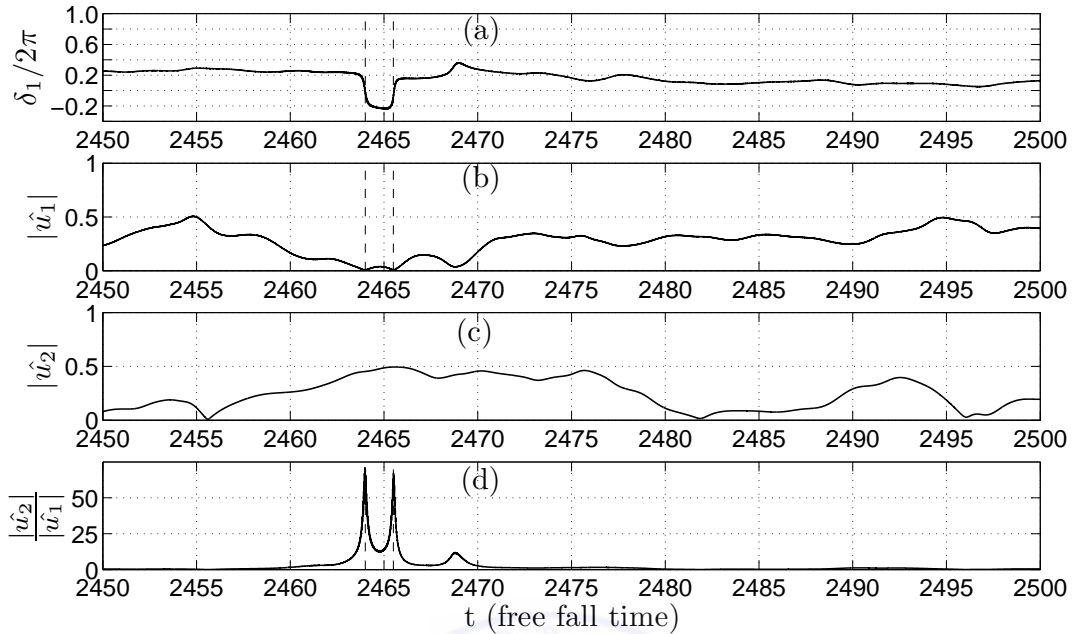


Figure 5.12: Time series of δ_1 , $|\hat{u}_1|$, $|\hat{u}_2|$, and $|\hat{u}_2|/|\hat{u}_1|$ indicating double-cessation for $R = 6 \times 10^5$ on a $33 \times 49 \times 97$ grid. The first cessation at $t \sim 2464$ is followed by the second at $t \sim 2466$. During both the events, $|\hat{u}_1|$ becomes weak and $|\hat{u}_2|$ dominates. Panel (d) shows the two spikes in $|\hat{u}_2|/|\hat{u}_1|$ during these events. This Figure is taken from [131].

cessation events (see Figs. 5.13(a,b,c,d)). Near $t \approx 4540$, δ_1 changes twice, $\theta_1 \approx 0.6\pi$ and $\theta_2 \approx -0.6\pi$ with a net $\Delta\delta_1 \approx 0$. These two events, however, occur very close to each other, and we observe only one peak for $|\hat{u}_2|/|\hat{u}_1|$, rather than any double peaks indicative of double-cessation. Another cessation-led reorientation occurs near $t \approx 4270$ which resembles the above-mentioned double-cessation event with the exception of one major difference. Here $\theta_1 \approx 0.8\pi$ and $\theta_2 \approx -0.6\pi$, and hence, the LSC reorients by a net non-zero angle after the event. Note that for the double cessation reported by Xi *et al.* [86], $\theta_1 \approx -\theta_2$ and the net change in δ_1 is zero. In our numerical simulations, we do find such events. In addition we also observe a double cessation where $\theta_1 \neq -\theta_2$, and the LSC reorients by a finite angle after the event.

Figure 5.14 illustrates the distribution of $\Delta\delta_1$ in the large scale circulations observed in our numerical simulations. We observe three complete reorientations ($\Delta\delta_1 \approx \pi$) of which two are rotation-led while the third is cessation-led. The number of observed partial reorientations is rather large with total of a 19. Among the partial reorientation events,

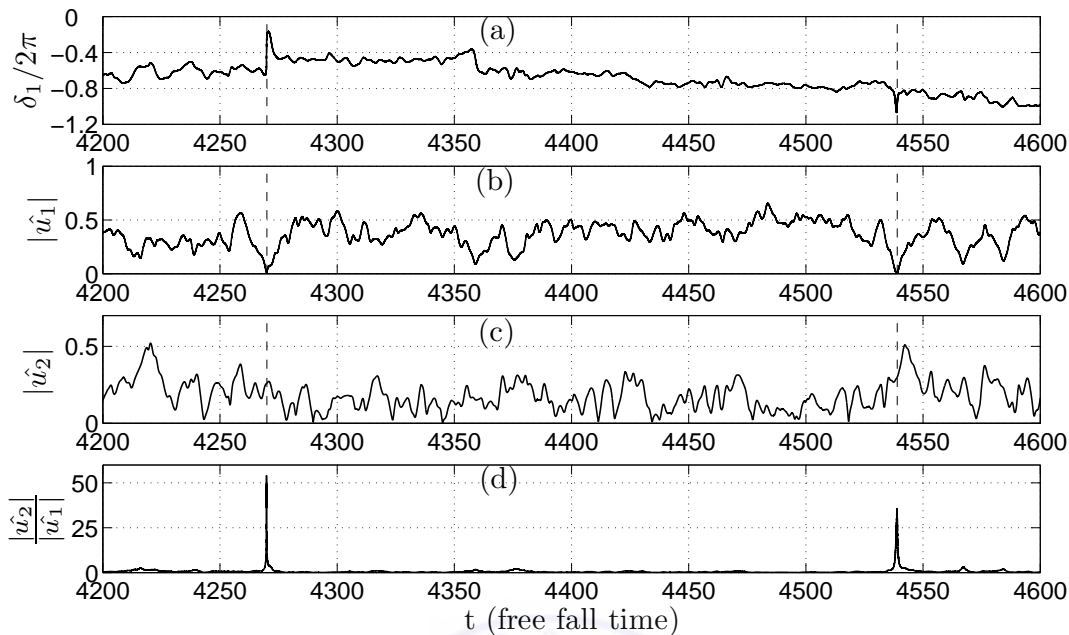


Figure 5.13: Time series of δ_1 , $|\hat{u}_1|$, $|\hat{u}_2|$, and $|\hat{u}_2|/|\hat{u}_1|$ for $R = 6 \times 10^5$ depicting events similar to double cessations on a $33 \times 49 \times 97$ grid. $\Delta\delta_1 \sim 72^\circ$ near $t \sim 4270$, while $\Delta\delta_1 \approx 0$ near $t \sim 4540$. During both the events, $|\hat{u}_1| \rightarrow 0$ while the ratio $|\hat{u}_2|/|\hat{u}_1|$ increases significantly. This Figure is taken from [131].

15 of them are rotation-led, while 4 of them are cessation-led. We also observe 4 double-cessations of which three have $\Delta\delta_1 \approx 0$ while the fourth has $\Delta\delta_1 \approx 0.2\pi$. The above observations indicate that cessation-led events are rarer as compared to the rotation-led ones, an observation consistent with that of Brown *et al.* [84], and Brown and Ahlers [85]. The number of reorientations observed in our simulations are far fewer as compared to those observed in the experiments of Brown *et al.* [84], Brown and Ahlers [85], Cioni *et al.* [81], and Xi *et al.* [86]. Consequently, we are unable to perform statistical studies of the reorientations similar to those performed by Brown *et al.* [84] and Brown and Ahlers [85].

In our numerical simulations we observe that the higher Fourier modes play an interesting role during reorientations. These kind of investigations were missing in earlier experimental works. We find that during the cessation-led reorientations, $|\hat{u}_2|$ tends to become significant while $|\hat{u}_1|$ tends to vanish. This feature is evident from the significant increase in the magnitude of $|\hat{u}_2|/|\hat{u}_1|$ during the cessation-led reorientations. Brown *et al.* [84], and Brown and Ahlers [85] interpret such events as cessation of the circula-

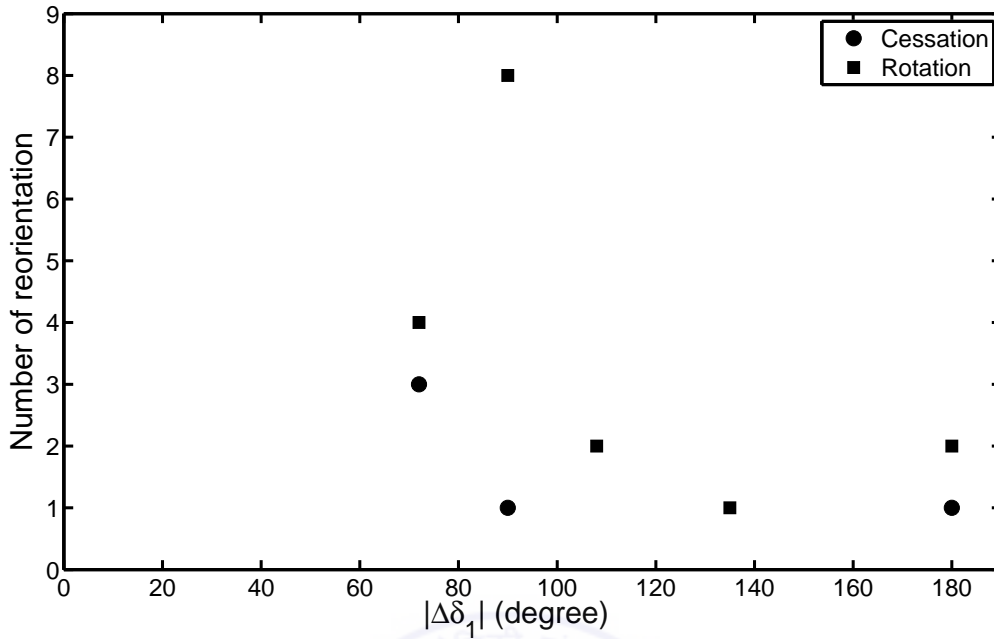


Figure 5.14: The distribution of the change in the phase of the first Fourier mode ($|\Delta\delta_1|$) of LSC during reorientations. The criteria of Brown *et al.* [84] and Brown and Ahlers [85] have been used for identifying reorientations of the LSC. This Figure is taken from [131].

tion, followed by a restart in a randomly chosen new direction. Our simulation results are consistent with the above interpretation, yet show that another scenario is also possible. During the cessation, the circulation structure corresponding to \hat{u}_1 (dipolar in a horizontal plane) becomes very weak, while the quadrupolar structure corresponding to \hat{u}_2 becomes dominant. After the cessation, the quadrupolar structure disappears and the dipolar structure reappears with a shift in the azimuthal direction. These features have been illustrated in Fig. 5.15 in which we show the horizontal profile of the temperature in the $z = 0.5$ plane before, during, and after two cessation-led reorientations for $R = 6 \times 10^5$. Figures 5.15(a,b,c) represent the temperature snapshots near a double cessation event (near $t = 2100$ of Fig. 5.11). The system starts from a \hat{u}_1 dominant state with approximate profile as $\cos(\theta + \delta_1)$ of Fig. 5.15(a). During the cessation, the system profile appears as Fig. 5.15(b) which has \hat{u}_2 as the most prominent Fourier mode with profile as $\cos(2\theta + \delta_2)$. After the double-cessation, the system returns to the \hat{u}_1 dominant structure as is evident from Fig. 5.15(c). Similar features are observed for another cessation-led

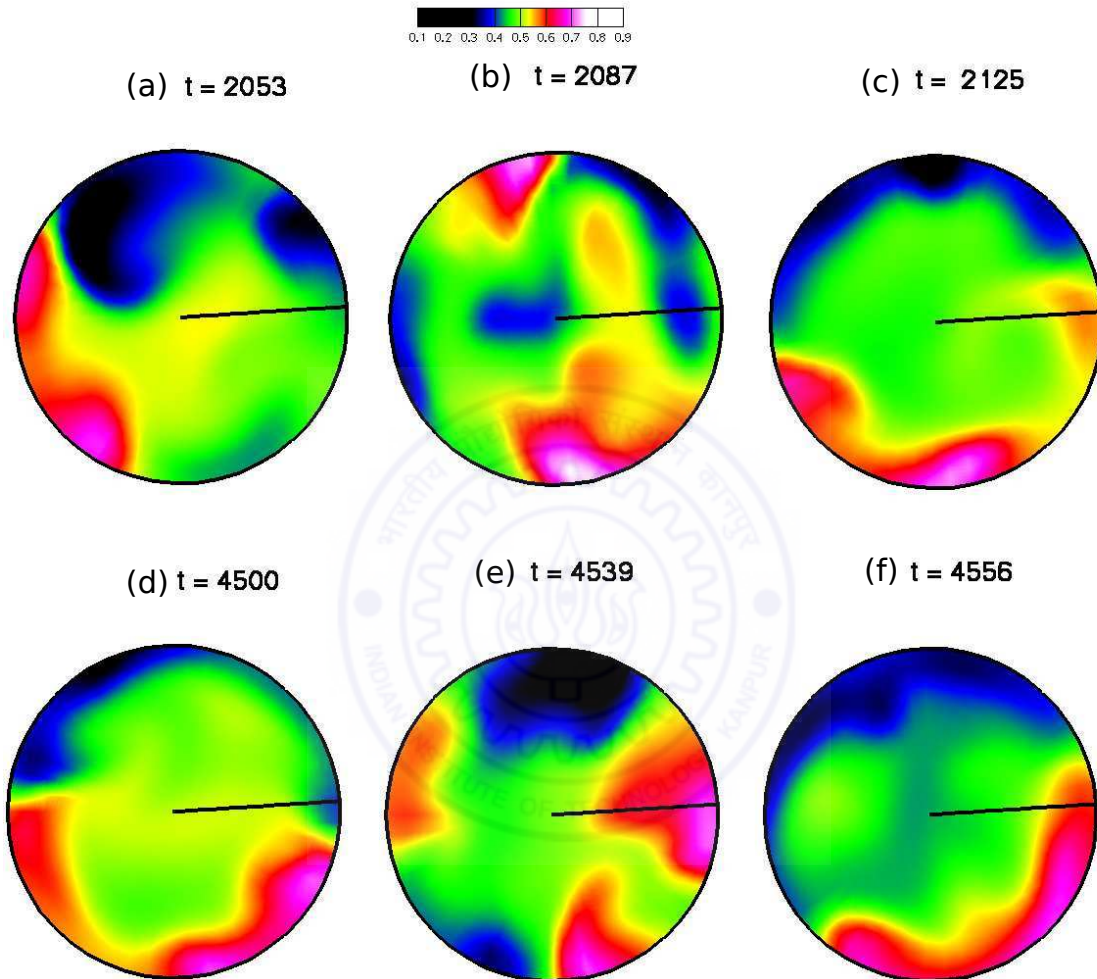


Figure 5.15: Temperature snapshots at the mid-plane ($z = 0.5$) during cessation-led reorientations near $t \sim 2087$ and 4539 for $R = 6 \times 10^5$. Dipolar structures are dominant before and after the reorientations, but quadrupolar structures are prominent during the reorientations (at $t = 2087$ & 4539). The horizontal black lines are drawn as a reference line which provide a guide to the azimuthal reorientations of the convective structure. This Figure is taken from [131].

reorientation near $t \approx 4500$ for $R = 6 \times 10^5$ as shown in Figs. 5.15(d,e,f). Note that in the rotation-led reorientations, the dipolar structure continues to be dominant during the reorientation itself.

In this section, we presented some of the complex dynamics of the reorientations of LSC. The reversals of the vertical velocity were shown to be intimately related to the reorientations of LSC. We observed rotation-led and cessation-led reorientations, which were first reported by Brown *et al.* [84] and Brown and Ahlers [85], and observed later in other experiments [86, 91, 93]. In our simulations, we encountered double cessation, previously observed by Xi *et al.* [86]. A new feature of our simulation was a double cessation in which the orientation of the LSC after the event was different from the original orientation. In our analysis, we studied higher Fourier modes, notably \hat{u}_2 , which were missing in earlier works on reversals. We proposed a new interpretation of the cessation-led reorientations, and argued that the LSC transformed from the dipolar (\hat{u}_1 dominant) to the quadrupolar (\hat{u}_2 dominant) structure, and then back to the dipolar (\hat{u}_1 dominant) structure during this event.

5.4 Discussion and conclusions

In this chapter, we numerically analyzed the dynamics of reorientations and reversals of LSC for air ($P = 0.7$) contained in a cylindrical container of aspect ratio one. We varied the Rayleigh number in the range of 6×10^5 to 3×10^7 . We observed that the dynamics of LSC could be captured quite well by the first Fourier mode of the vertical velocity measured near the lateral surface in the mid-plane of the container. The phase and amplitude of the first Fourier mode (δ_1) were used as a measure of the orientation and strength of the LSC respectively. We observed that the LSC occasionally reorients itself by rotating along the azimuthal direction by an arbitrary angle. When the reorientation angle was around π , the vertical velocity at *all* probes changed sign signaling a complete reversal of the flow. A partial reversal was observed when the reorientation angle was less than π .

We observed two kinds of reorientations: (a) rotation-led, and (b) cessation-led, earlier

observed by Brown *et al.* [84], Brown and Ahlers [85], and Xi *et al.* [86]. The rotation-led reversals involved the rotation of the LSC without any appreciable reduction in circulation strength, i.e., the amplitude of $|\hat{u}_1|$ remained finite. In the cessation-led reversals, $|\hat{u}_1|$ tended to zero, which was interpreted by Brown *et al.* [84], and Brown and Ahlers [85] as a cessation of the circulation followed by a restart in a randomly chosen new direction. During this event, we found that the ratio of the amplitude of the second Fourier mode to the first Fourier mode, i.e., $|\hat{u}_2|/|\hat{u}_1|$, increased significantly, and then it came back to its original level. These properties of the Fourier modes revealed that during the cessation, the LSC transformed from a dipolar-like structure to a quadrupolar-like structure, and then back to a dipolar-like structure. These features appear to have certain similarities with the reversals of the magnetic field in a dynamo [137]. The role of the higher Fourier modes in the reversals and reorientations of LSC have been highlighted in our simulations for the first time.

We also observed double-cessation-led reorientations of LSC. Xi *et al.* [86] had observed in their experiments that the LSC returns to its original orientation (approximately) after a double cessation. We, however, found in our numerical simulations that the change of the orientations of the LSC during some double cessations is zero, while in some others, the changes are non-zero.

We were able to reproduce many features (“rotation-led reorientations”, “cessation-led reorientations”, “double-cessations”, etc.) observed in convection experiments by Cioni *et al.* [81], Brown *et al.* [84], Brown and Ahlers [85], Xi *et al.* [86], and Niemela *et al.* [82] for Rayleigh numbers greater than those in our simulations. Several researchers have argued that the reorientations, including the reversals, of LSC occur only in strong turbulence regimes, say for $R > 10^8$. We, however, observe that the nature of the convective flows and reorientations are very similar for the range of Rayleigh numbers studied by us ($R = 6 \times 10^5$ to $R = 3 \times 10^7$). The lowest Rayleigh number that we have chosen, $R = 6 \times 10^5$, is probably in the weak turbulence regime where the LSC is not well-organized, and $R = 3 \times 10^7$, the highest Rayleigh number that we have chosen, is at the lower end of the strong turbulence regime. We could not carry out simulations for even larger Rayleigh numbers due to the very expensive computational requirements for these runs. However, we believe that the

reversals in the high Rayleigh number regimes are extremely likely to be similar to those presented in the simulations.

The next chapter summarizes the main conclusions of this thesis.



Chapter 6

Conclusions and future work

6.1 Main conclusions of the thesis

In this thesis, we have performed numerical and phenomenological studies on instabilities and turbulence in Rayleigh-Bénard convection. In the instabilities regimes, we investigated the effects of Prandtl number (mainly low-Prandtl number and zero-Prandtl number) on various static and time-dependent competitive non-linear instabilities, and proposed a low-dimensional model to understand it through a bifurcation diagram. In the turbulent regime, we have investigated the two features: (i) nature of energy cascade in the inertial range and (ii) dynamics of large scale circulation. The main conclusions of our studies are as follows:

In **chapter 3** we have explored various flow patterns of low- P ($P = 0.0002, 0.002, 0.005, 0.02$) convection, and performed a detailed bifurcation analysis near the onset using direct numerical simulation and a related low-dimensional models. Using the most energetic modes of DNS, we have proposed a 30-mode low-dimensional for low- P convection. We find a good agreement between the low-dimensional models and DNS results. We find the chaotic nature of the flow near the onset for $P \lesssim 0.005$ convection, however, we observe no chaos for $P = 0.02$. We have carried out a comparative studies of low- P convections with zero- P convection [43], and show how the limiting behaviour of zero- P convection is obtained as P approaches to zero. We find that low- P and zero- P convection exhibit patterns, namely squares, asymmetric squares, oscillating asymmetric squares, relaxation oscillations, and

chaos. The bifurcation diagram of low- P convection is very similar to zero- P convection, except near the onset where 2D stationary rolls, and stationary and oscillatory asymmetric squares are observed for non-zero Prandtl number. However, the range of Rayleigh numbers for which the stationary 2D rolls and associated asymmetric patterns are observed shrinks towards the onset with a P^2 dependence as P is decreased. This result is consistent with the earlier numerical and phenomenological studies performed for free-slip boundary conditions.

In **Chapter 4** we numerically compute the energy spectra and fluxes on 512^3 grid in the inertial range of the convective turbulence for a wide range of Prandtl numbers: zero- P ($P = 0$), low- P ($P = 0.02, 0.2$), moderate- P ($P = 1$), and high- P ($P = 6.8$). We perform simulation in a 3-D box with isothermal and free-slip condition on the horizontal walls, and periodic conditions on the lateral walls. We find that the spectra and fluxes support the presence of Kolmogorov-Obukhov scaling for zero-Prandtl number and low-Prandtl number convection. However, we find the presence of Bolgiano-Obukhov scaling for high-Prandtl number convection. Our numerical results for $P = 1$ is rather inconclusive. Next we find that the entropy spectra for non-zero Prandtl number exhibit dual branches in the inertial range. We propose a phenomenological argument based on the mode-to-mode energy transfer and find that the upper branch mainly correspond to the mode $\theta_{0,0,2n}$, where subscript represents the wave vectors along the x -, y - and z -axis respectively. Moreover, we find that the upper branch shows a scaling k^{-2} that is consistent with our phenomenological arguments.

In **Chapter 5** we have numerically investigated the dynamics of large scale circulation (LSC), in particular related to the reversals and reorientation of the flow, for air ($P = 0.7$) contained in a cylindrical container in the turbulent regime of Rayleigh-Bénard convection. The dynamics of the LSC in the azimuthal direction is captured by the Fourier modes of the vertical velocity in the azimuthal direction. We show that the amplitude and phase of the first Fourier mode contain the information of the strength and orientation of the LSC. We find that the LSC oscillates with a time period approximately equal to one eddy turn over time for high Rayleigh number convection ($R = 2 \times 10^7$ and $R = 3 \times 10^7$), however for low Rayleigh number we find that the oscillation in LSC is not

so regular. This observation is consistent with earlier experimental results. We observe large time modulation in the correlation functions related to the reversals of LSC. We find both rotation-led and cessation-led reorientations in our simulation. During rotation-led reorientation the amplitude of first Fourier mode continue to dominate over the higher modes. However, during the cessation-led reorientation of the flow, our simulations indicate the dominance of second Fourier mode over the amplitude of the first Fourier mode. We also observe the double cessation led reorientations. These results are consistent with earlier experimental and numerical observations.

6.2 Scope for future work

RBC is a vast field. In the following discussions, we describe some of the problems in RBC which could be attempted using tools similar to used in this thesis. The main limitation of our low-dimensional model for low-P presented in Chapter 3 is the absence of the modes that generate the wavy instability along the axis of the roll [12, 13]. Recently Pal *et al.* [115] have proposed a 27-mode model for zero-P convection by considering the modes responsible for the wavy instabilities. The wavy instabilities are also observed in the laboratory experiments. Thus inclusion of modes (e.g. Z_{010}) related to the wavy instabilities in the present 30-mode low-dimensional model would provide the better picture of instabilities and patterns observed in the experiments for low-P convection. We have performed our studies for aspect ratio $2\sqrt{2} : 2\sqrt{2} : 1$. It would be interesting to study the effects of aspect ratio on the dynamics of different static and time-dependent instabilities. As laboratory experiments are performed under the rigid wall boundary condition. The similar bifurcation analysis for no-slip boundary conditions would provide the more quantitative picture of instabilities which are observed in the laboratory experiments.

For the study of energy spectra and fluxes in Chapter 4, we have considered the free-slip condition for velocity on the horizontal walls to reduce the effect of the viscous boundary layers. However, in a recent review article, Lohse and Xia [46] discussed that the boundary layers critically affect the cascade of energy. Thus it would be interesting to perform similar numerical investigations for no-slip boundary condition. Further we

have proposed a phenomenological arguments for the nature of energy cascade in the inertial range for zero- P convection and very low- P convection, and we find that Buoyancy remains significant for low wave number ($k \sim 1$) for $P = 0$ and $P = 0.02$ convection. As a consequence, KO scaling is expected in the inertial range of very low- P and zero- P convection. It would be interesting to compute these scalings for limiting cases such as for $P \rightarrow 0$ and $P \rightarrow \infty$ using field-theoretical techniques. We have ignored the effects of anisotropy and intermittency in our studies for spectra and fluxes. The quantitative analysis of energy transfer in different direction in Fourier space would provide the better picture of energy cascade in the inertial range. The further extensions of our work may be the calculation of exponents of higher order structure function which would provide more comprehensive picture of cascade of energy in the small scale of convective turbulence.

In Chapter 5, we have analyzed the dynamics of LSC for Rayleigh numbers ranging from 6×10^5 to 3×10^7 , which is lower than the Rayleigh number considered in the laboratory experiments. Therefore, the natural extension of this work would be the numerical investigations of the dynamics of LSC for high Rayleigh number regime that would provide more quantitative comparison between the experimental and numerical observations. Another interesting result of our thesis (Chapter 5) is the prediction of flow structure during the cessation-led reorientation of the LSC. We find that the dipolar structure of the LSC transforms to the Quadrupolar structure during cessation and again comes back to dipolar structure. It would be interesting to investigate these issues from the perspective of energy transfer from low-wave number modes to higher-wave number modes during cessation. Xi and Xia [93] showed in their experiment that for large aspect ratio container, the azimuthal motion of the vertical plane containing LSC remains confined in a smaller azimuthal region compared to the small aspect ratio container. Numerical investigations of these observations would provide clearer picture on this issue. One of the possible reason of the presence of both rotation-led and cessation-led reorientations in the cylindrical geometry is of the azimuthal symmetry of the container. However, the 3D rectangular container lack this symmetry. It would be interesting to investigate the reorientations of LSC in the rectangular container.

Appendix A

A.1 Entropy spectrum

In chapter 4, we found that the entropy spectra for some finite Prandtl numbers ($P = 0.02, 0.2, 1$, and 6.8) exhibit dual branches. In this appendix, we discuss the reasons for this behaviour. We start with the entropy equation for the $\theta(n, 0, n)$ mode, which is

$$\frac{\partial}{\partial t} \frac{|\theta(n, 0, n)|^2}{2} = T^\theta(n, 0, n) + \Re[u_3(n, 0, n)\theta^*(n, 0, n)] - \frac{1}{\sqrt{PR}}(n^2\pi^2 + n^2k_c^2)|\theta(n, 0, n)|^2 \quad (\text{A.1})$$

where $T^\theta(n, 0, n)$ is the nonlinear entropy transfer to the mode $\theta(n, 0, n)$, and $k_c = \pi/\sqrt{2}$. The second term in the RHS is the entropy production rate $P^\theta(n, 0, n)$ due to the vertical velocity, and the last term provides the dissipation rate of the entropy due to thermal diffusivity. The entropy equation for the $\theta(0, 0, n)$ mode is very similar. We compute $T^\theta(n, 0, n)$ and $P^\theta(n, 0, n)$ from the simulation data, and find these quantities to be highly variable (i.e, fluctuate greatly with time). Yet we compute them at a given instant of time in the steady state regime. In this regime, $\partial|\theta(n, 0, n)|^2/\partial t \simeq 0$, and the dissipation term is also quite small. In Table A.1, we list the numerical values of $T^\theta(n, 0, n)$, $T^\theta(0, n, n)$, $P^\theta(n, 0, n)$, and $P^\theta(0, n, n)$ at an instant. Clearly, $T^\theta \simeq -P^\theta$, indicating that the entropy generated by u_3 is transferred to the higher modes by non-linear transfer.

From Eq. (A.1) we can conclude that the $\theta(n, 0, n)$ mode gains energy through the entropy production term ($P^\theta(n, 0, n)$), and loses energy to other modes through non-linear entropy transfer ($T^\theta(n, 0, n)$). When we compute the energy transfer functions explicitly, we find that the dominant entropy transfer from the $\theta(n, 0, n)$ mode is to the $\theta(0, 0, 2n)$

Table A.1: For the high-P ($P = 6.8$) and low-P ($P = 0.2$) cases, the numerical values of the non-linear entropy transfer rates T^θ , entropy production rates P^θ , and the nonlinear entropy transfer rates $S(\mathbf{k}|\mathbf{p}|\mathbf{q})$ from the $\theta(0, 0, 2n)$ mode to the modes $\theta(n, 0, n)$ or $\theta(0, n, n)$. This Table is taken from [122].

Mode	$P = 6.8$			$P = 0.2$		
	T^θ	$S(\mathbf{k} \mathbf{p} \mathbf{q})$	P^θ	T^θ	$S(\mathbf{k} \mathbf{p} \mathbf{q})$	P^θ
(1,0,1)	-1.2×10^{-4}	-1.1×10^{-4}	1.1×10^{-4}	-1.3×10^{-3}	-2.7×10^{-3}	2.9×10^{-3}
(0,1,1)	-1.0×10^{-7}	-7.5×10^{-8}	7.5×10^{-8}	-3.1×10^{-4}	-3.4×10^{-4}	3.6×10^{-4}
(2,0,2)	-7.0×10^{-7}	-5.0×10^{-7}	5.5×10^{-7}	-2.5×10^{-6}	-2.6×10^{-5}	3.4×10^{-5}
(0,2,2)	-1.6×10^{-6}	-1.2×10^{-6}	1.3×10^{-6}	-6.1×10^{-5}	-4.9×10^{-5}	6.3×10^{-5}
(3,0,3)	3.0×10^{-7}	2.1×10^{-7}	-2.2×10^{-7}	-7.0×10^{-7}	-1.4×10^{-6}	2.3×10^{-6}
(0,3,3)	-1.0×10^{-7}	-9.3×10^{-8}	1.0×10^{-7}	-5.7×10^{-6}	-5.3×10^{-6}	9.2×10^{-6}
(4,0,4)	3.0×10^{-7}	-3.2×10^{-7}	3.5×10^{-7}	-8.0×10^{-7}	-1.0×10^{-6}	2.4×10^{-6}
(0,4,4)	-4.0×10^{-7}	-4.0×10^{-7}	3.9×10^{-7}	1.0×10^{-6}	-7.0×10^{-7}	-1.6×10^{-6}

mode. The “mode-to-mode energy transfer” formalism [124] provides us the entropy transfer rate from the $\theta(0, 0, 2n)$ mode to the $\theta(n, 0, n)$ mode with $\mathbf{u}(-n, 0, n)$ acting as a mediator, which is

$$\begin{aligned}
S(\mathbf{k}|\mathbf{p}|\mathbf{q}) &= -\Im\{2n\pi(-i)u_3(-n, 0, n)\theta(n, 0, n)\theta(0, 0, 2n)\} \\
&= 2n\pi\theta(0, 0, 2n)\Re[u_3^*(n, 0, n)\theta(n, 0, n)]
\end{aligned} \tag{A.2}$$

with $\mathbf{k} = (n, 0, n)$, $\mathbf{p} = (0, 0, 2n)$, and $\mathbf{q} = (-n, 0, n)$. The function $\Im()$ stands for the imaginary part of the argument. The above formula has been adopted from the mode-to-mode energy transfer formulae for Fourier bases to mixed bases used for the free-slip boundary conditions [Eqs. (2.1) - (2.3)].

We compute $S(\mathbf{k}|\mathbf{p}|\mathbf{q})$ using the numerical data at the same instant of time when we compute $T^\theta(n, 0, n)$, and compare it with $T^\theta(n, 0, n)$ and the entropy production. As evident from the entries of the Table A.1,

$$T^\theta(n, 0, n) \simeq S(n, 0, n|0, 0, 2n|-n, 0, n) \simeq -P^\theta(n, 0, n). \tag{A.3}$$

The formulae and relationships for $\theta(0, n, n)$ are very similar. The above numerical findings indicate that the most dominant entropy transfers to the $\theta(0, 0, 2n)$ mode occur from

the $\theta(n, 0, n)$ and $\theta(0, n, n)$ modes. Also, the approximate relationship $S(n, 0, n|0, 0, 2n| - n, 0, n) \simeq -P^\theta(n, 0, n)$ and the equivalent relationship for the $\theta(0, n, n)$ mode yield

$$\theta(0, 0, 2n) \simeq -\frac{1}{2n\pi}, \quad (\text{A.4})$$

which matches quite well with the simulation data for $P = 6.8$ and 0.2 (listed in Table 4.2). Using the above result we can immediately derive that

$$E^\theta(0, 0, 2n) \simeq \frac{1}{4\pi^2 n^2}, \quad (\text{A.5})$$

which matches well with the upper branch of the entropy spectrum as shown in Figs. 4.5, 4.8, 4.11, and 4.14. The lower branch of the entropy spectrum corresponds to the modes other than $\theta(0, 0, 2n)$. The dual branches appear to arise due to the free-slip boundary conditions, and they have been observed in the simulations by Vincent and Yuen [72] and Paul *et al.* [73]. Note that the dual branches in the entropy spectrum have not been reported for no-slip [75] and periodic boundary conditions [57, 58].

The above arguments that support $E^\theta(0, 0, 2n) \sim 1/n^2$ are essentially numerical and phenomenological which work for $P = 6.8$ and 1 . For lower Prandtl numbers, $T^\theta(n, 0, n)$ is not approximately equal to $S(n, 0, n|0, 0, 2n| - n, 0, n)$, possibly due to significant entropy transfers to other modes, or due to thermal diffusion. Note, however, that the above quantities are within a factor of two, consequently $\theta(0, 0, 2n) \simeq -\frac{1}{2n\pi}$ holds even for lower Prandtl number within a factor of two.

The dual branches in the entropy spectrum add complications to the energy fluxes discussed in the Chapter 4. The temperature modes on the upper branch have significantly higher entropy, but they are only a few in number. Hence, the non-linear energy transfers arising from the upper branch are possibly insignificant. The number of modes involved in the lower branch is quite large, and they are likely to provide the energy flux.

Bibliography

- [1] Chandrashekhar S., *Hydrodynamic and Hydromagnetic Stability* (Cambridge university Press, Cambridge) 1961.
 - [2] Busse F. H., in *Hydrodynamic Instabilities and the Transition to Turbulence*, edited by H. L. Swinney and J. P. Gollub, Topics in Appl. Phys., **45** (Springer, Berlin), pp. 97-137 (1985).
 - [3] Manneville P., *Instabilities, Chaos and Turbulence*, (Imperial College Press, London) 2004.
 - [4] Bhattacharjee J. K., *Convection and Chaos in fluids* (World Scientific, Singapore) 1987.
 - [5] Spiegel E. A., 'Thermal turbulence at very small Prandtl number', J. Geophys. Res. **67**, 3063 (1962).
 - [6] Krishnamurti R., and Howard L. N., 'Large-scale flow generation in turbulent convection', Proc. Natl. Acad. Sci. U.S.A. **78**, pp. 1981-1985 (1981).
 - [7] Busse F. H., in *Fundamentals of Thermal Convection Mantle Convection, Plate Tectonics and Global Dynamics*, edited by PELTIER W. R. (Gordon and Breach), pp. 23-95 (1989).
 - [8] Croquette V., 'Convective pattern dynamics at low Prandtl number: Part I.', Contemp Phys. **30**, pp. 113-133 (1989).
 - [9] Croquette V., 'Convective pattern dynamics at low Prandtl number: Part II', Contemp. Phys. **30**, pp. 153-171 (1989).
 - [10] Cross M. C. and Hohenberg P. C., 'Pattern formation outside of equilibrium', Rev. Mod. Phys. **65**, pp. 851-1112 (1993).
 - [11] Bodenschatz E., Pesch W., and Ahlers G., 'Recent developments in Rayleigh-Bénard Convection', Annu. Rev. Fluid Mech. **32**, pp. 709-778 (2000).
 - [12] Thual O., 'Zero-Prandtl number convection', J. Fluid Mech. **240**, pp. 229-258 (1992).
 - [13] Busse F. H., 'The oscillatory instability of convection rolls in a low Prandtl number fluid', J. Fluid Mech. **52**, pp. 97-112 (1972).
-

- [14] Libchaber A. and Marurer J., 'Nonlinear Phenomena at Phase Transition Instabilities', Nato Advanced Study Series **B** (Ed. T. Riste), p.259 (Plenum: New York) (1981).
- [15] Busse F. H. and Bolton E. W., 'Instabilities of convection rolls with stress-free boundaries near threshold', *J. Fluid Mech.* **146**, pp. 115-125 (1984).
- [16] Ozoe H. and Hara T., 'Numerical analysis for oscillatory natural convection of low-Prandtl number fluid heated from below', *Num. Heat Transfer A* **27**, pp. 307-317 (1995).
- [17] Clever R. M. and Busse F. H., 'Transition to time-dependent convection', *J. Fluid Mech.* **65**, pp. 625-645 (1974).
- [18] Newell A. C., Passot T., and Soul M., 'The phase diffusion and mean drift equations for convection at finite Rayleigh numbers in large containers', *J. Fluid Mech.* **220**, pp. 187-252 (1990).
- [19] Newell A. C. and Whitehead J. A. 'Finite bandwidth, finite amplitude convection', *J. Fluid Mech.* **38**, pp. 279-303 (1969).
- [20] Segel L. A., 'Distant side-walls cause slow amplitude modulation of cellular convection', *J. Fluid Mech.* **38**, pp. 203-224 (1969).
- [21] Siggia E. D. and Zippelius A., 'Patterns selection in Rayleigh-Bénard convection near threshold', *Phys. Rev. Lett.* **47**, pp. 835-838 (1981).
- [22] Zippelius A. Siggia E. D., 'Disappearance of stable convection between free-slip boundaries', *Phys. Rev. A* **26**, pp. 1788-1790 (1982).
- [23] Zippelius A. and Siggia E. D., 'Stability of finite-amplitude convection', *Phys. Fluids*, **26**, pp. 2905-2915 (1983).
- [24] Bolton E. W. and Busse F. H., 'stability of convection rolls in a layer with stress-free boundaries', *J. Fluid Mech.* **150**, pp. 487-498 (1985).
- [25] Fauve S., Bolton E. W. and Brachet M. E., 'Nonlinear oscillatory convection: A quantitative phase dynamics approach', *Physica D* **29**, 202 (1987).
- [26] Jenkins D. R. and Proctor M. R. E., 'The transition from roll to square-cell solutions in Rayleigh-Bénard convection', *J. Fluid Mech.* **139**, pp. 461-471 (1984).
- [27] Willis G. E. and Deardorff J. W., 'The oscillatory motions of Rayleigh convection', *J. Fluid Mech.* **44**, pp. 661-672 (1970).
- [28] Rossby H. T., 'A study of Bénard convection with and without rotation', *J. Fluid Mech.* **36**, pp. 309-335 (1969).
- [29] Krishnamurti R., 'On the transition to turbulent convection. Part2. The transition to time-dependent flow', *J. Fluid Mech.* **42**, pp. 309-320 (1970); Krishnamurti R., 'Some further studies on the transition to turbulent convection', *J. Fluid Mech.* **60**, 285 (1973).
-

- [30] Lipps F. B., 'Numerical simulation of three-dimensional Bénard convection in air', *J. Fluid Mech.* **75**, pp. 113-148 (1976).
- [31] Clever R. M. and Busse F. H., 'Convection at very low Prandtl numbers', *Phys. Fluids A* **2** (3), pp. 334-339 (1990).
- [32] Meneguzzi M. *et al.*, 'Three-dimensional numerical simulation of convection in low Prandtl number fluid', *J. Fluid Mech.* **182**, pp. 169-191 (1987).
- [33] Lorenz E. N., 'Deterministic non-periodic flow', *J. Atmos. Sci.* **20**, pp. 130-141 (1963).
- [34] McLaughlin and Martin P.C., 'Transition to turbulence in a statically stressed fluid system', **12**, pp. 186-203 (1975).
- [35] Curry J. H., 'A generalized Lorenz model', *Comm. Math. Phys.* **60**, pp. 193-204 (1978).
- [36] Yahata H., 'Transition to turbulence in the Rayleigh-Bénard convection', *J. Phys. Soc. Jpn.* **68**, pp. 1070-1081 (1982).
- [37] Yahata H., 'Period-doubling cascade in the Rayleigh-Bénard convection', *J. Phys. Soc. Jpn.* **69**, 1802 (1983).
- [38] P. K., Wahi P., and Verma M. K., 'Patterns and bifurcations for low-P Rayleigh-Bénard convection', *Europhys. Lett.* **89**, 44003 (2010).
- [39] Kumar K., Fauve S., and Thual O., 'Critical self-tuning: the example of zero Prandtl number convection', *J. Phys. II (France)* **6**, pp. 945-951 (1996).
- [40] Herring J. R., 'Convection at zero-Prandtl number', *Woods Hole Oceanogr. Inst. Tech. Rep. WHOI-70-01*, (1970).
- [41] Kumar K., Pal P., and Fauve S., 'Critical bursting', *Europhys. Lett.* **74**, pp. 1020-1026 (2006).
- [42] Pal P. and Kumar K., 'Wavy strips and squares in zero-Prandtl number convection', *Phys. Rev. E* **65**, 047302 (2002).
- [43] Pal P., Wahi P., Paul S., Verma M. K., Kumar K., and Mishra P. K., 'Bifurcations and chaos in zero-Prandtl number convection', *Europhys. Lett.* **87**, 54003 (2009).
- [44] Kolmogorov A. N., 'Dissipation of energy in locally isotropic turbulence', *Dokl. Akad. Nauk SSSR* **32**, pp. 16-18 (1941).
- [45] Siggia E. D., 'High Rayleigh number Convection', *Annu. Rev. Fluid Mech.* **26**, pp. 137-168 (1994).
- [46] Lohse D. and Xia K. Q., 'Small-Scale Properties of Turbulent Rayleigh-Bénard Convection' *Annu. Rev. Fluid Mech.* **42**, pp. 335-364 (2010).
-

- [47] Bolgiano R. Jr., 'Turbulent spectra in a stably stratified atmosphere', *J. Geophys. Res.* **64**, pp. 2226-2229 (1959).
- [48] Obukhov A. M., *Dokl. Akad. Nauk SSSR* **125**, 1246 (1959).
- [49] Procaccia I. and Zeitak R., 'Scaling exponents in nonisotropic convective turbulence', *Phys. Rev. Lett.* **62**, pp. 2128-2131 (1989).
- [50] L'vov V. S., 'Spectra of velocity and temperature fluctuations with constant entropy flux of fully developed free-convective turbulence', *Phys. Rev. Lett.* **67**, 687 (1991).
- [51] Falkovich G. and L'vov V. S., 'Conservation laws and two-flux spectra of hydrodynamic convective turbulence', *Physica D* **57**, pp. 85-95 (1992).
- [52] Grossmann S. and L'vov V. S., 'Crossover of spectral scaling in thermal turbulence', *Phys. Rev. E* **47**, pp. 4161-4168 (1993).
- [53] Chillá F. *et al.*, 'Boundary Layer and Scaling Properties in Turbulent Thermal Convection', *Nuovo Cimento D* **15**, pp. 1229-1249 (1993).
- [54] Shraiman B. I. and Siggia E. D., 'Heat transport in high-Rayleigh-number convection', *Phys. Rev. A* **42**, 3650 (1990).
- [55] Grossmann S. and Lohse D., 'Scaling in thermal convection: A unifying view', *J. Fluid Mech.* **407**, 27 (2000).
- [56] Calzavarini E., Toschi F., and Tripicciono R., 'Evidences of Bolgiano-Obukhov scaling in three-dimensional Rayleigh-Bénard convection', *Phys. Rev. E* **66**, 016304 (2002).
- [57] Borue V. and Orszag S. A., 'Turbulent Convection Driven by a Constant Temperature Gradient', *J. Sci. Comput.* **12**, pp. 305-351 (1997).
- [58] Škandera D., Busse A., and Müller W. C., 'Scaling Properties of Convective Turbulence', *High Performance computing in science and engineering, Transactions of the Third joint HLRB and KONWIHR status and result workshop, Springer Berlin, Part IV*, 387 (2008).
- [59] Chillá F. *et al.*, 'Spectra of Local and Averaged Scalar Fields in Turbulence', *Europhys. Lett.* **22**, 23 (1993).
- [60] Mashiko T. *et al.*, 'Instantaneous measurement of velocity fields in developed thermal turbulence in mercury', *Phys. Rev. E* **69**, 036306 (2004).
- [61] Sun C., Zhou Q., and Xia K. Q., 'Cascades of Velocity and Temperature Fluctuations in Buoyancy- Driven Thermal Turbulence', *Phys. Rev. Lett.* **97**, 144504 (2006).
- [62] Zhou S. Q. and Xia K.Q., 'Scaling properties of the temperature field in convective turbulence', *Phys. Rev. Lett.* **87**, 06451 (2001).
-

- [63] Shang X. D. and Xia K. Q., 'Scaling of the velocity power spectra in turbulent thermal convection', *Phys. Rev. E* **64**, 065301 (2001).
- [64] Heslot F. *et al.*, 'Scaling of hard thermal turbulence in Rayleigh-Bénard convection', *J. Fluid Mech.* **204**, pp. 1-30 (1989).
- [65] Castaing B., 'Scaling of Turbulent Spectra', *Phys. Rev. Lett.* **65**, 3209 (1990).
- [66] Wu X. Z. *et al.*, 'Frequency power spectrum of temperature fluctuations in free convection', *Phys. Rev. Lett.* **64**, 2140 (1990).
- [67] Ashkenazi S. and Steinberg V., 'Spectra and Statistics of Velocity and Temperature Fluctuations in Turbulent Convection', *Phys. Rev. Lett.* **83**, 4760 (1999).
- [68] Niemela J. J. *et al.*, 'Turbulent convection at very high Rayleigh numbers', *Nature (London)* **404**, 837 (2000).
- [69] Cioni S., Ciliberto S., and Sommeria J., 'Temperature Structure Functions in Turbulent Convection at Low Prandtl Number', *Euophys. Lett.* **32**, 413 (1995).
- [70] Grossmann S. and Lohse D., 'Fourier-Weierstrass Mode Analysis for Thermally Driven Turbulence', *Phys. Rev. Lett.* **67**, 445 (1991).
- [71] Grossmann S. and Lohse D., 'Scaling in hard turbulent Rayleigh-Bénard flow', *Phys. Rev. A* **46**, 903 (1992).
- [72] Vincent A. P. and Yuen D. A., 'Plumes and waves in two-dimensional turbulent thermal convection', *Phys. Rev. E* **60**, 2957 (1999).
- [73] Paul S., Mishra P. K., Verma M. K., and Kumar K., 'Order and chaos in two-dimensional Rayleigh-Bénard convection', *Arxiv:0904.2917v1* (2009).
- [74] Rincon F., 'Anisotropy, inhomogeneity, and inertial-range scalings in turbulent convection', *J. Fluid Mech.*, **563**, pp. 43-69 (2006).
- [75] Kerr R. M., 'Rayleigh number scaling in numerical convection', *J. Fluid Mech.* **310**, pp. 139-179 (1996).
- [76] Camussi R. and Verzicco R., *European Journal Of Mechanics B*, 'Temporal statistics in high Rayleigh number convective turbulence', **23**, 427 (2004); Verzicco R. and Camussi R., *J. Fluid Mech.*, 'Numerical experiments on strongly turbulent thermal convection in a slender cylindrical cell', **477**, 19 (2003).
- [77] Yakhot V., ' $\frac{4}{5}$ Kolmogorov Law for Statistically Stationary Turbulence: Application to High Rayleigh Number Bénard Convection', *Phys. Rev. Lett.* **69**, 769 (1992).
- [78] Skrbek I., Niemela J. J., Sreenivasan K. R., and Donnelly R. J., 'Temperature structure functions in the Bolgiano regime of thermal convection', *Phys. Rev. E* **66**, 036303 (2002).
-

-
- [79] Kunnen R. P. *et al.*, ‘Numerical and experimental investigation of structure-function scaling in turbulent Rayleigh-Bénard convection’, *Phys. Rev. E* **77**, 016302 (2008).
- [80] Castaing B., Gunaratne G., Heslot F. *et al.*, ‘Scaling of hard thermal turbulence in Rayleigh-Bénard convection’, *J. Fluid Mech.* **204**, 1 (1989).
- [81] Cioni S., Ciliberto S., and Sommeria J., ‘Strongly turbulent Rayleigh-Bénard convection in mercury: comparison with results at moderate Prandtl number’, *J. Fluid Mech.* **335**, pp. 111-140 (1997).
- [82] Niemela J. J. *et al.*, ‘The wind in confined thermal convection’, *J. Fluid Mech.* **449**, 169 (2001).
- [83] Sreenivasan K. R., Bershadskii A., and Niemela J. J., ‘Mean wind and its reversal in thermal convection’, *Phys. Rev. E* **65**, 056306 (2002).
- [84] Brown E., Nikolaenko A., and Ahlers G., ‘Reorientation of the Large-Scale Circulation in Turbulent Rayleigh-Bénard Convection’, *Phys. Rev. Lett.* **95**, 084503 (2005).
- [85] Brown E., and Ahlers G., ‘Rotations and cessations of the large-scale circulation in turbulent Rayleigh-Bénard convection’, *J. Fluid Mech.* **568**, 351 (2006).
- [86] Xi H. D., Zhou Q., and Xia K. Q., ‘Azimuthal motion of the mean wind in turbulent thermal convection’, *Phys. Rev. E* **73**, 056312 (2006).
- [87] Ahlers G., Grossmann S., and Lohse D., ‘Heat transfer and large scale dynamics in turbulent Rayleigh-Bénard convection’, *Rev. Modern Phys.* **81**, 503 (2009).
- [88] Xi H. D., Lam S., and Xia K. Q., ‘From laminar plumes to organized flows: the onset of large-scale circulation in turbulent thermal convection’, *J. Fluid Mech.* **503**, pp. 47-56 (2004).
- [89] Kadanoff L. P., ‘Turbulent heat flow: structures and scaling’, *Phys. Today* **54**, 34 (2001).
- [90] Y. Tsuji, T. Mizuno, T. Mashiko, and M. Sano, ‘Mean Wind in Convective Turbulence of Mercury’, *Phys. Rev. Lett.* **94**, 034501 (2005).
- [91] Xi H.D. and Xia K. Q., *Phys. Rev. E* **75**, ‘Cessations and reversals of the large-scale circulation in turbulent thermal convection’, 066307 (2007).
- [92] Xi H.D. and Xia K. Q., ‘Flow mode transitions in turbulent thermal convection’, *Phys. Fluids* **20**, 055104 (2008).
- [93] Xi H. D. and Xia K. Q., ‘Azimuthal motion, reorientation, cessation, and reversal of the large-scale circulation in turbulent thermal convection: A comparative study in aspect ratio one and one-half geometries’, *Phys. Rev. E* **78**, 036326 (2008).
- [94] Qiu X. L. and Tong P., ‘Onset of Coherent Oscillations in Turbulent Rayleigh-Bénard Convection’, *Phys. Rev. Lett.* **87**, 094501 (2001).
-

- [95] Sano M., Wu X. Z., and Libchaber A., ‘Turbulence in Helium gas free convection’, *Phys. Rev. A*, **40**, 6421 (1989).
- [96] Benzi R., ‘Flow Reversal in a Simple Dynamical Model of Turbulence’, *Phys. Rev. Lett.* **95**, 024502 (2005).
- [97] Araujo F. F., Grossmann S., and Lohse D., ‘Wind Reversals in Turbulent Rayleigh-Bénard Convection’, *Phys. Rev. Lett.* **95**, 084502 (2005).
- [98] Brown E. and Ahlers G., ‘Large-Scale Circulation Model for Turbulent Rayleigh-Bénard Convection’, *Phys. Rev. Lett.* **98**, 134501 (2007).
- [99] Brown E. and Ahlers G., ‘A model of diffusion in a potential well for the dynamics of the large-scale circulation in turbulent Rayleigh-Bénard convection’, *Phys. Fluids* **20**, 075101 (2008).
- [100] Villermaux E., ‘Memory-Induced Low Frequency Oscillations in Closed Convection Boxes’, *Phys. Rev. Lett.* **75**, 4618 (1995).
- [101] Stringano G. and Verzicco R., ‘Mean flow structure in thermal convection in a cylindrical cell of aspect ratio one half’, *J. Fluid Mech.* **548**, 1 (2006).
- [102] Benzi R. and Verzicco R., ‘Numerical simulations of flow reversal in Rayleigh-Bénard convection’, *Europhys. Lett.* **81**, 64008 (2008).
- [103] Breuer M. and Hansen U., ‘Turbulent convection in the zero Reynolds number limit’, *Europhys. Lett.* **86**, 24004 (2009).
- [104] Hansen U., Yuen D. A., and Kroening E., ‘Transition to hard turbulence in thermal convection at infinite Prandtl number’, *Phys. Fluids A* **2** (12), 2157 (1990);
- [105] Hansen U., Yuen D.A., and Kroening S.E., ‘Mass and heat transport in strongly time-dependent thermal convection at infinite prandtl number’, *Geophys. Astrophys. Fluid Dyn.* **63**, 67 (1992).
- [106] Paul S. *et al.*, ‘Chaotic travelling rolls in Rayleigh-Bénard convection’, *Pramana* **74**, 75 (2010).
- [107] Verma M. K., ‘TARANG: An object-oriented code for turbulence simulation’, *Unpublished* (2008).
- [108] Canuto C. Hussaini, Quarteroni A., and Zhang T. A., *Spectral methods in fluid turbulence*, (Springer-Verlag, Berlin) 1988.
- [109] Pope S. B., *Turbulent Flows*, (University Press, Cambridge) 2000.
- [110] Sengupta T. K., *Fundamentals of computational fluid dynamics*, (University-Press, Hyderabad) 2004.
-

-
- [111] Tam C. K. W. and Webb J. C., ‘Dispersion-Relation-Preserving Finite Difference Schemes for Computational Acoustic’, *J. Comput. Phys.* **107**, pp. 262-281 (1993).
- [112] Anderson D. A., Tannehill J. C., and Pletcher R. H., ‘Computational Fluid Mechanics and Heat Transfer’, *Hemisphere Publishing Corporation*, New York, 1984.
- [113] Das A., Ghosal U., and Kumar K., ‘Asymmetric Squares as standing waves in Rayleigh-Bénard Convection’, *Phys. Rev. E* **62**, R3051 (2000).
- [114] Stein R. F. and Norlund A., ‘Realistic solar convection simulations’ *Sol. Phys.* **192**, pp. 91-108 (2000).
- [115] Pal P., Paul S., Wahi P., and Verma M. K., ‘Dynamics of zero-Prandtl number convection near the onset’, arXiv:1008.0752v1 (2010).
- [116] Nandakumar K., and Chatterjee A., ‘Resonance, parameter estimation, and modal interactions in a strongly nonlinear benchtop oscillator, *Nonlinear Dynamics*’ *Nonlin. Dynam.* **40**, pp. 143-167 (2005); Wahi P., and Chatterjee A., ‘Self-interrupted regenerative metal cutting in turning’, *Int. J. Nonlin. Mech.* **43**(2), pp. 111-123 (2008).
- [117] Dhooge A., Govaerts W., and Kuznetsov Y. A., *Matcont: A MATLAB package for numerical bifurcation analysis of ODEs*. *ACM TOMS* **29**, pp. 202-214 (2003).
- [118] Guckenheimer J. and Holmes P., *Nonlinear Oscillations, Dynamical Systems, and Bifurcations of Vector Fields* (Springer, New York) 1983.
- [119] Epstein I. R. and Pojman J. A., *An Introduction to Nonlinear Chemical Dynamics: Oscillations, Waves, Patterns, and Chaos* (Oxford University Press, Oxford, 1998); Meron E. and Procaccia I., ‘Gluing bifurcations in critical flows: The route to chaos in parametrically excited surface waves’, *Phys. Rev. A* **35**, 4008 (1987).
- [120] Ott E., *Chaos in Dynamical Systems* (Cambridge University Press, Cambridge) 2002.
- [121] Mercader I. *et al.*, ‘Bifurcations and chaos in single-roll natural convection with low Prandtl number’, *Phys. Fluids A* **17**, 104108 (2005).
- [122] Mishra P. K. and Verma M. K., ‘Energy Spectra and Fluxes for Rayleigh-Bénard Convection’, *Phys. Rev. E*, **81**, 056316 (2010).
- [123] Lesieur M., *Turbulence in fluids*, (Kluwer Acc. Publishers, Dordrecht) 1990.
- [124] Verma M. K., ‘Statistical theory magnetohydrodynamic turbulence: recent results’, *Phys. Rep.* **401**, pp. 229-380 (2004); Verma M. K., Kumar K., and Kamble B., ‘mode-to-mode energy transfers convective patterns’, *Pramana, J. Phys.* **67**, 1129 (2006).
- [125] Kraichnan R., ‘The structure of isotropic turbulence at very high Reynolds numbers’, *J. Fluid Mech.* **5**, pp. 497-543 (1959).
-

- [126] Toh S. and Suzuki E., ‘Entropy Cascade and Energy Inverse Transfer in Two-Dimensional Convective Turbulence’, *Phys. Rev. Lett.* **73**, 1501 (1994).
- [127] Debliquy O., Verma M. K., and Carati D., ‘Energy fluxes and shell-to-shell transfers in three-dimensional decaying magnetohydrodynamic turbulence’, *Phys. of Plasmas* **12**, 042309 (2005).
- [128] Balachandar S., Maxey M. R., and Sirovich L., ‘Numerical Simulation of High Rayleigh Number Convection’, *J. Sci. Comput.* **4**, 219 (1989).
- [129] Verzicco R., ‘Turbulent thermal convection in a closed domain: viscous boundary layer and mean flow effects’, *Eur. Phys. J. B* **35**, 133 (2003).
- [130] Rubinstein R., ‘Renormalization group theory of Bolgiano scaling in Boussinesq turbulence’, NASA Technical Memorandum, 106602 (1994).
- [131] Mishra P. K., De A. K., Verma M. K., and Eswaran V., ‘Dynamics of reorientations and reversals of large scale flow in Rayleigh-Bénard convection’, *J. Fluid Mech.* 2010 (In Press).
- [132] Stevens R. J. A. M, Verzicco R., & Lohse D., ‘Radial boundary layer structure and Nusselt number in Rayleigh-Bénard convection’, *J. Fluid Mech.*, **643**, 495 (2010).
- [133] Grötzbach G., ‘Spatial resolution requirement for direct numerical simulation of Rayleigh-Bénard convection’, *J. Comput. Phys.* **49**, 241 (1983).
- [134] Verzicco R., and Camussi R., ‘Prandtl number effects in convective turbulence’, *J. Fluid Mech.* **383**, 55 (1999).
- [135] See VC-7 and VC-8 on <http://home.iitk.ac.in/~mkv/Videos/Convection.html> to view animations of dynamics of Large scale circulation for $R = 2 \times 10^7$ in the vertical ($\theta = 3\pi/4$) and horizontal ($z = 0.5$) sections.
- [136] Brown E., Funfschilling D., and Ahlers G., ‘Anomalous Reynolds-number scaling in turbulent Rayleigh-Bénard convection’, *J. Stat. Mech.* **10**, P10005 (2007).
- [137] Wicht J. & Olson P., ‘A detailed study of the polarity reversal mechanism in a numerical dynamo model’, *Geochem. Geophys. Geosyst.* **5**, Q03H10, (2004).
-